



**INTERNATIONAL RESEARCH CENTER MAGTOP**

**DOCTORAL THESIS**

---

**Thermoelectric phenomena in topological materials**

---



Supervisor

**Dr. hab. Marcin Matusiak**

Author

**MSc. Md Shahin Alam**

*A thesis submitted in partial fulfillment of the requirements  
for the degree of Doctor of Philosophy to*

**Institute of Physics, Polish Academy of Sciences**

**Warsaw, June 2024**

*Dedicated to my paternal and maternal  
grandparents.*

## **Acknowledgements**

First and foremost, I would like to express my deep gratitude to my thesis supervisor, Prof. Dr. hab. Marcin Matusiak, for his invaluable guidance, inspiration, and support throughout this journey. I have been fortunate to work with Dr. hab. Marcin Matusiak on my Ph.D. since 2020. His systematic approach to generating ideas, methodological approach, analyzing data, and writing manuscripts has significantly contributed to my achievements. Moreover, he has supported me in various aspects of my life beyond physics, imparting many life lessons that I will always cherish.

I would also like to express my gratitude to my labmates and collaborators for their invaluable contributions to my research achievements. Special thanks go to my friends for their companionship, support, and encouragement throughout this journey.

Lastly, I am immensely thankful to my parents and family members for their unwavering support, love, and blessings. Without their endless encouragement and support, none of this would have been possible.

We appreciate the support of the Foundation for Polish Science through the international research agendas program co-financed by the European Union within the smart growth operational program.

## **Author's declaration**

I confirm that the work contained in this thesis has not been submitted for consideration for any other academic award and has been completed in accordance with the rules and guidelines of the Institute of Physics, Polish Academy of Sciences. The work is the candidate's own contribution, unless otherwise indicated by a specific reference in the text. Work carried out using or collaborating with others is acknowledged as such. In the dissertation, only the author's viewpoints are given.

License Number : RNP/24/MAY/079651

SIGNED:.....

DATE: .....

## List of publications

The following articles are part of this thesis, where I contributed as the first author highlighted by bold text.

**Md Shahin Alam**, P.K. Tanwar, Krzysztof Dybko, Ashutosh S. Wadge, Przemysław Iwanowski, Andrzej Wiśniewski, Marcin Matusiak, *Temperature-Driven Spin-Zero Effect in TaAs<sub>2</sub>*, J. Phys. Chem. Solids **170**, 110939 (2022).

**Md Shahin Alam**, Amar Fakhredine, Mujeeb Ahmad, P. K. Tanwar, Hung-Yu Yang, Fazel Tafti, Giuseppe Cuono, Rajibul Islam, Bahadur Singh, Artem Lynnyk, Carmine Autieri, and Marcin Matusiak, *Sign change of anomalous Hall effect and anomalous Nernst effect in the Weyl semimetal CeAlSi*, Phys. Rev. B **107**, 85102 (2023).

**Md Shahin Alam**, Alexandr Kazakov, Mujeeb Ahmad, Rajibul Islam, Fei Xue, Marcin Matusiak, *Quantum transport properties of the topological Dirac Semimetal  $\alpha$ -Sn*, arXiv:2403.00083 (2024)[Accepted in Phys. Rev. B].

## Publications other than thesis

I have also contributed to the following articles.

Pardeep Kumar Tanwar, **Md Shahin Alam**, Mujeeb Ahmad, Dariusz Kaczorowski, and Marcin Matusiak, *Severe violation of the Wiedemann-Franz law in quantum oscillations of NbP*, Phys. Rev. B **106**, L041106 (2022).

Pardeep Kumar Tanwar, Mujeeb Ahmad, **Md Shahin Alam**, Xiaohan Yao, Fazel Tafti, Marcin Matusiak, *Gravitational anomaly in the ferrimagnetic topological Weyl semimetal NdAlSi*, Phys. Rev. B **108**, L161106 (2023).

# Achievements

**Leonard Sosnowski Prize**, Best PhD Student award, 51st International School & Conference on the Physics of Semiconductors, Jaszowiec 2023, Szczyrk, Poland.

**One of the 10 most downloaded Physical Review B articles in 2023**, Md Shahin Alam\* et al, Sign change of anomalous Hall effect and anomalous Nernst effect in the Weyl semimetal CeAlSi, Physical Review B **107**, 085102 (2023).

## List of oral and poster presentations

**M. S. Alam** et al., American Physical Society March Meeting (APS 2023), March 2023, “Anomalous transport properties of Weyl semimetal CeAlSi”, Las Vegas, Nevada, USA. **Poster**

**M. S. Alam** et al., 51st International School & Conference on the Physics of Semiconductors (Jaszowiec 2023), June 2023, “Anomalous transverse response in topological magnet CeAlSi”, Silesian Beskid Region, Poland, **Oral**

**M. S. Alam** et al., Joint European Magnetism Symposia Conference (JEMS 2022), July 2022, “Spin zero effect in nonmagnetic centrosymmetric dipnictides TaAs<sub>2</sub>”, Warsaw, Poland. **Poster**

# **CERTIFICATE**

This is to certify that the thesis entitled “Thermoelectric phenomena in topological materials”, submitted by Md Shahin Alam to Institute of Physics, Polish Academy of Sciences, is a record of bonafide research work under my supervision and guidance, and I consider it worthy of consideration for the award of the degree of Doctor of Philosophy of the Institute.

---

## **Supervisor**

Dr. hab. Marcin Matusiak,  
prof. IF PAN MagTop, Institute of Physics,  
Polish Academy of Sciences Warsaw, Poland

# ABSTRACT

Three-dimensional topological semimetals are a new class of quantum materials characterized by a non-trivial bulk and surface states. Electronic bands in their structure crosses at gapless points, whose vicinity is populated by unique relativistic-like quasiparticles. As a result, we observe in these materials a kaleidoscope of unusual electronic properties, and among the standard methods of revealing them are measurements of charge transport. These are meaningful and relatively easy to perform but a more in-depth analysis often requires additional experimental evidence. As such, the thermoelectric transport measurements provide an exceptional tool to probe the electronic properties of topological semimetals with high sensitivity indicated by the Mott - Jones relation. In this thesis I have focused on the three types of quantum effects observed in transport phenomena. Specifically, these are quantum oscillations (QOs), the anomalous Hall effect (AHE), the anomalous Nernst effect (ANE) and the chiral anomaly.

The key characteristics of fermions in topological semimetals can be studied by quantum oscillation measurements. Here, we present a detailed analysis of QOs in TaAs<sub>2</sub>, where we observed an unusual temperature ( $T$ ) evolution of the fundamental frequency  $\beta$  and its second harmonic  $2\beta$  amplitudes. Namely, in the oscillatory Nernst signal the former disappears completely at  $T \approx 25$  K, while  $2\beta$  frequency is still present. We attribute this behavior to a temperature-induced spin-zero effect derived from the temperature evolution of the Landé  $g$ -factor. Subsequently, the  $T$  - dependence of the  $g$ -factor may reflect evolution of the spin-orbit coupling, which in the case of TaAs<sub>2</sub> can go hand in hand with a change a topology of the electronic system.

One important feature of Weyl fermions is the accompanying Berry curvature (BC), which acts like an effective magnetic field leading to the appearance of intrinsic AHE and ANE. In the ferromagnetic phase of Weyl semimetal CeAlSi, we detected a sign change in the anomalous Hall conductivity (AHC) from positive to negative, when the magnetic field ( $B$ ) was rotated from the hard to easy axis. This sign reversal in AHC was attributed to the reconstruction of the electronic structure and a change in associated BC driven by spin reorientations. Additionally, the anomalous Nernst conductivity (ANC) was detected when  $B$  was oriented along the hard axis. Significant AHC and ANC persisted in the paramagnetic

phase of CeAlSi, and their temperature dependence can be described by the presence of the Weyl points near the Fermi level.

The evidence for the chiral anomaly in the Weyl system based solely on charge transport measurements, i.e. observation of the negative longitudinal magnetoresistance (NLMR), has sometimes been questioned due to the possible contribution of the current jetting effect. Here, we demonstrate that the pumping of chiral fermions between Weyl cones can be observed in the topological Dirac semimetal  $\alpha$ -Sn using combined electrical and thermoelectric transport studies. The latter is expected to be robust to external artefacts. The experimental evidence of the chiral anomaly were detected in both measurements – NLMR and negative slope of the thermopower were observed at low temperatures when the magnetic field was parallel to the applied electric field ( $E$ ) or the thermal gradient ( $\nabla T$ ). Furthermore, the angular variation of resistivity and thermopower confirmed the rapid diminishing of anomalous chiral current when magnetic field was tilted away from the applied  $E$  or  $\nabla T$ . We also showed that at high temperature the intervalley Weyl scattering time decreases, and as a consequence  $\alpha$ -Sn in this range is no longer in the chiral limit.

# STRESZCZENIE

Trójwymiarowe semimetale topologiczne stanowią nową klasę materiałów kwantowych charakteryzujących się obecnością nietrywialnych stanów objętościowych i powierzchniowych. W strukturze elektronowej tych związków dochodzi do przecinania się pasm w bezprzerwowych punktach, których sąsiedztwo jest obsadzone relatywistycznymi kwazicząstkami. W rezultacie obserwujemy w takich materiałach kalejdoskop niezwyklej własności elektronowych, zwykle badanych za pomocą pomiarów transportu ładunkowego. Otrzymane w ten sposób dane niezaprzeczalnie niosą wiele informacji i są stosunkowo łatwe do otrzymania, jednak dogłębniejsza analiza często wymaga dodatkowej eksperymentalnej ewidencji. Takową oferują badania transportu termoelektrycznego, które, jak sugeruje formuła Motta – Jonesa, są wysoce czułym narzędziem do badania własności elektronowych semimetalu topologicznego. W niniejszej rozprawie skupiłem się na trzech rodzajach efektów kwantowych obserwowanych w zjawiskach transportowych. Są to mianowicie oscylacje kwantowe (QO), anomalny efekt Halla (AHE) i anomalny efekt Nernsta (ANE) oraz anomalia chiralna.

Podstawowe własności fermionów w semimetalach topologicznych można badać za pomocą pomiarów oscylacji kwantowych. W pracy przedstawiono szczegółową analizę QO w  $\text{TaAs}_2$ , gdzie zaobserwowaliśmy nietypową ewolucję temperaturową ( $T$ ) amplitud częstotliwości fundamentalnej  $\beta$  i jej drugiej harmonicznej  $2\beta$ . Otóż w oscylacyjnym sygnale Nernsta pierwsza z nich zanika całkowicie przy  $T \approx 25$  K, podczas gdy częstotliwość  $2\beta$  jest nadal obserwowana. Przypisujemy to zachowanie efektowi spin - zero indukowanemu zmianą temperatury, a będącemu skutkiem ewolucji czynnika Landégo ( $g$ ). Ta z kolei może odzwierciedlać zmiany sprzężenia spin - orbita, co w przypadku  $\text{TaAs}_2$  powinno wiązać się z przededefiniowaniem topologii układu elektronowego.

Ważną cechą fermionów Weyla jest towarzysząca im niezerowa krzywizna Berry'ego (BC), która działa jak efektywne pole magnetyczne prowadząc do pojawienia się niezwiązanych z rozproszaniem AHE i ANE. W fazie ferromagnetycznej semimetalu Weyla  $\text{CeAlSi}$  wykryliśmy zmianę znaku anomalnego przewodnictwa Halla (AHC) z dodatniego na ujemny, zachodzącą na skutek zmiany orientacji pola magnetycznego ( $B$ ) z trudnej do łatwej osi magnetyzacji. Zmiana znaku AHC została powiązana z rekonstrukcją struktury elektronowej (i wynikającej z niej BC), która jest konsekwencją reorientacji spinów. Gdy  $B$

było skierowane wzdłuż trudnej osi, stwierdzono także pojawianie się anomalnego przewodnictwa Nernsta (ANC). Co istotne AHC i ANC pozostały mierzalne również w fazie paramagnetycznej CeAlSi, a ich zależności temperaturowe można zamodelować zakładając obecność punktów Weyla w pobliżu poziomu Fermiego.

Ewidencja wskazująca na pojawianie się anomalii chiralnej w układzie Weyla oparta wyłącznie na pomiarach transportu ładunkowego, tj. obserwacji ujemnego magnetooporu podłużnego (NLMR), była czasami kwestionowana ze względu na możliwy wkład od tzw. efektu current – jetting. W naszej pracy pokazujemy, że pompowanie chiralnych fermionów między stożkami Weyla w topologicznym semimetalu Diraca  $\alpha$ -Sn można zaobserwować przy użyciu połączonych badań transportu elektrycznego i termoelektrycznego. Oczekuje się przy tym, że te ostatnie powinny być odporne na artefakty eksperymentalne. Wyniki wskazujące na pojawianie się anomalii chiralnej zostały wykryte w obu pomiarach. W niskich temperaturach oraz gdy pole magnetyczne było równoległe do przyłożonego pola elektrycznego ( $E$ ) albo gradientu temperatury ( $\nabla T$ ) zaobserwowano NLMR albo ujemne nachylenie polowej zależności siły termoelektrycznej. Co więcej, kątowne zależności oporności elektrycznej i siły termoelektrycznej potwierdzają szybką degradację anomalnego prądu chiralnego, gdy pole magnetyczne było oddalone od kierunku przyłożonego  $E$  albo  $\nabla T$ . Wykazaliśmy również, że w wysokiej temperaturze międzypolinowy czas rozpraszania maleje, a w konsekwencji  $\alpha$ -Sn w tym zakresie nie znajduje się już w granicy chiralnej.

# Contents

<b>List of figures</b>	<b>xiii</b>
<b>1. Introduction</b>	<b>1</b>
1.1 Topological semimetals.....	2
1.1.1 Dirac semimetals.....	2
1.1.2 Weyl semimetals.....	5
1.2 Transport phenomena.....	9
1.2.1 Quantum oscillations.....	10
1.2.2 Anomalous Hall and Nernst effect.....	14
1.2.3 Chiral anomaly.....	17
1.3 Thermoelectric transport coefficients.....	19
1.4 Motivation and objective of the thesis.....	23
<b>2. Experimental section</b>	<b>25</b>
2.1 Single crystal growth techniques.....	25
2.1.1 Chemical vapour transport method.....	26
2.1.2 Flux method.....	27
2.1.3 Molecular beam epitaxy.....	28
2.2 High field cryogenic system.....	29
2.3 Electrical probe.....	32
2.4 Thermoelectrical probe.....	33
2.5 Electrical transport measurements (TEP).....	35
2.5.1 Sample preparation.....	37
2.5.2 Measurements.....	38
2.6 Thermoelectrical transport measurements.....	40
2.6.1 Sample preparation.....	41
2.6.2 Measurements .....	42
2.7 Calibration of TEP.....	44
<b>3. Articles Comprising the thesis</b>	<b>46</b>
3.1 A brief summary of the main results .....	46
3.1.1 ARTICLE I: Quantum oscillations.....	47
3.1.2 ARTICLE II: Anomalous Hall and anomalous Nernst effect...	62
3.1.3 ARTICLE III: Chiral anomaly.....	80
<b>4. Conclusions</b>	<b>111</b>
<b>Bibliography</b>	<b>114</b>

# List of Figures

1.1	Schematic representation of electronic structure; (a) trivial insulator; (b) Dirac semimetal; (c) Band inversion mechanism formed pair of Dirac points protected by uniaxial rotational symmetry. (d) Pair of Dirac points of $\alpha$ -Sn at $\pm k_z$ protected by four fold rotational symmetry ( $C_{4z}$ ) along z axis .....	5
1.2	Schematic representation: (a) A four-fold Dirac point can split into pairs of two-fold Weyl points with opposite chirality when at least one symmetry, such as time reversal or inversion symmetry, is broken. (b) The surface projection of a pair of Weyl points connected through a Fermi arc.....	9
1.3	Schematic representation: (a) Relativistic Landau level spectra under applied magnetic field. (b) Cylindrical Landau tubes crossing through a 3D Fermi surface.....	14
1.4	Schematic representation of (a) skew scattering; (b) side jump mechanism .....	17
1.5	The pumping of Weyl fermions between Weyl nodes of different chirality when a parallel electric field is applied along with a magnetic field .....	19
2.1	A schematic representation of chemical vapour transport method.....	27
2.2	A simplified schematic representation of molecular beam epitaxy used for the growth of $\alpha$ -Sn thin film.....	28
2.3	A schematic representation of the cryogenic system.....	32
2.4	Different parts of our hand crafted electrical probe.....	33
2.5	Sections of our custom-made thermoelectrical probe.....	34

2.6	A typical schematic diagram of the Hall bar geometry. A constant current ( $j_{xx}$ ) is injected along the longest side, the $x$ -axis of the sample. The magnetic field ( $B$ ) is applied perpendicular to the surface of the sample, i.e. $z$ -axis. The generated longitudinal ( $V_{xx}$ ) and transverse ( $V_{xy}$ ) voltages were recorded using a Nanovoltmeter.....	<b>35</b>
2.7	An example of a single crystalline sample prepared for the electrical measurements.....	<b>38</b>
2.8	Schematic diagram of the magnetoelectric measurement setup. Blue lines denote electrical connections, orange ones denote data transfer.....	<b>39</b>
2.9	A schematic representation thermopower and Nernst effect.....	<b>41</b>
2.10	A Single crystal of $TaAs_2$ was prepared to determine its thermoelectric properties.....	<b>42</b>
2.11	A schematic diagram of thermoelectric measurements setup. Blue lines denote electrical connections, orange ones denote data transfer.....	<b>44</b>
2.12	Temperature dependences of thermoelectric power of Leads of TEP.....	<b>45</b>

## INTRODUCTION

Prior to 1980, the phase transitions of materials were understood according to Landau's formalism, in which the system goes from a highly symmetric phase to a lower or broken symmetric phase [1,2]. Changes of symmetry can be described by an order parameter, which is finite for the ordered phase and vanishes in the highly symmetric phases. In the 1980s, the discovery of quantum Hall effect in 2D electron gasses led to introduction of exotic topological phases, which do not involve breaking of symmetries [3,4]. These quantum phases can be classified with a topological invariant, namely Thouless-Kohmoto-Nightingale-Nijs number (TKNN), or the Chern number (C) [3]. This topological invariant can be understood in terms Berry phase, in which a system acquired an additional phase associated with the Bloch wave functions during the cyclic adiabatic transformation [5]. Over the past sixteen years, the theoretical prediction of topological phases induced by spin-orbit interaction has been realized in real crystalline materials [6,7]. Initially gapped topological phases, also known as topological insulators (TIs) have been reported, those were protected by time reversal symmetry [8]. Subsequently, a topological crystalline insulator (TCI) phase protected by crystalline symmetry was experimentally discovered [9].

In the last decade, topological semimetals (TSMs) distinct from TIs, have attracted considerable attention due to the bulk band crossings resulting in non-trivial electronic structures [10–13]. In these materials, the valence band and the conduction band intersect at or near the Fermi level ( $E_F$ ) to form isolated points or lines [11]. Such gapless band contact points were predicted very early on, but their importance due to their topological nature has

# Chapter 1: Introduction

---

only recently been realized [14]. They give rise to gapless electronic excitations associated with the topological invariant [15,16].

This chapter is structured as follows. First, I will provide a detailed overview of Dirac and Weyl semimetals. Then, I will discuss the various transport phenomena observed in topological Dirac and Weyl semimetals. Following this, I will briefly discuss the thermoelectric response in topological materials. Finally, I will present the motivation and objectives of this work.

## 1.1 Topological semimetals

In the past few years, the presence of low-energy fermionic excitation in TSMs has brought them to the forefront of condensed matter research [11,12]. TSMs are divided into three categories based on the dimensionality of the band crossing at or near the Fermi level in the momentum space [17]. The first group exhibit zero-dimensional (0D) band crossing, forming two or four degenerate band crossings around the  $E_F$ . Dirac and Weyl semimetals are the famous materials showing 0D band crossing. On the other hand, nodal-line semimetals belong to the second group, in which band crossing occurs along the one-dimensional (1D) line in the momentum space. In recent times, two-dimensional (2D) band crossing has been proposed in nodal-surface semimetals [18].

### 1.1.1 Dirac semimetals

The low energy excitations of free or nearly free quasiparticles in solids can describe by the Schrödinger equation. However, non-relativistic Schrödinger equation has certain limitations, for instance recently discovered fermionic excitations in TSMs need to be described by Dirac and Weyl equations [19]. The Dirac Hamiltonian of an electronic system can be written as [19]:

## Chapter 1: Introduction

---

$$H_D = v_F \alpha \cdot \mathbf{k} + \beta m v_F^2 = \begin{bmatrix} v_F \sigma \cdot \mathbf{k} & m v_F^2 \\ -m v_F^2 & -v_F \sigma \cdot \mathbf{k} \end{bmatrix} \quad (1.1)$$

Where  $k$ ,  $\sigma$ ,  $m$  and  $v_F$  are the momentum, Pauli spin, effective mass and Fermi velocity respectively. Since Eqn. 1.1 describing the Dirac fermions inside solids is analogous to high energy Dirac Hamiltonian (where  $v_F$  was replaced by the speed of light  $c$ ), it follows an analogous energy – momentum relation:  $E_{\pm} = \pm \sqrt{m v_F^4 + k^2 v_F^2}$ . This relation immediately gives for a massive quasiparticle an energy gap  $\Delta E = 2m v_F^2$  at  $k = 0$  (see schematic of Fig. 1.1a). Alternatively, for  $m = 0$  we have a gapless degenerate point as shown in Fig 1.1b, which is known as the Dirac point. Materials having such points are called Dirac semimetals, and their low-energy excitations are identified as massless Dirac fermions [12]. In a sense 3D topological Dirac semimetals are counterpart of 2D graphene [6], but the Dirac states in DSMs differ from the gapless states of graphene. In the latter, the application of spin-orbit coupling (SOC) lifts the degeneracy to make it a quantum spin Hall insulator [6]. On the other hand, Dirac semimetals exhibit symmetry-protected degenerate Dirac nodes in the presence of SOC.

There were initial attempts to achieve DSMs state by fine tuning SOC in a topological insulator by modifying chemical composition [20], by applying strain [21]. However, it was later reported that there are other mechanisms leading to the realization of stable Dirac junctions in DSMs [12]. This can be achieved by (i) band inversion mechanism; (ii) symmetry enforced mechanism (iii) combination of band inversion and uniaxial rotational symmetry. These mechanisms are associated with a broad range of variations in the system's Hamiltonian parameters.

(i) In this mechanism, the degenerate Dirac point can be achieved by the presence inversion symmetry along with the fine tuning of chemical composition and strain. This type of Dirac point was observed during the phase transition between trivial insulators to the

## Chapter 1: Introduction

---

nontrivial topological insulator. Dirac semimetals induced by the band inversion mechanism were reported in  $\text{Pb}_{1-x}\text{Sn}_x\text{Te}$  [9] and  $(\text{Bi}_{1-x}\text{In}_x)_2\text{Se}_3$  [22]. On the other hand Dirac points in  $\text{ZrTe}_5$  occurred naturally by topological phase transition without even change in chemical composition [23].

(ii) Here we have fourfold degenerate Dirac points appearing at high symmetric point of Brillouin zone. The necessary condition is the particular space group of a materials in the presence of nonsymmorphic symmetry, which means glide reflections along with screw rotations [24]. Due to such strong requirements, these kinds of Dirac electronic structure are theoretically predicted to be realized in  $\beta\text{-BiO}_2$  [24] and distorted spinels [25]. These are still awaiting experimental confirmation.

(iii) In this scenario, the tuning of physical parameters, such the chemical composition or strain, etc., ensures that bands of different eigenvalues interact and create Dirac points on the opposite sites of the time-reversal invariant moment (see Fig.1.1c). The presence of uniaxial rotational symmetry preserves the Dirac points under weak perturbations, or in other words, such type of Dirac points are topologically protected. Experimental evidence of topologically protected Dirac semimetals are reported in  $\text{Cd}_2\text{As}_3$  [26],  $\text{Na}_3\text{Bi}$  [27],  $\alpha\text{-Sn}$  [28].

In this dissertation, out of three semimetals one of them is  $\alpha\text{-Sn}$ , in which compressive in-plane strain leads to formation of pair of four fold degenerate Dirac points along out-of-plane wave vector [28]. We report in Ref. [29], in the presence of spin-orbit coupling, two Dirac points ( $\pm k_z$ ) as shown in Fig. 1.1, along the highly symmetric  $\Gamma \rightarrow Z$  direction, protected by four fold rotational symmetry along the  $z$ -axis.

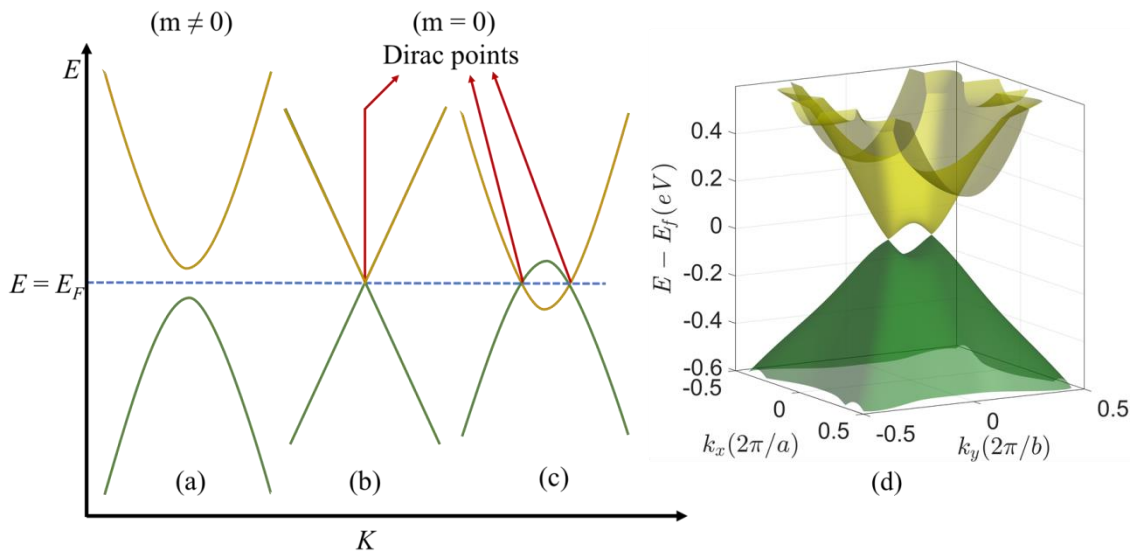


**Figure 1.1.** Schematic representation of electronic structure; (a) trivial insulator; (b) Dirac semimetal; (c) Band inversion mechanism formed pair of Dirac points protected by uniaxial rotational symmetry. (d) Pair of Dirac points of  $\alpha$ -Sn at  $\pm k_z$  protected by four fold rotational symmetry ( $C_{4z}$ ) along z axis.

## 1.1.2 Weyl semimetals

Let's start again with the Dirac Hamiltonian, when  $m = 0$ , equation 1.1 can be rewritten as [30]:

$$H_{\pm} = \pm v_F \sigma \cdot \mathbf{k} \quad (1.2)$$

This is general form of Weyl Hamiltonian analogous to the massless relativistic Hamiltonian suggested by Hermann Weyl in 1929 [31]. Eqn. 1.2 described a pair of band touching points in the electronic structure with an energy eigen values of  $E(\mathbf{k}) = \pm v_F |\mathbf{k}|$ . In the last two decades, these band touching points have been studied in topological materials and denoted as Weyl points [12]. If they occur at or near the Fermi level the corresponding low energy excitations of these band intersection points are at or near the  $E_F$  known as Weyl fermions [12]. Those materials that exhibit this unique property is are called Weyl semimetals.

## Chapter 1: Introduction

---

The Weyl points are distinct from Dirac points, the latter composed of two copies of Weyl points. Weyl points in the electronic structure has stable non-trivial topology described by a nonzero Chern number. The value of  $C$  associated with Fermi surface enclosing the Weyl point in the  $k$ -space can be expressed as [30]:

$$C = \frac{1}{2\pi} \oint \Omega(\mathbf{k}) \cdot d\mathbf{s} \quad (1.3)$$

here,  $\Omega(\mathbf{k})$  is the Berry Curvature. For a 3D Weyl point, the Berry curvature adopts the universal form [30]:

$$\Omega_{\pm}(\mathbf{k}) = \pm \frac{\hat{e}_k}{2k^2} \quad (1.4)$$

where,  $\hat{e}_k$  is the unit normal vector. These result in the Chern number (also known as the chiral or topological charge of Weyl points) being equal to  $C = \pm 1$ . The chiral charge measures the Berry flux in a singular Weyl points, analogously to the electric flux in Gauss's law of classical electrodynamics. Thus, the sign of  $C$  indicates whether the Weyl point in the  $k$  space acts as a source ( $C = +1$ ) or a sink ( $C = -1$ ) of Berry curvature. Since the net chiral charge over the Brillouin zone should be zero, these Weyl points always appear in pairs. The essential condition required to generate a pair of two-fold degenerate Weyl points from a fourfold degenerate Dirac point is breaking of either time reversal symmetry (TRS) or inversion symmetry (SI), as it is discussed below shown schematically in Figure 1.2a. Figure 1.2b shows schematically that the surface projection of the Weyl points are connected with a unclosed contour starting from one Weyl point and terminates at other Weyl point of opposite chirality or Chern number. This unclosed line connecting two Weyl points is called the Fermi arc [32] and it is clearly distinct from the Fermi surface forming a close loop. Thus, detection of the Fermi arc, which can be done via a surface sensitive angle-resolved photoemission spectroscopy (ARPES) technique, provides compelling evidence for a Weyl-type electronic structure.

## Chapter 1: Introduction

---

As mentioned, there are two ways to realize WSMs, (i) by breaking time reversal symmetry, or (ii) by breaking inversion symmetry:

### (i) Time reversal breaking WSMs

Weyl points induced by breaking of TRS were first postulated in pyrochlore iridates  $R_2Ir_2O_7$  (where R is a rare-earth element) [10]. The magnetic order in this compound was found to be due to the all-in/all-out configuration of the Ir (R) sites, leading to a break in the time-reversal symmetry, while the inversion symmetry is preserved. It was theoretically predicted that onsite coulomb interaction can modify the electronic ground state giving rise to the possibility of the Weyl semimetal phase to occur. Following this work, it was postulated that the Weyl phase should form in a magnetic doped superlattice structure composed of magnetic layers and topological insulator [33]. Subsequently, the search for a 3D Weyl semimetal phase in topological insulators began by incorporating magnetic impurities, for instance in HgTe, which was a well-known topological insulator. The doping of this material with Cd atoms can modify the band gap to achieve the critical band touching point, while doping of Mn can break the time reversal symmetry creating 3D Weyl phase in  $Hg_{1-x}Cd_xMn_yTe$  [34]. Later, there were shown several examples of ferromagnetic semimetals and non-collinear antiferromagnets hosting the novel Weyl phase by breaking the TRS, such as  $Co_3Sn_2S_2$  [35],  $Co_2MnAl$  [36],  $Mn_3Sn$  and  $Mn_3Ge$  [36,37] etc. Furthermore, magnetotransport studies have also suggested the existence of Wey points in the Dirac semimetals  $Cd_2As_3$  [38],  $Na_3Bi$  [39] and  $\alpha$ -Sn [28] in the presence of a magnetic field.

### (ii) Inversion breaking WSMs

Initially, researchers were looking for the appearance of Weyl points in a tunable topological insulator  $BiTl(S_{1-x}Te_x)_2$  [40] in which alternating layers can enable inversion symmetry breaking. Topological insulator based superlattice structure can also break the

## Chapter 1: Introduction

---

inversion symmetry, transforming the system to a Weyl semimetal during a topological phase transition [41]. However, these systems have not received significant attention due to the substantial experimental challenges in observing Weyl points, which can disappear with slight variation of real physical parameters such as chemical compositions. On the other hand, materials with internally broken inversion symmetry become frontal because the Weyl points in these materials are well separated and appear near the Fermi level. The compelling evidence of Fermi arc and bulk Weyl fermions was reported in TaAs, and the material was recognized as the first stoichiometric Weyl semimetal [42]. Subsequently, the Weyl fermions were also reported in systems with broken inversion symmetry, such as NbP [43], NbAs [44], TaP [45] etc. Recently, it has been demonstrated theoretically as well as experimentally that RAIPn series (Pn = Ge, Si), in which both inversion and time reversal symmetry are broken, host the Weyl nodes [46].

In addition to the type of symmetry breaking, Weyl semimetals can be divided into two groups due to the dependence of their energy dispersion near Weyl points. The electronic system of type-I WSMs obey Lorentz symmetry and contains untitled Weyl cones in which point like Fermi surface ideally only crosses through Weyl points. The type-II does not follow Lorentz symmetry and exhibits strong tilting of Weyl cones. Their Weyl points touches the electron and hole pockets on the Fermi surface [11].

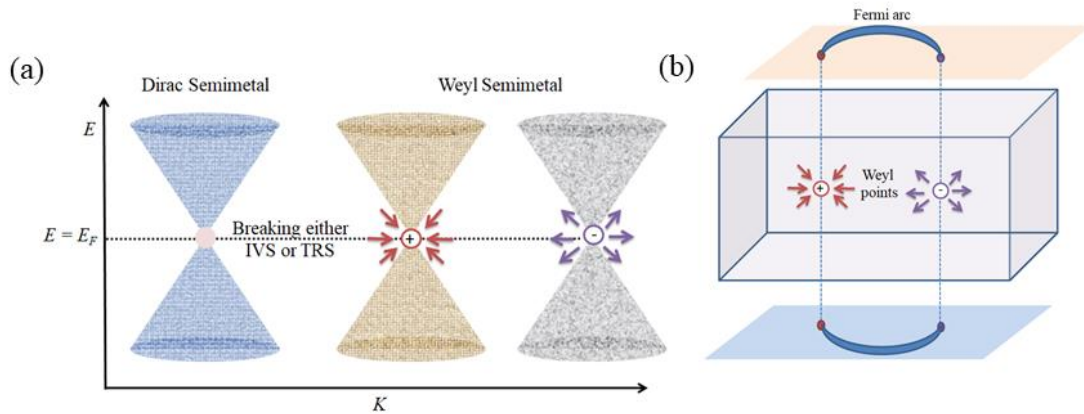


**Figure 1.2.** Schematic representation: (a) A four-fold Dirac point can split into pairs of two-fold Weyl points with opposite chirality when at least one symmetry, such as time reversal or inversion symmetry, is broken. (b) The surface projection of a pair of Weyl points connected through a Fermi arc.

## 1.2 Transport phenomena

Topological semimetals exhibit many intriguing qualities in electronic magnetotransport properties. The linear band crossings near or at the  $E_F$  of these materials give rise to remarkable transport features, including non-saturating in high magnetic field magnetoresistance and magneto-thermopower [47,48]. If the Fermi level lies close to Dirac or Weyl nodes, then small effective mass Dirac or Weyl fermions, together with their high mobility, leads to pronounced quantum oscillations. These significantly affect various transport phenomena, including electric conductivity, where they are referred to as the Shubnikov–de Haas (SdH) effect [49]. A finite Berry curvature associated with Weyl nodes can manifest itself as a phase-shift of QOs [50] and also lead also to emergence of intriguing physical phenomena, such as the intrinsic anomalous Hall effect [51] and anomalous Nernst effect [52]. Still another magnetotransport phenomenon specific to Weyl semimetals occurs when an electric field or thermal gradient is applied parallel to the magnetic field. This can be

## Chapter 1: Introduction

---

principle of chiral charge conservation between Weyl points of opposite chirality, leading to the appearance of an interesting phenomenon called chiral anomaly [53].

### 1.2.1 Quantum oscillations

The study of quantum oscillations is a powerful tool for investigating the electron structure of topological semimetals. This can provide information on the Fermi surface area, effective mass, mobility, Landé g-factor and Berry phase. The theoretical description of quantum oscillations was developed by L.D. Landau, who noted that electronic states of charge carriers become quantized under the influence of a magnetic field. This causes the energy bands to split into Landau levels (LLs), and as they expand with increasing magnetic field, the density of states (DOS) at  $E_F$  becomes modulated to the rhythm of LLs crossing the Fermi energy. The periodic modulations of DOS at  $E_F$  results in the appearance of quantum oscillations in physical quantities such as magnetization, resistivity, Hall resistivity, thermoelectric power, and Nernst effect etc.

Landau level quantization of 3D relativistic fermions is different from non-relativistic electrons. The latter has a parabolic energy dispersion relationship, while for the former it is linear. The energy eigenvalues for 3D non-relativistic electrons, when the magnetic field applied along z-axis can be written as,

$$\varepsilon_{n,k} = \frac{\hbar e B}{m^*} \left( n + \frac{1}{2} \right) + \frac{\hbar^2 k_z^2}{2m^*} \quad (n = 0,1,2,3, \dots) \quad (1.5)$$

where  $n$  represent the Landau levels number,  $\hbar$  is reduced Planck constant and  $e$ ,  $m^*$ ,  $k_z$  is the charge, effective mass and wavevector of the electrons, respectively. Notably, the energy is not quantized along the motion of electrons. Whereas the energy eigenvalues for 3D relativistic fermions can be read as [54],

## Chapter 1: Introduction

---

$$\varepsilon_{n,k} = v_F \operatorname{sgn}(n) \sqrt{2e\hbar|B||n| + \hbar^2 k_z^2} \quad (n = 0, 1, 2, 3, \dots) \quad (1.6)$$

where  $v_F$  is the Fermi velocity of relativistic fermions,  $\operatorname{sgn}(n)$  is the sign function. Analogous to the non-relativistic case, energy along relativistic fermion motion is unquantized. Landau levels for relativistic fermions are shown in Fig. 1.3. The formation of Landau tubes illustrated in Fig. 1.3b involves 3D free electrons under a magnetic field along the  $z$ -axis. Once magnetic field was applied, overlaps between LLs at energy space leading to form a mixture of Landau tubes. Consequently, an equal energy surface intersects multiple Landau cylinders, which radius is field dependent i.e.  $\propto \sqrt{B}$ . Aforementioned quantum oscillations occur when the Landau tube crossing the Fermi surface representing the extremal cross sectional area ( $S_{ex}$ ). Thus, one can find the  $S_{ex}$  from the frequency ( $F$ ) of QOs using Onsager relation,  $F = \frac{2\pi e}{h} S_{ex}$  [49]. The oscillations in physical quantities can be described by the Lifshitz–Kosevich theory [49]. The oscillatory signal of Gibbs thermodynamic potential ( $\widetilde{\Omega}$ ) at zero temperature can be written as [49],

$$\widetilde{\Omega} \propto B^{\frac{5}{2}} \sum_{p=1}^{\infty} \frac{1}{p^{\frac{5}{2}}} \cos\left(2\pi p \left(\frac{F}{B} - \gamma\right) \pm \delta\right) \quad (1.7)$$

where  $p$  represent the harmonic number and  $\pm\delta$  phase shift related to dimensionality of the Fermi surface. Including several damping factors, the general formula for magnetoconductivity is given by [49].

$$\frac{\Delta\sigma}{\sigma} \propto \sum_i S_{ex}^i B^{\frac{1}{2}} \sum_{p=1}^{\infty} R_T R_D R_S \cos\left(2\pi p \left(\frac{F_i}{B} - \gamma_i\right) \pm \delta\right) \quad (1.8)$$

Here  $\gamma_i$  is the phase factor related to band topology,  $R_T, R_D, R_S$  are the temperature reduction, impurity damping and spin reduction factors respectively. The first correction factor  $R_T$  accounts for the temperature effect on the Fermi-Dirac distribution function. The term  $R_T$  is expressed as [49],

## Chapter 1: Introduction

---

$$R_T = \frac{2\pi^2 p k_B T m^* / e \hbar B}{\sinh(2\pi^2 p k_B T m^* / e \hbar B)} \quad (1.9)$$

where  $k_B$  is the Boltzmann constant. As the temperature increases, the thermal broadening of LLs results in drop of amplitude of QOs and its temperature dependent profile allows the effective mass  $m^*$  to be deduced. This is usually small when the Dirac/Weyl points are close to the Fermi level, while  $m^*$  increases with increasing distance between the Fermi level and the node [54]. From  $m^*$  one can also calculate the Fermi velocity of relativistic fermions,  $v_F = \frac{\hbar k_F}{m^*}$ , where  $k_F$  can be obtained from  $S_{ex}$ .

Returning to another damping factor of QOs,  $R_D$ . It is called the Dingle damping term and is associated with impurity quantum scattering of relativistic fermions.  $R_D$  can be expressed as [49],

$$R_D = \exp\left(-2\pi^2 p k_B T m^* / e \hbar B \frac{T_D}{T}\right) \quad (1.10)$$

where  $T_D$  is the Dingle temperature. Any finite scattering will result in broadening of the LLs, which can be associated with the quantum relaxation time ( $\tau_q$ ), given by the relation,  $\Gamma = \hbar/2\tau_q$ . The  $T_D$  can be extracted from the QOs by linear fitting of logarithmic plot of amplitude of oscillations vs  $1/B$ . The estimated Dingle temperature yields  $\tau_q$  via the relation  $\tau_q = \hbar/2\pi k_B T_D$ . Remarkably,  $\tau_q$  can be used to calculate an important parameter related to material transport i.e. quantum mobility ( $\mu_q$ ) via  $\mu_q = e\tau_q/m^*$ .  $\mu_q$  calculated in this way is always lower than that obtained from the Drude model as the classical Drude mobility is unaffected by forward scattering, whereas  $\mu_q$  takes into account scattering in all directions [55].

The final damping term,  $R_S$ , is associated with spin splitting caused by the Zeeman effect, which produces a phase shift between LLs sub-bands with opposite spins. This results in a reduction of the amplitude of QOs given by [49],

$$R_S = \cos\left(\frac{p\pi}{2} \frac{gm^*}{m_e}\right) \quad (1.11)$$

where  $m_e$  is the free electron mass and  $g$  is the Landé  $g$  factor.  $R_S$  is field independent and provides an alternative way to determine  $g$ , that can also be extracted from the peak splitting in QOs. Such analysis has been presented for topological semimetal ZrSiS [56]. Furthermore, the Landé  $g$  factor can also be estimated using the spin zero effect [49]. This phenomenon is defined as the disappearance of the fundamental oscillation while its second harmonic is enhanced at a certain field orientation due to the interference of spin-split Fermi surfaces. Interestingly, we recently reported on the zero spin effect in TaAs<sub>2</sub> caused not by changes in field orientation, but in temperature [57].

Another parameter that can be extracted by studying quantum oscillations is the phase factor  $\gamma$ , which is of particular interest for topological materials. This is because  $\gamma$  is associated with the Berry phase ( $\phi_B$ ) through the relation  $\gamma = \frac{1}{2} - \frac{\phi_B}{2\pi}$  [58]. Ideally, for a linear band dispersion,  $\phi_B = \pi$ . It may deviate when band dispersion changes or in the presence of strong Zeeman field [54].  $\phi_B$  can be derived from QOs by plotting the Landau level fan diagrams.

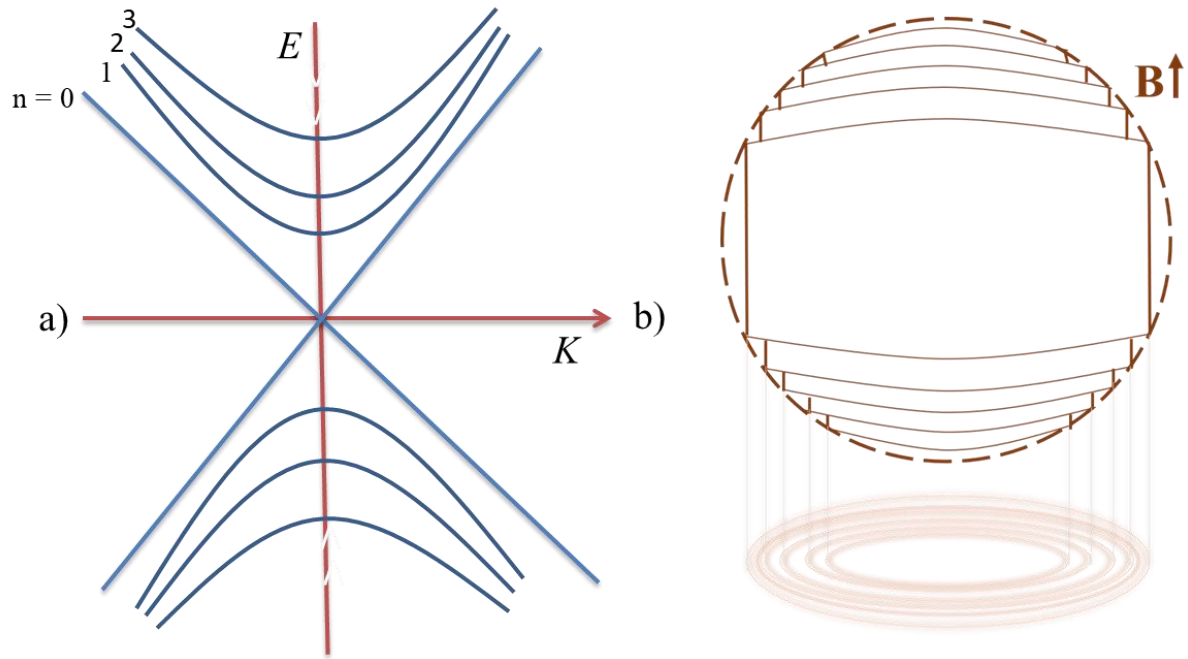


**Figure 1.3.** Schematic representation: (a) Relativistic Landau level spectra under applied magnetic field. (b) Cylindrical Landau tubes crossing through a 3D Fermi surface.

### 1.2.2 Anomalous Hall and Nernst effect

The classical Hall effect occurs in a conductor subjected to a mutually perpendicular magnetic field and current. It was discovered in 1879 and has become an invaluable tool for accurately measuring the concentration of carriers in conductors [59]. For a single band system, the Hall signal is proportional to the magnetic field, but two years after initial discovery, it was found that in Iron the response is stronger at low magnetic field [60]. This implied the presence of additional contributions to the ordinary Hall effect (OHE) from extraordinary or anomalous Hall effect, which is defined as the development of the transverse signal orthogonal to an applied electric field even without presence of external magnetic field. The thermoelectric counterpart of AHE and ANE, is also defined as the generation of transverse voltage in response to the application of thermal gradient without the involvement of a magnetic field [61]. Evidence of AHE can be experimentally distinguished from OHE, as the former steeply increases at low magnetic field and eventually saturates.

## Chapter 1: Introduction

---

Very early it was realized that the AHE in ferromagnetic conductors is proportional to the magnetization. The empirical relation that describe the total Hall resistivity governed by OHE and AHE is given by,

$$\rho_{yx} = R_o H_z + R_s M_z \quad (1.12)$$

where  $H_z, M_z, R_o, R_s$  are the applied magnetic field, magnetization, ordinary Hall coefficient and anomalous Hall coefficient respectively. In particular, the anomalous Hall coefficient  $R_s$  is material specific, in contrast to  $R_o$  which is purely a function of the carrier concentration. It has recently turned out that  $R_s$  can be very high in topological materials [62–64]. The anomalous Hall effect can result from either (i) an intrinsic mechanism or it might originate from the (ii) extrinsic mechanism. The latter is further divided into two categories: skew scattering and side jump mechanism.

### (i) Intrinsic mechanism

In 1954, Karplus and Luttinger (KL) first proposed a theory to describe the anomalous Hall conductivity in solids [65]. They showed that electrons can develop a group or anomalous velocity perpendicular to the applied electric field and this anomalous velocity, which is due to the electronic structure, generates AHE. The total anomalous velocity for ferromagnetic solids with all the bands occupied becomes nonzero, contributing to the AHE. Later, it was shown that the anomalous velocity can be understood within the Berry curvature concept [5]. The Berry curvature was dubbed as anomalous velocity of electrons as a result anomalous Hall voltage developed. The discovery of topologically non-trivial materials had a profound impact on the study of anomalous effects, since linear band crossing gives rise to a non-zero Berry curvature [51]. In the aspect under discussion, this is particularly important for Weyl semimetals, where the presence of opposite chiral Weyl points acts as source of sink of Berry curvature. When the time reversal symmetry is broken, the Berry curvature from

# Chapter 1: Introduction

---

Weyl nodes within the pair does not cancel and can act in a manner analogous to a magnetic field. This leads to anomalous velocity perpendicular to the applied electric field even in a zero magnetic field [62].

Large intrinsic anomalous Hall and Nernst effects have been reported for several time-reversal-breaking Weyl semimetals, such as  $\text{Co}_3\text{Sn}_2\text{S}_2$  [66],  $\text{Co}_2\text{MnGa}$  [63],  $\text{Mn}_3\text{Sn}$  [67],  $\text{MnGe}_3$  [68], etc. It has also been shown that a large intrinsic anomalous contribution can be observed by tuning the location of Weyl points [69]. Recently, we have also reported the sign change of anomalous Hall and anomalous Nernst effects in a ferromagnetic Weyl semimetal  $\text{CeAlSi}$  [70]. In this article we show that the anomalous properties in the magnetic phase are determined by the shift of the Weyl point driven by the reconstruction of the magnetic spins, and in the paramagnetic phase the position of the Weyl point with respect to the Fermi level determines the anomalous properties.

## (ii) Extrinsic mechanism

The anomalous Hall and Nernst effect also can originate from the scattering of charge carries of the magnetic impurities, namely skew scattering or side jump. The idea that the asymmetric scattering from impurities caused by the spin-orbit interaction is responsible for anomalous Hall effect was first proposed by J. Smith in 1955 [71]. The asymmetric scattering, also known as skew scattering, is illustrated in Fig. 1.4a. In this mechanism, the spin-orbit coupling of the impurity scattered the spin up and spin down electron in an asymmetric manner, which contributed to the AHE. The skew scattering obeys a specific relationship between the transverse anomalous Hall resistivity ( $\rho_{yx}$ ) and the longitudinal resistivity ( $\rho_{xx}$ ) i.e.  $\rho_{yx} \propto \rho_{xx}$  [51].

Another type of scattering that can lead to AHE, namely side jump, was introduced by L. Berger in 1964 [72]. In this mechanism the spin up and down electrons experiences a

## Chapter 1: Introduction

---

transverse shift to the incident direction due to influence of the electric field of the impurities. The side jump mechanism is also shown schematically in Figure 1.4b. In this mechanism,  $\rho_{yx}$  follows quadratic dependences with  $\rho_{xx}$ , i.e.  $\rho_{yx} \propto \rho_{xx}^2$  [51].

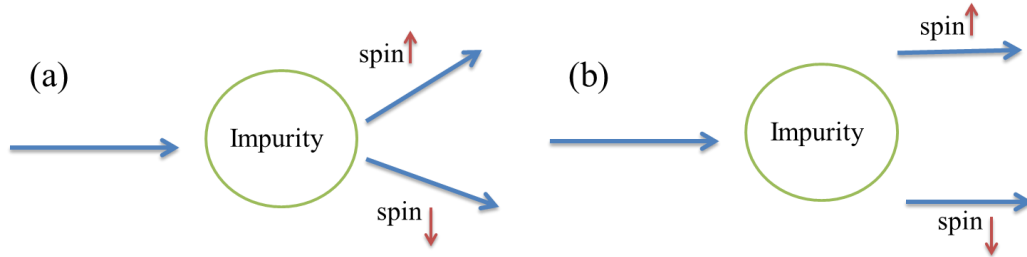


**Figure 1.4.** Schematic representation of (a) skew scattering; (b) side jump mechanism.

### 1.2.3 Chiral anomaly

The concept of a quantum anomaly, which emerged in the field of high-energy physics, describes the breakdown of classically conserved symmetries as quantum effects are turned on [73]. For instance, parity and charge conservation is violated when a pion ( $\pi^0$ ) decays into two photons, providing the first evidence of a chiral anomaly, also known as the Adler-Bell-Jackiw anomaly [74]. Remarkably, in 1983 H.B. Nielsen and M. Ninomiya predicted that the chiral anomaly should occur in relativistic Weyl fermions system when parallel electric and magnetic fields are applied [75]. After it was experimentally shown that the Weyl electronic system can be found in some semimetals, this phenomenon is extensively investigated by several research groups [32,53]. In the quantum limit, the chiral anomaly is the manifestation of pure and opposite chirality of the lowest Landau level of the Weyl cones pair. Application of parallel electric field along with the magnetic field can accelerate the chiral charges from one Weyl cone to other at lowest Landau level as illustrated in Fig. 1.5, and thus the net chirality of the individual nodes becomes unbalanced. The charge pumping rate of a Weyl node is given by [12],

$$\frac{\partial \rho_\chi}{\partial t} = -\chi \frac{e^3}{4\pi^2 \hbar^2} E \cdot B \quad (1.13)$$

where  $\rho_\chi$ ,  $\chi$  represent charge density and chirality of Weyl fermions. Chiral charge pumping of Weyl fermions leads to an anomalous current (or a chiral conductivity), which can be detected in transport measurements as a negative longitudinal magnetoresistance. Since the chiral imbalance can be relaxed by inter-Weyl scattering ( $\tau_i$ ), the anomalous chiral current is proportional to  $\propto E \cdot B \cdot \tau_i$ . This means that large  $\tau_i$  is necessary to observe large NLMR [12]. In the quantum limit the chiral conductivity varies linearly with the magnetic field, whereas in the classical limit it shows quadratic dependence [76]. There is a number of reports of NLMR in Dirac and Weyl semimetals that have been attributed to the presence of a chiral anomaly [23,32,38,39,39,53]. However, it is not always the case even if the negative longitudinal magnetoresistance is observed. For instance, it can be induced by current jetting effect [77] or may be related to the anomalous Hall effect [78]. Therefore, complementary experiments like measurements of the thermoelectric power, thermal conductivity, planar Hall effect and planar Nernst effect are vital to exclude artefacts and probe the intrinsic chiral behavior of Weyl fermions [53]. The investigation of the thermoelectrical coefficients provides a unique opportunity to probe the chiral anomaly free from artefact as the thermopower is measured open circuit condition without charge current flow [79]. Recently, we have also reported of the presence chiral anomaly in the topological Dirac semimetal  $\alpha$ -Sn using electrical and thermoelectrical measurements [29].

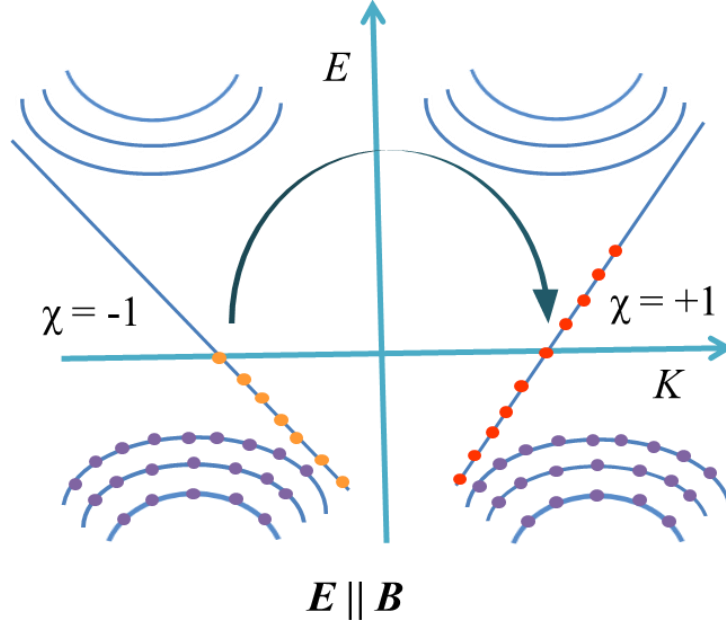


**Figure 1.5.** The pumping of Weyl fermions between Weyl nodes of different chirality when a parallel electric field is applied along with a magnetic field.

### 1.3 Thermoelectric transport coefficients

The discovery that a temperature difference between the junctions of two conductors connected in a closed loop leads to the generation of a magnetic field (due to the flow of electric current) was made by Thomas J. Seebeck in 1821 and published in 1825 [80]. It has been later realized that the basis of this phenomenon is that the flow of charged particles in a conductor is accompanied by a flow of entropy [81]:

$$j^s = S j^e - \kappa \frac{\nabla T}{T}, \quad (1.14)$$

where  $j^s$  is the entropy flow,  $S$  the Seebeck coefficient,  $j^e$  the charge current density,  $\kappa$  the thermal conductivity and  $\nabla T$  the thermal gradient. Generally, the total charge current in presence of the thermal gradient can be written as [82]:

$$j^e = \sigma E - \alpha \nabla T, \quad (1.15)$$

## Chapter 1: Introduction

---

where  $E$  is the electrical field whereas  $\alpha$  and  $\sigma$  denote the thermoelectrical conductivity and electrical conductivity tensors, respectively. When  $j^e = 0$ , Eqn. 1.13 can be rewritten as

$$\alpha\sigma^{-1} = E/\nabla T, \quad (1.16)$$

thus,  $S = \alpha / \sigma$ , also known as the thermoelectric power or shortly thermopower, quantifies a tendency of an electronic system to generate an electric field in response to a thermal gradient. When  $\nabla T \parallel \hat{x}$  and  $B \parallel \hat{z}$ ,  $S_{xx}$  can then be expressed as [83]:

$$S_{xx} = \frac{E_x}{\nabla T} = \frac{\alpha_{xx}\sigma_{xx} - \alpha_{xy}\sigma_{xy}}{\sigma_{xx}^2 + \sigma_{xy}^2}, \quad (1.17)$$

In the presence of a mutually perpendicular magnetic field and thermal gradient, charged particles moving in a solid will deviate from their trajectory due to the Lorentz force. As a result, a finite transverse thermoelectric response is generated, also known as the Nernst effect. This is a manifestation of transverse entropy flow caused by longitudinal current flow [84] with Nernst signal  $S_{xy}$  given by [83]:

$$S_{xy} = \frac{E_y}{\nabla T_x} = \frac{\alpha_{xy}\sigma_{xx} - \alpha_{xx}\sigma_{xy}}{\sigma_{xx}^2 + \sigma_{xy}^2} \quad (1.18)$$

The sign of the Nernst effect is not straightforward to predict as it is determined by the difference of two contributions of similar magnitude. The situation where they are equal, hence the resulting Nernst signal is zero, is called the Sondheimer cancellation [85].

The magnetic field affects thermoelectric conductivity and according to the linear Boltzmann formalism the longitudinal and transverse response in a classical system are given by [82]:

$$\alpha_{xx} = \frac{\alpha_0}{1 + \mu B^2} \quad (1.19)$$

$$\alpha_{xy} = \frac{\alpha_0 \mu B}{1 + \mu B^2} \quad (1.20)$$

## Chapter 1: Introduction

---

where  $\alpha_0$  is zero field thermoelectric conductivity and  $\mu$  is the mobility. It is evident from Eqns. 1.15 and 1.16 that the magnitude of the thermoelectric coefficients is controlled by the product of mobility and magnetic field similar to the electrical conductance. In the weak field limit ( $\mu B \ll 1$ ), the transverse response is linear, whereas the longitudinal response is weakly field dependent.

Remarkably, N.F. Mott and H. Jones in 1936 provided the link between the thermoelectric conductivity and electric conductivity [86]:

$$\alpha = \frac{\pi k_B^2 T}{3} \frac{\partial \sigma}{\partial \epsilon} \Big|_{\epsilon = \epsilon_F} \quad (1.21)$$

This expression implies that the thermoelectric conductivity is proportional to the energy derivative of electrical conductivity, which means that relatively small variation of  $\sigma(\epsilon)$  around the Fermi level can manifest as a large change of  $\alpha$  [87].

The sign of the thermopower can be positive or negative depending on the curvature of the Fermi surface, with some exemptions, such as noble metals [82]. However, the energy dependent scattering time can affect the value of  $\alpha$  [88]. For a multiband conductor, the total thermoelectric signal is a sum of individual band contributions  $S_i$ , weighted by the respective conductivities  $\sigma_i$ :  $S = \frac{\sum_i S_i \sigma_i}{\sigma}$ .

The magnitude of thermoelectric response is proportional to  $k_B T / \epsilon_F$ , what make them useful in studies of topological semimetals where the Fermi energy is low, hence a large thermoelectric response can be expected in these materials [89] [Phys. Rev. B 99, 155123]. The magnitude of Seebeck and Nernst coefficient ( $v$ ) for a single band conductor at low temperatures is given by [82]:

$$S_{xx} = \frac{\pi^2 k_B T}{2 e T_F} \quad (1.22)$$

## Chapter 1: Introduction

---

$$\nu = \frac{\pi^2 k_B^2 T}{3 e \epsilon_F \mu} \quad (1.23)$$

Here,  $T_F$  represents the Fermi temperature, and  $e$  denotes the electronic charge.

In fact, many research groups have shown interest in studying the thermoelectric properties of topological semimetals, particularly in magnetic fields [32,37,52,63,83,84,89,90], because such measurements can be a sensitive tool to study the unconventional band structure of these materials. For instance, thermoelectrical quantum oscillations of different topological semimetals can help to probe the Fermi surface with better resolution than Shubnikov - de Hass oscillations [91]. Other phenomena associated with non-trivial topology, such as the chiral anomaly or the anomalous magneto-transport, have also been widely investigated using thermoelectrical transport [52,92].

In the end, it is worth mentioning that the thermoelectric phenomena can have other than diffusive origin. A relatively common one is phonon-drag thermoelectric power ( $S_g$ ). The temperature gradient causes phonon currents to flow from the hot to the cold end of the sample. At low temperatures, due to the large mean free path of the phonons, they can effectively pull the charge carriers along the direction of the phonon current by momentum transfer. Thus, a net charge imbalance of the sample is generated, as a result an electric field was developed to prevent further accumulation of charge carriers, which constitute as  $S_g$ . The approximate magnitude of the phonon-drag thermoelectric power in metals is given by [88],

$$S_g = \frac{C_g}{3n_0 e} \left( \frac{\tau'_p}{\tau'_p + \tau_{pe}} \right) \quad (1.24)$$

where,  $C_g$  is lattice heat capacity,  $n_0$  carrier concentration,  $\tau_{pe}$  is the relaxation of phonon due to electron-phonon coupling and  $\tau'_p$  is phonon relaxation time due to other interactions of phonon except electron-phonon. At high temperatures,  $S_g$  drastically decreases due to increasing rate of phonon-phonon scattering. Typically the maximum contribution of  $S_g$  in

metals has been observed around the temperature  $T \approx \theta_D/5$ , where  $\theta_D$  is the Debye temperature [88].

### 1.4 Motivation and objective of the thesis

The remarkable discovery of the topological insulator has led to extensive research into the topological aspects of electronic structure [8]. Soon afterwards, it has been realized that the nontrivial topology can occur in many other materials, including semimetals, which triggered another wave of research interest [11]. The electronic structure of topological semimetals hosts quasiparticles arising from band crossings between the valence and conduction bands. Manifestations of these low-energy electronic excitations can be found, among others, in unusual transport properties in presence of a magnetic field. In other words, by measuring the transport properties of topological semimetals one can probe the nontrivial topology of the electronic structure. These studies include investigations of quantum oscillations providing information about the Fermi surfaces; the anomalous Hall effect arising from non-zero Berry curvature; and the chiral anomaly consisting of charge pumping of Weyl fermions. It is worth noting that complementary transport measurements, such as thermoelectric ones, provide an exceptional opportunity to explore the properties of topological semimetals in more depth.

This work is motivated by the fact that measurements of thermoelectric coefficient appear to be very useful, though perhaps somewhat underrepresented, way of investigating the properties of topological semimetals. For instance, as suggested by the Mott formula, thermoelectric coefficients should be more sensitive to changes in energy dispersion at the Fermi level than their electrical counterparts. Therefore, the thermoelectric transport measurements can offer precise information about the Fermi surface in studies of quantum oscillations [91]. Another example is the anomalous Nernst effect, which is expected to be

## Chapter 1: Introduction

---

more sensitive to the non-zero Berry curvature than anomalous Hall effect, if Weyl nodes are not placed exactly on the Fermi level [93]. Furthermore, chiral current of Weyl semimetals can be detected using thermoelectric transport measurements without application of external electrical current, which makes it more robust to experimental artefacts [53].

Inspired by these facts, we decided to investigate properties of three topological semimetals using combined electrical and thermoelectric transport measurements. In a magnetic field, these materials were showing many unusual characteristics. For example, TaAs<sub>2</sub> is expected to become a Weyl semimetal when a magnetic field is applied [94], which should induce an additional phase in the electron wave functions. This, in turn, will affect quantum oscillations and can result in emergence of the spin-zero effect [95]. The ferromagnetic Weyl semimetal CeAlSi, on the other hand, has been identified as a new type of topological material, where the Weyl points arise from broken inversion symmetry. By breaking time-reversal symmetry, these points can be shifted in k-space making CeAlSi an intriguing object to study the interaction between magnetism and topology [96]. Hence, in this material we chose to look for the anomalous Hall effect and the complementary anomalous Nernst effect. In the latter, the response to the non-zero Berry curvature is different from that of the anomalous Hall effect, allowing some conclusions to be drawn about the position of the Fermi level. Finally, we have selected an elemental  $\alpha$ -Sn in a form of a strained thin film to study the quantum anomaly, whose manifestations were found by our colleagues in electrical measurements [97]. The electronic structure of strained  $\alpha$ -Sn thin film has a pair of Dirac cones are protected by four-fold rotational symmetry [28], but the application of magnetic field turns  $\alpha$ -Sn into a Weyl semimetal. This makes  $\alpha$ -Sn a suitable candidate to investigate the chiral anomaly, which, if true, should also be seen in thermoelectric transport.

## EXPERIMENTAL SECTION

Various experimental techniques can be deployed to study topological nontrivial material. In this thesis, I will focus on measurements of transport and thermoelectric properties, but in order to obtain reliable results to draw solid conclusions, high-quality samples are needed first and foremost. These samples can be grown in bulk or thin film form. We studied two bulk single crystals, namely TaAs<sub>2</sub> and CeAlSi grown by chemical vapor transport and self-flux method respectively. We also measured a single-crystalline thin film of  $\alpha$ -Sn fabricated by molecular beam epitaxy (MBE).

This chapter will be structured as follows. First, I will give a brief description of the techniques used to grow the single crystals selected for measurements. Next, I will give a brief description of our cryostat, which is equipped with a superconducting coil capable of generating a 14.5/16 T magnetic field. Subsequently, I will introduce our self-made electrical and thermoelectric probes. Finally, I will discuss the sample preparation and the procedure of electrical and thermoelectric measurements.

### 2.1 Single crystal growth techniques

In order to obtain high quality samples, we collaborated with three different experimental research groups. Two of them are from Institute of Physics, Polish Academy of Sciences (IF PAN), Poland, and one from the Boston College, USA. TaAs<sub>2</sub> and  $\alpha$ -Sn were grown by the MagTop ON6.1 group at IF PAN, while the magnetic Weyl semimetal CeAlSi was synthesized in the Tafti Lab at Boston College, USA.

### 2.1.1 Chemical vapour transport method

Chemical vapour transport (CVT) is a widely used method for growing high purity single crystals [98]. In the simplest of terms, this process requires reactants, a transport agent (typically elemental halogens) and a temperature gradient. A schematic description of the CVT is shown in Figure 2.1, and the principle of the process can be described as follows. Initially, a precursor is mixed with a transport agent and kept in a vacuum sealed quartz ampoule. This ampoule is then placed in an oven and subjected to a temperature gradient. Initially, the transport agent sublimates and reacts chemically with the precursor in the quartz ampoule, which converts the solid form of a precursor into a gaseous derivative. The temperature gradient forces the gaseous derivative to migrate either from the hot zone to the cold zone ( $T_2 \rightarrow T_1$ ) or vice versa ( $T_1 \rightarrow T_2$ ), depending on the nature of the reaction between the precursor and transport agent. Finally, crystallization takes place in the cold zone ( $T_1$ ) if the reaction was endothermic, whereas while it take places in the hot zone ( $T_2$ ) if the reaction was exothermic.

TaAs<sub>2</sub> single crystals were prepared by two stage CVT. Initially, polycrystalline TaAs<sub>2</sub> was synthesized using direct reaction of Tantalum foils (ZR Industrial Ltd, 99.99%) and Arsenic (PPM Pure Metals, 99.999995%) in a vacuum sealed in a quartz tube. This reaction occurs at the temperature of 990 °C and takes 19 days in a furnace. The furnace is then cooled down to room temperature and polycrystalline TaAs<sub>2</sub> is extracted from the quartz tube.

To make single crystals, polycrystalline TaAs<sub>2</sub> was first palletized and then placed inside the vacuum-sealed quartz tube along with iodine (transport agent). The temperature gradient is then applied to the quartz tube in a furnace. The source zone ( $T_2$ ) was kept at 1025 °C, while the sink zone ( $T_1$ ) was kept at 956 °C for 23 days. The furnace was then cooled down to room temperature at a rate of 100 °C/h and the single crystals of TaAs<sub>2</sub> can be

## Chapter 2: Experimental Section

---

extracted from the sink zone. For more details on the growth and characterization of TaAs<sub>2</sub>, see Ref. [99].

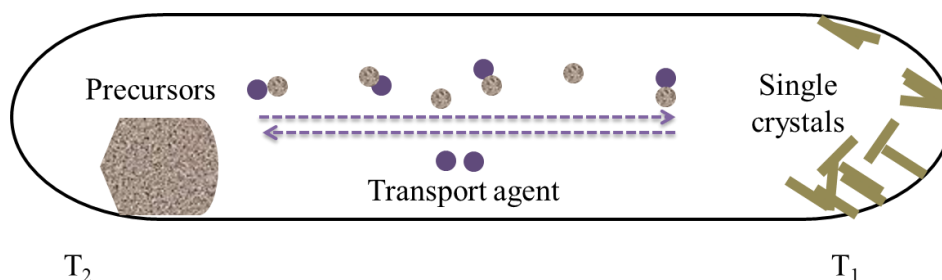


**Figure 2.1.** A schematic representation of chemical vapour transport method.

### 2.1.2 Flux method

The flux method is a long known and still very popular technique for growing single crystals, in which a low melting point solvent (flux) is used to dissolve the solute. First, a high-melting crucible filled with a solute is placed in a furnace. The oven temperature is increased to completely dissolve the solute and left for some time to obtain a homogeneous solution. The next step is to lower the temperature at a specific rate to reduce the solubility of the solute. This continues until the supersaturation point is reached, where the concentration of the solute is greater than its solubility. At this instant, small nuclei begin to grow and, with further temperature reduction, these nuclei fuse together, eventually leading to the formation of crystals. The residual flux can be removed with a solvent (e.g. by using hot dilute nitric acid for several days) or quickly decanted by centrifuge while still in the liquid phase.

Self-flux method used to grow CeAlSi single crystals is called the "self-flux method" because the flux components are the same as in the desired compound. Initially Ce, Al and Si were mixed in a weight ratio of 1:10:1 in a Canfield crucible. This crucible was then sealed and placed inside a quartz tube evacuated using a vacuum pump. Subsequently, the sealed quartz tube is placed inside a furnace, heated to 1000 °C at a rate of 3 °C/h and held for 12 h. Cooling was then commenced to 700 °C at a rate of 0.1 °C/h and the held for 12 h. The

## Chapter 2: Experimental Section

residual flux was removed and then crucible was rapidly cooled to room temperature. More detailed information on the preparation of CeAlSi can be found in Ref. [96].

### 2.1.3 Molecular beam epitaxy

The molecular beam epitaxy (MBE) machine offers a number of capabilities that are beneficial for the growth of high-purity epitaxial layers. For example, the inner space of the system is kept at the ultra-high vacuum (UHV) to ensure efficient deposition of high purity epitaxial layers with in-situ reflection high-energy electron diffraction (RHEED) capability. The latter allows accurate monitoring of the growth process [100]. A generic diagram showing a simplified principle of the MBE machine is presented in Fig. 2.2.

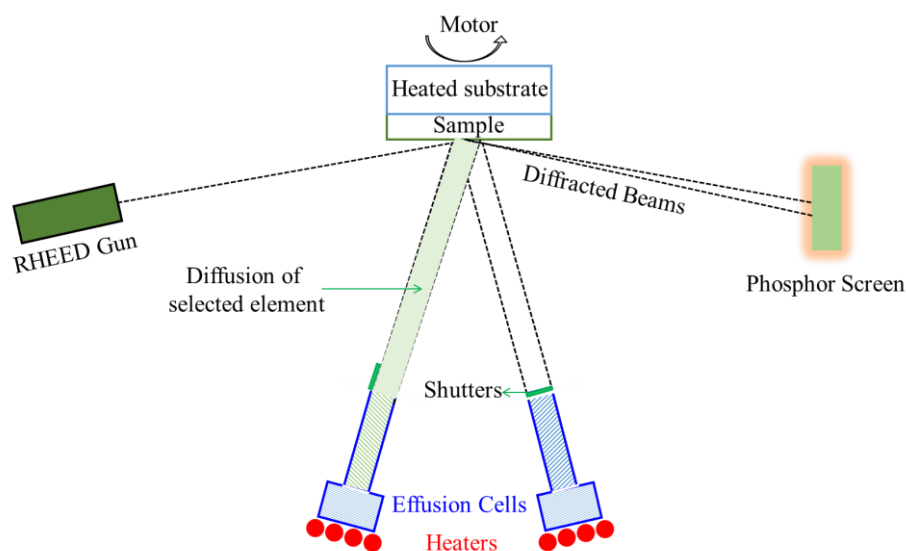


**Figure 2.2.** A simplified schematic representation of molecular beam epitaxy used for the growth of  $\alpha$ -Sn thin film.

At the bottom of the UHV chamber, two or more effusion cells or Knudsen effusion cells (K-cells) are installed which comprise of crucibles in order to hold the source elements. One of the important requirements for successful layer growth is the capability to generate stable, reproducible and uniform molecular beams of elemental constituents [101]. The K-

## Chapter 2: Experimental Section

---

cells are directed towards the substrate to place pure element on the substrate. The precursors held in the effusion cells are heated up and sublimated which are then transferred to the heated sample holder in the form of molecular beams. In case of liquid source materials, the starting elements are evaporated and beamed in the same pattern as for solid precursors. Heating of the effusion cells is typically achieved by using either resistive or electron beam energy source [101]. The choice is based on the required flux and the melting point of the source material stored in the crucibles. The effusion cells are armed with shutters to control deposition of the substances. Once they are open, physical vapour from each K-cell is diffused towards the substrate to deposit a layer. In a typical MBE chamber, the sample holder consists of a heating source and a sample rotating component which is used to achieve uniform growth of the films. The RHEED gun is used to characterize the deposited layers in-situ during the growth process. The gun emits electrons at a very low angle with respect to the sample's surface which produce a diffraction pattern. The in-situ RHEED characterization can yield information about surface structure, cleanliness, smoothness and growth rate [102], which helps in understanding the details to produce a sample with the preferred properties.

For our study,  $\alpha$ -Sn thin film was grown on GaAs (001) substrate with 4  $\mu\text{m}$  CdTe buffer layer. The desired lattice mismatch between CdTe and  $\alpha$ -Sn incorporates an in-plane compressive strain ( $\sim 0.1\%$ ) in  $\alpha$ -Sn, leading to the formation of a Dirac semimetallic phase (DSM). Detailed description of the growth procedure and structural information available in Ref. [97].

### 2.2 High field cryogenic system

High magnetic field and low temperatures are highly desirable conditions to study the quantum transport properties of materials. The former can drive an electronic system to extreme states, such as a quantum or chiral limit, while the latter reduces the thermal

## Chapter 2: Experimental Section

---

broadening of energy levels and allows one to measure low energy quantum phenomena . All the transport measurements data presented in this thesis were measured in a high magnetic field cryostat system. The superconducting electromagnet coils were manufactured by Cryogenic Consultant Limited, while the cryostat was manufactured by KrioSystem. A schematic representation of our High field cryogenic system shown in Fig.2.3. Here I will shortly discuss key components of the experimental rig and its operating procedures.

We used a “wet” passive cryogenic system that required filling with liquid helium (LHe) to operate. To reduce a heat exchange between the inner and outer space of the cryostat they were separated with vacuum jackets and the liquid nitrogen (LN<sub>2</sub>). While high vacuum prevents a convective and diffusive heat transfers, the thermal radiation was reduced by multiple layers of mylar foil (also referred to as a superinsulation). To further reduce the thermal radiation, the nitrogen tank (jacket) was installed in such a way that it surrounds the inner vessel. This was filled with LHe in which the superconducting coil was immersed. At the boiling temperature of helium at atmospheric pressure (4.2 K for <sup>4</sup>He ) the superconducting coil was able to generate a magnetic field of ±14.5 T, which allowed us to study the magneto-transport in a wide range of conditions. To control the temperature of a sample we used the variable temperature insert (VTI) into which a sample probe was inserted. LHe from the main bath was sucked to VTI through a needle valve, after which it was transformed into gas of desired temperature at a heat exchanger and drawn to the sample space. The temperature of the heat exchanger was measured by Rhodium Iron (RhFe) thermometer and controlled by a resistive heater. An evacuation port (located at the top flange of the VTI) was connected to a rotary pump that allowed us to keep the gas pressure in VTI below atmospheric pressure.

There are several steps needed to be performed to prepare a system for measurements. To maintain high vacuum in vacuum jackets of cryostat and VTI we used Edwards pump

## Chapter 2: Experimental Section

---

station that was set of a scroll and turbo molecular pump. We pumped the vacuum for a few days and waited for the pressure to reach  $10^{-6}$  mbar before cooling the system. Next we filled the nitrogen jacket with LN<sub>2</sub> and waited until the superconducting coil cooled down to a temperature of about 160 K through thermal radiation. This cooling process took at least 72 hours, but allowed us to keep the main bath filled with helium gas. During this process the coil temperature was monitored by another RhFe thermometer, which was attached to the lambda plate placed above the superconducting coil. After reaching the desired temperature, we could start filling the helium reservoir with a liquid through a double sided transfer tube by ICE Oxford. The level of LHe was monitored by a liquid helium level meter DLG200 constructed by Cryogenic Consultant Ltd. An exhaust port at the head of the cryostat was connected to the recovery line to continuously release the overpressure of the helium gas from the reservoir.

When the system was filled with LHe the sample probe could be inserted inside VTI. In order to easily regulate the flow of helium through the originally manual needle valve during measurements, we connected it to a stepper motor controlled from a personal computer (PC). An additional electronic valve by Leybold (also controlled from PC) was attached to the pumping line to fine tune the He pressure inside the VTI. This was monitored by an electronic pressure gauge by Leybold which, like all other instruments, was read and controlled by measurement software that was written and run in the National Instrument Labview environment.

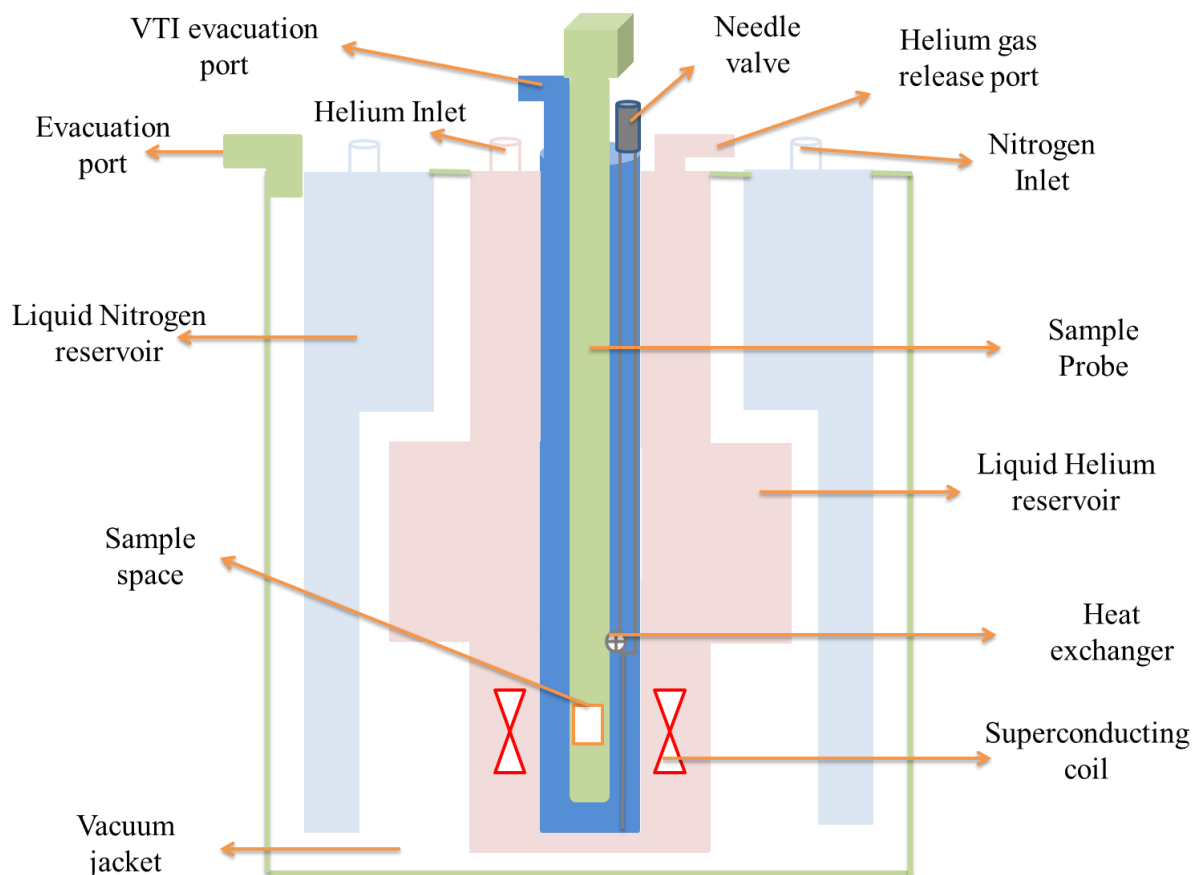


**Figure 2.3.** A schematic representation of the cryogenic system.

### 2.3 Electrical probe

Electrical transport properties were measured using a custom-made probe equipped with a sample holder allowing 360° rotation of the sample. It is shown in Figure 2.4, where three panels present the three different segments of the probe. The left section shows the head of the probe fitted with a rotary knob that allows us to manually control the angle of the sample tilt with high precision. The actual position can be read from the dial. Below, the probe has installed five copper discs five copper disks are installed to prevent radiative heat transfer to the sample from the top of the probe being at room-temperature. For the electrical connection, a set of twisted pairs made of thin copper wire are used. These wires connected to the external devices through a multi-pin hermetic connector shown in the center panel of

## Chapter 2: Experimental Section

Fig.2.4. The most important part of the probe, shown in the right panel of the Fig. 2.4. The sample holder consists of an 8-pin socket connected to a wheel, the position of which is controlled by the knob. To accurately determine the sample temperature, a Cernox thermometer is attached to the sample holder.

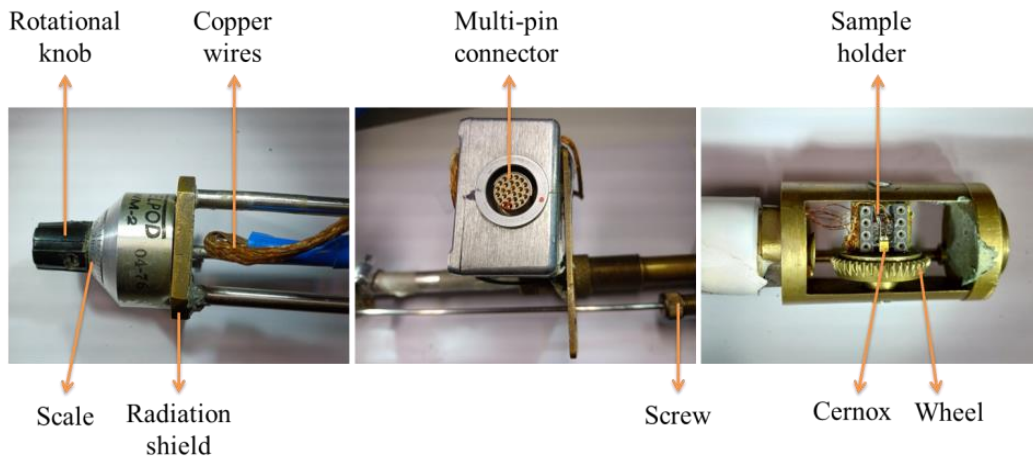


**Figure 2.4.** Different parts of our hand crafted electrical probe

### 2.4 Thermoelectric probe (TEP)

Thermoelectric coefficients are measured with another custom-made probe. I will again discuss its construction by describing the three segments - these are shown in Figure 2.5. The head of the probe shown in Figure 2.5a consists of a vacuum port, a stepper motor connector and a multi-pin sample connector. Figure 2.5b presents the base of the probe, where we have 16 pairs of coils made of 25  $\mu\text{m}$  thick phosphor - bronze wire for the electrical connections. These are connected to twisted pairs made of 50  $\mu\text{m}$  copper wire leading to the top of the probe. To prevent electrical shortcuts between twisted pairs and the probe, a cigarette paper was glued to the tube, which joins the head and base of the problem and Teflon tape was wrapped around. The twisted-pair cables are fed into the base via a vacuum-tight electrical conduit prepared using a Stycast 2850FT epoxy. The base consists of several components, including a beryllium oxide chips for connections, a couple of gears and the

## Chapter 2: Experimental Section

sample space. The beryllium oxide chips, due to their high thermal conductivity, are used as thermal anchors to equalize temperature of the wires. The gears made of brass are controlled by the stepper motor allow us to measure the angular variation ( $\pm 180^\circ$  out-of-plane) of thermoelectric coefficients. An enlarged view of the sample space is presented in Figure 2.5c. Two phosphor - bronze blocks are fixed together using Vespel fittings and tensioned with a stainless spring – a sample is mounted between them. In order to induce a thermal gradient along the sample we used resistive heater of 10 k $\Omega$  resistance glued with GE varnish into one of the blocks. For determination of temperature gradient two Cernox thermometers were attached to the Ph-Br blocks using Stycast 2850FT epoxy. Figure 2.5d shows the brass can that was used to seal the base of the probe to make it vacuum-tight.

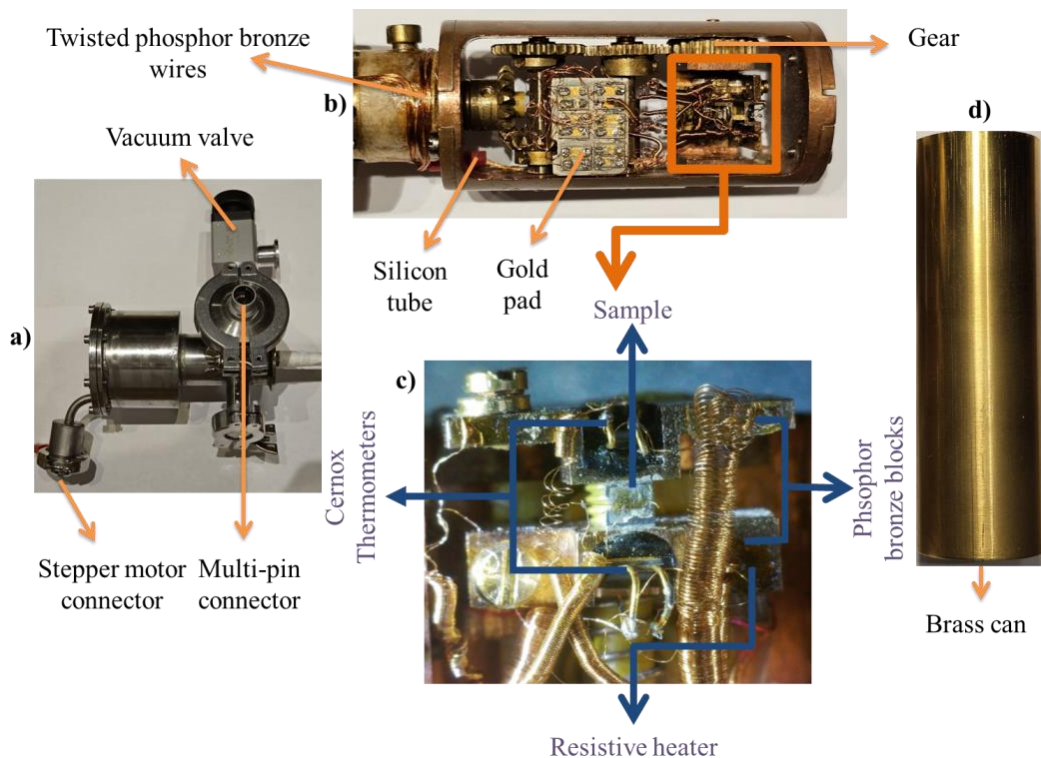


**Figure 2.5.** Sections of our custom-made thermoelectrical probe

### 2.5 Electrical transport measurements

In the past decade, many unusual electrical transport phenomena have been reported in topological semimetals. For example, in the presence of a magnetic field ( $B$ ) observation of changes to the electrical resistivity (i.e. magnetoresistance, MR) and Hall resistivity provide opportunity to study the extraordinary behavior of Dirac and Weyl fermions. We measured the temperature dependences of the resistivity for all materials studied and also magnetic field dependences of the magnetoresistance and Hall resistivity for several fixed temperatures. To determine the longitudinal and transverse electrical signals we used contacts arranged in the standard Hall bar configuration shown in Fig. 2.6.

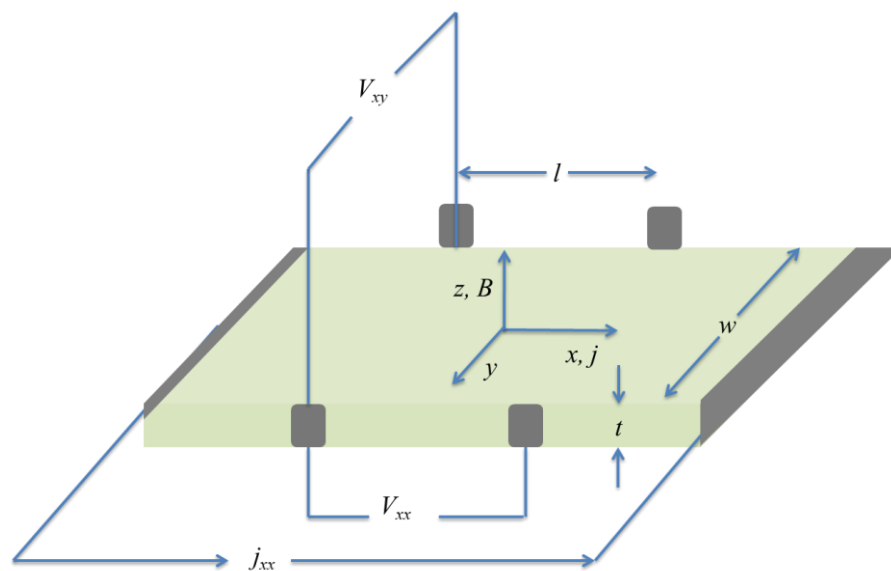


**Figure 2.6.** A typical schematic diagram of the Hall bar geometry. A constant current ( $j_{xx}$ ) is injected along the longest side, the x-axis of the sample. The magnetic field ( $B$ ) is applied perpendicular to the surface of the sample, i.e. z-axis. The generated longitudinal ( $V_{xx}$ ) and transverse ( $V_{xy}$ ) voltages were recorded using a Nanovoltmeter.

## Chapter 2: Experimental Section

---

The electric field governed by the relation  $E = \rho j$ , when a mutually perpendicular current ( $j_x$ ) and magnetic field ( $B_z$ ) applied to sample, here  $\rho$  is the resistivity rank 2 tensor quantity,  $E$  and  $j$  are the vectors. Hence, in terms of Einstein notation, this relation further can be expressed as  $E_i = \rho_{ij}j_j$ , where  $i, j$  in the subscript represent the component of electrical resistivity, electric field and the current. The matrix representation of this expression can be written as:

$$\begin{pmatrix} E_x \\ E_y \\ E_z \end{pmatrix} = \begin{pmatrix} \rho_{xx} & \rho_{xy} & \rho_{xz} \\ \rho_{yx} & \rho_{yy} & \rho_{yz} \\ \rho_{zx} & \rho_{zy} & \rho_{zz} \end{pmatrix} \begin{pmatrix} j_x \\ j_y \\ j_z \end{pmatrix} \quad (2.1)$$

Now restricting the current flowing into  $x$  direction only and eliminating the  $z$  component of  $E$ ,  $\rho$  and  $j$ , as a result Eqn.2.1 can be rewritten as,

$$\begin{pmatrix} E_x \\ E_y \end{pmatrix} = \begin{pmatrix} \rho_{xx} & \rho_{xy} \\ \rho_{yx} & \rho_{yy} \end{pmatrix} \begin{pmatrix} j_x \\ 0 \end{pmatrix} \quad (2.2)$$

Including the sample dimensions:  $l$  (the length between two longitudinal electrical contacts),  $w$  (width) and  $t$  (thickness) Eqn. 2.2 can be expressed in terms of voltages  $V_{xx}$  and  $V_{xy}$ :

$$\begin{pmatrix} \frac{V_{xx}}{l} \\ \frac{V_{xy}}{w} \end{pmatrix} = \begin{pmatrix} \rho_{xx} \\ \rho_{yx} \end{pmatrix} \frac{j}{w * t} \quad (2.3)$$

From the above relation, the longitudinal and Hall resistivity can be calculated respectively as:

$$\rho_{xx} = \frac{V_{xx}}{j} * \frac{w * t}{l} \quad (2.4)$$

$$\rho_{yx} = \frac{V_{xy}}{j} * t \quad (2.5)$$

To separate the electrical signal into field-symmetrical (magnetoresistance) and anti-symmetrical (Hall resistivity) components, we need to measure  $\rho_{xx}$  and  $\rho_{yx}$  in both positive and negative magnetic fields. Thus, the final form of longitudinal and Hall resistivities can be expressed as:

$$\rho_{xx}(B) = \frac{\rho_{xx}(+B) + \rho_{xx}(-B)}{2} \quad (2.6)$$

$$\rho_{yx}(B) = \frac{\rho_{yx}(+B) - \rho_{yx}(-B)}{2} \quad (2.7)$$

### 2.5.1 Sample preparation

To measure  $\rho_{xx}$  and  $\rho_{yx}$ , we need a suitable bar- or plate-like shaped single crystal. To this end we cut the bulk single crystals using a wire-saw. The sample attached to a suitable plastic sample holder with GE varnish. In this process, a tungsten wire continuously performs a reciprocating motion against the surface of the sample that is coated with a dripping mixture of glycerin and alumina powder ( $\text{Al}_2\text{O}_3$ ). The abrasive particles remove the material and the liquid acts also as a coolant to prevent overheating due to friction between wire/alumina and a sample. After cutting a sample to suitable dimensions, it needs to be properly cleaned before making the electrical contacts. The cleaning process has couple of steps, including washing in acetone ( $\text{C}_3\text{H}_6\text{O}$ ) to soften the adhesive glue which can then be removed with tweezers. After acetone treatment, the remaining residue is removed by soaking a sample in ethanol ( $\text{CH}_3\text{CH}_2\text{OH}$ ) bath for 15-20 minutes. Ethanol can dissolve the both polar and nonpolar molecules, can effectively remove the unwanted contaminants those were embedded onto surfaces of the samples. The cleaned sample is then ready to make electrical contacts.

A typical example of Hall bar contacts made on a sample is shown in Figure 2.7. To mount a sample we used an 8 legs puck with a mica flake (that is electrically insulating) as a base. Mica sheet is electrically and thermally insulating, preventing additional unwanted signals during the measurements. A double-sided cellulose tape was placed on top of the mica to gently hold the sample and six electrical connections (two of them used for current and four served as voltage contact) using 25  $\mu\text{m}$  thick gold wires were made. These gold wires were attached to the pin of puck with indium using a soldering-iron. We use indium as a

## Chapter 2: Experimental Section

---

soldering agent as it does not easily dissolve gold, has a low melting point (156.7 °C) and is very ductile. The other ends of the gold wires were attached to the sample with DuPont 4929N silver paint. After making appropriate electrical connections, we ensured that the resistivity is within several Ohms range.

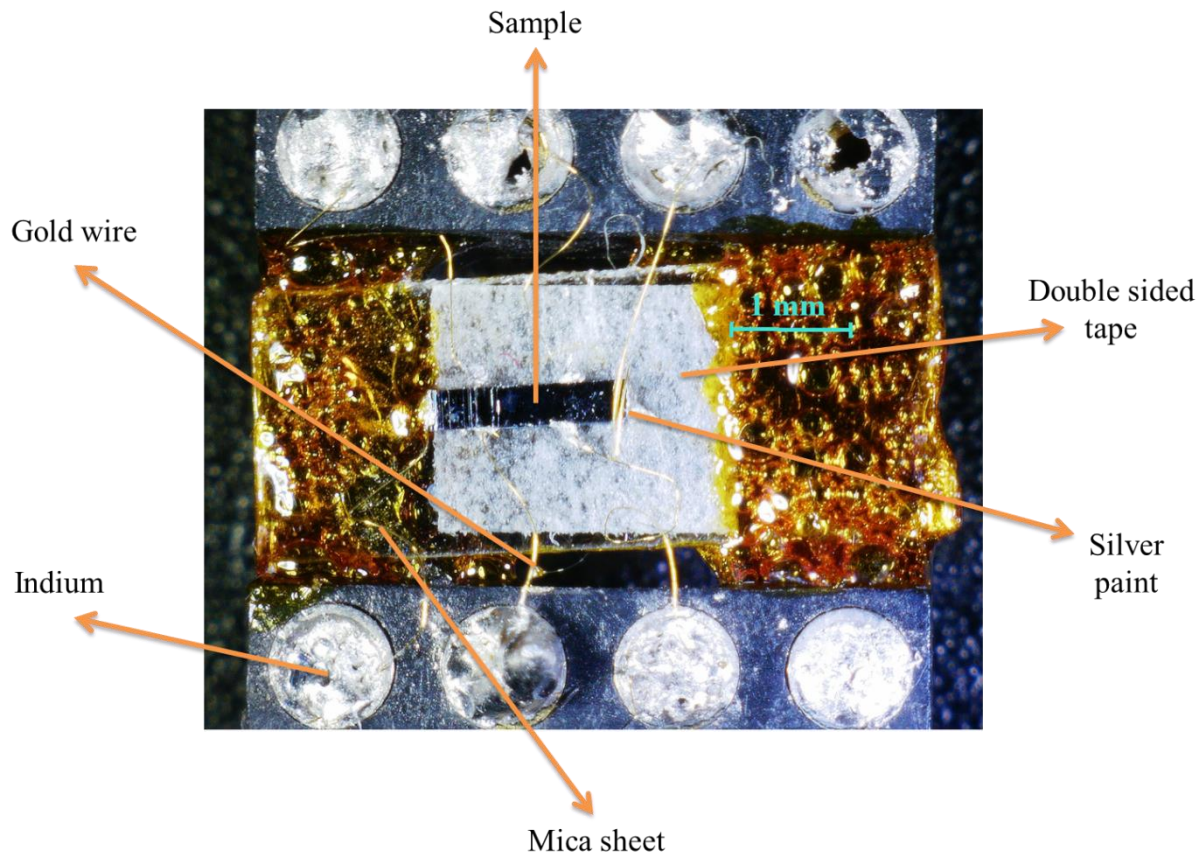


**Figure 2.7.** An example of a single crystalline sample prepared for the electrical measurements.

### 2.5.2 Measurements

Properties of a sample were investigated using a high magnetic field cryostat system, and a schematic representation of the entire magnetoelectric transport system is shown in Figure 2.8. This setup allowed us to measure the electrical properties in the temperature range from 1.7 to 300 K and in the magnetic field up to 14.5 T. The prepared sample was mounted in the electrical probe, which was then inserted into the cryostat system for measurements. The electrical measurements were performed using a four probe method. In this process, the

## Chapter 2: Experimental Section

electrical current was injected to the sample through a Keithley 6221 current source, the voltages were determined using Keithley 2182A nanovoltmeter and the sample temperature were recorded with a Lakeshore 332 temperature controller. The temperature of the VTI base was varied with a heating element controlled by another Lakeshore 332 temperature controller. MR and Hall measurements were done simultaneously in the presence of a magnetic field at several temperatures in between 1.7 to 300 K. The magnet was powered by a power supply IPS 120, which can provide a bipolar current of  $-97 \text{ A} \leq j \leq +97 \text{ A}$ , leading to generation of a magnetic field of  $-14.5 \text{ T} \leq B \leq 14.5 \text{ T}$ . This power supply can also operate the magnet in either non-persistent or persistent mode. The latter was used to acquire data on temperature sweeps at a constant magnetic field. All the instruments were interfaced with Labview to PC to control condition of the experiment and to collect the data.

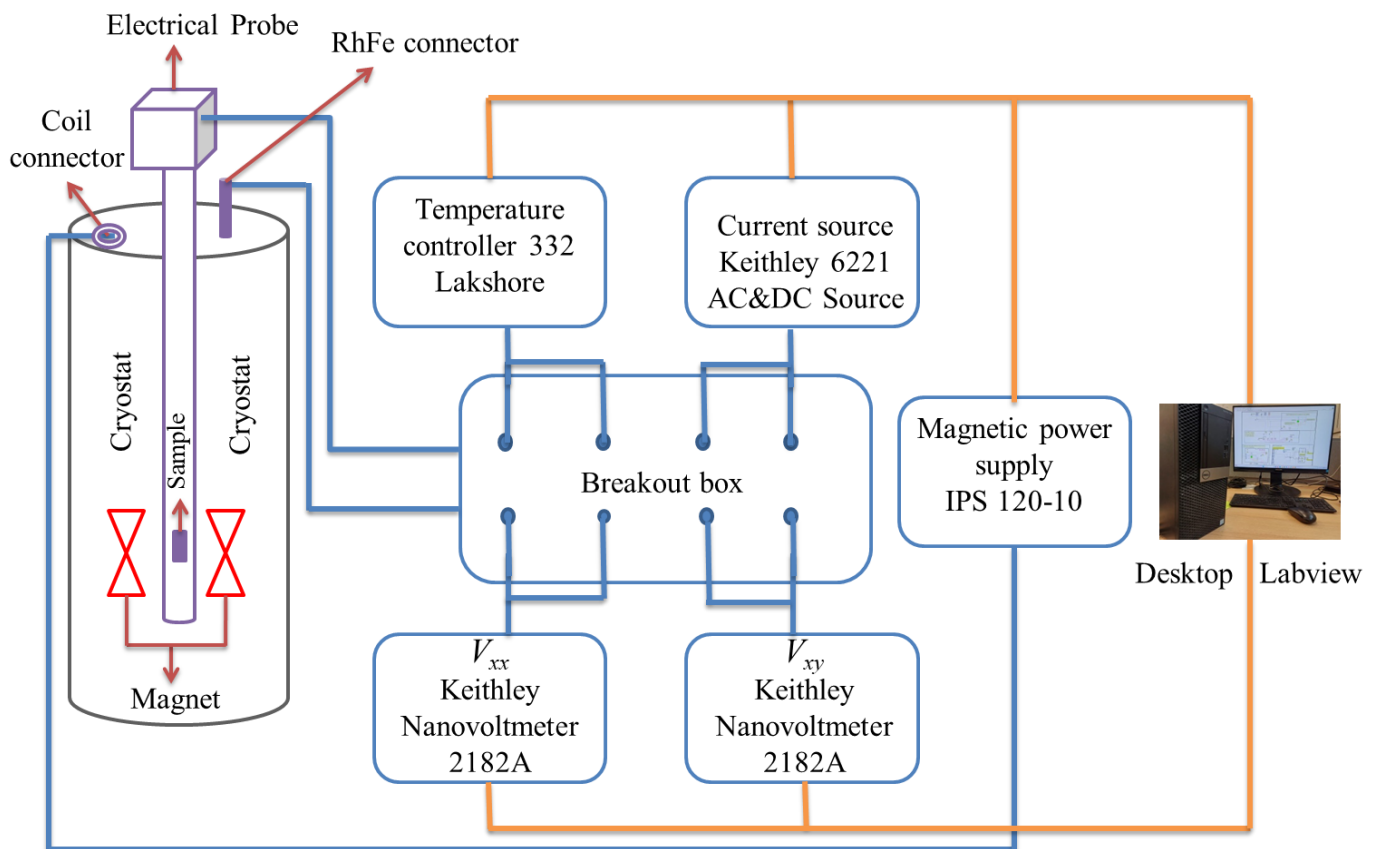


**Figure 2.8.** Schematic diagram of the magnetoelectric measurement setup. Blue lines denote electrical connections, orange ones denote data transfer.

### 2.6 Thermoelectrical transport measurements

The thermoelectric measurements can be seen as a relative of electrical transport measurements – they probe the same electronic system and the relevant coefficients are linked, for example through the Mott relation (discussed in detail in chapter 1). However, the former are often more sensitive to details of the electronic structure. The schematic diagram of the experimental setup for measurements of the thermoelectric power and Nernst effect is shown in Figure 2.9. The application of thermal gradient ( $\nabla_x T$ ) to a sample causes charge particles to drift from the hot end ( $T+\Delta T$ ) to cold end ( $T$ ), resulting in thermoelectrical current. As we carried out measurements in an open circuit configuration, this drift is offset by the appearance of the electric field, which is effectively measured as the voltage ( $V$ ) across the sample. The thermopower ( $S$ ) is defined as the ratio of developed longitudinal voltages ( $V_x$ ) to the temperature difference ( $\Delta_x T$ ):

$$S_{xx} = \frac{V_x}{\Delta_x T} \quad (2.8)$$

Subjecting of a sample to a mutually perpendicular thermal gradient and magnetic field ( $B_z$ ), results in development of a transverse voltages perpendicular to both  $\nabla_x T$  and  $B_z$ . The phenomenon is called the Nernst effect and the Nernst signal is denoted by  $S_{xy}$ :

$$S_{xy} = \frac{V_y}{\Delta_x T} \quad (2.9)$$

During the measurements of the thermoelectric coefficients, it was observed that the data always contained mixed contributions from longitudinal to transverse signals due to the asymmetric position of the contacts. Therefore, for the magnetic field dependences it was necessary to symmetrize the thermopower data and anti-symmetrize the Nernst data. The results can be presented in the following form:

$$S_{xx}(B) = \frac{S_{xx}(+B) + S_{xx}(-B)}{2} \quad (2.10)$$

$$S_{xy}(B) = \frac{S_{xy}(+B) - S_{xy}(-B)}{2} \quad (2.11)$$

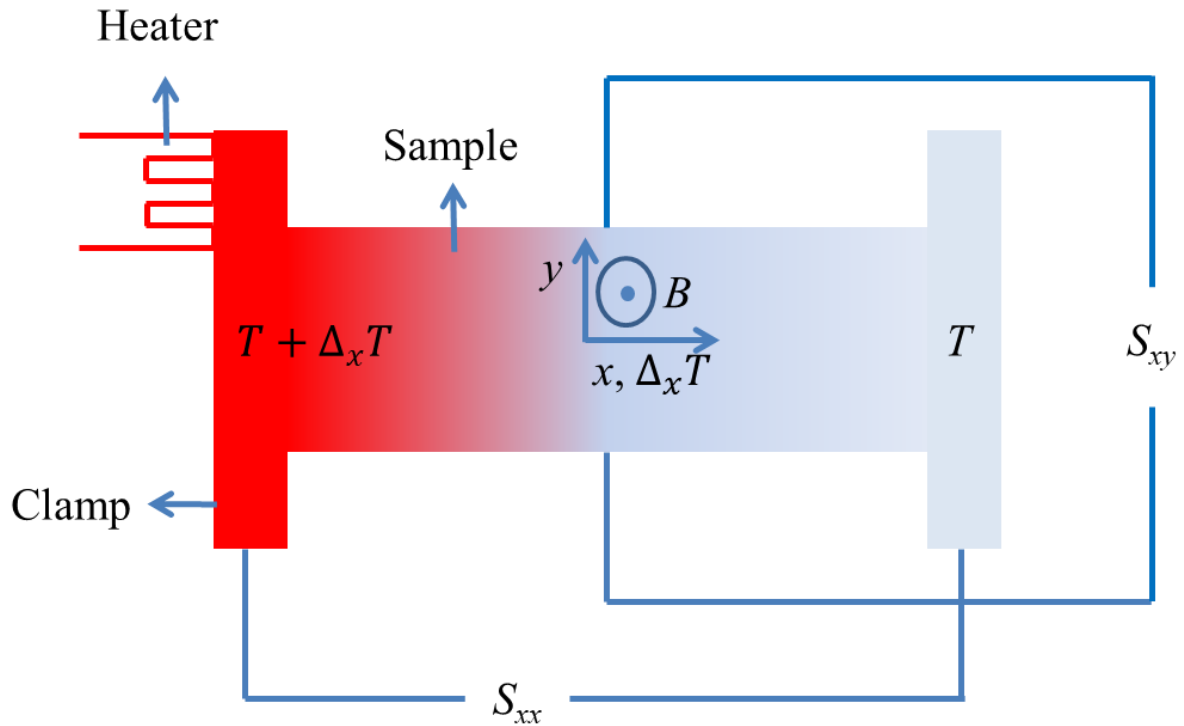


**Figure 2.9.** A schematic representation thermopower and Nernst effect.

### 2.6.1 Sample preparation

For thermoelectric measurements, we need a sample with a similar plate shape as for electrical measurements. Actually, in most cases, we performed set of the experiments on the literally same sample. To measure the thermoelectric power the sample was placed between two phosphor bronze clamps that were used as longitudinal voltage contacts. For the Nernst effect measurement, we made two transverse electrical contacts of 25  $\mu\text{m}$  thick gold wires attached to sides of the sample with Dupond 4929N silver paint. Gold wires were fixed to the the surface of the sample through cigarette paper to improve their mechanical stability. Figure

## Chapter 2: Experimental Section

2.10. Illustrates the sample preparation of a Single crystal of TaAs<sub>2</sub> to determine its thermoelectric properties.

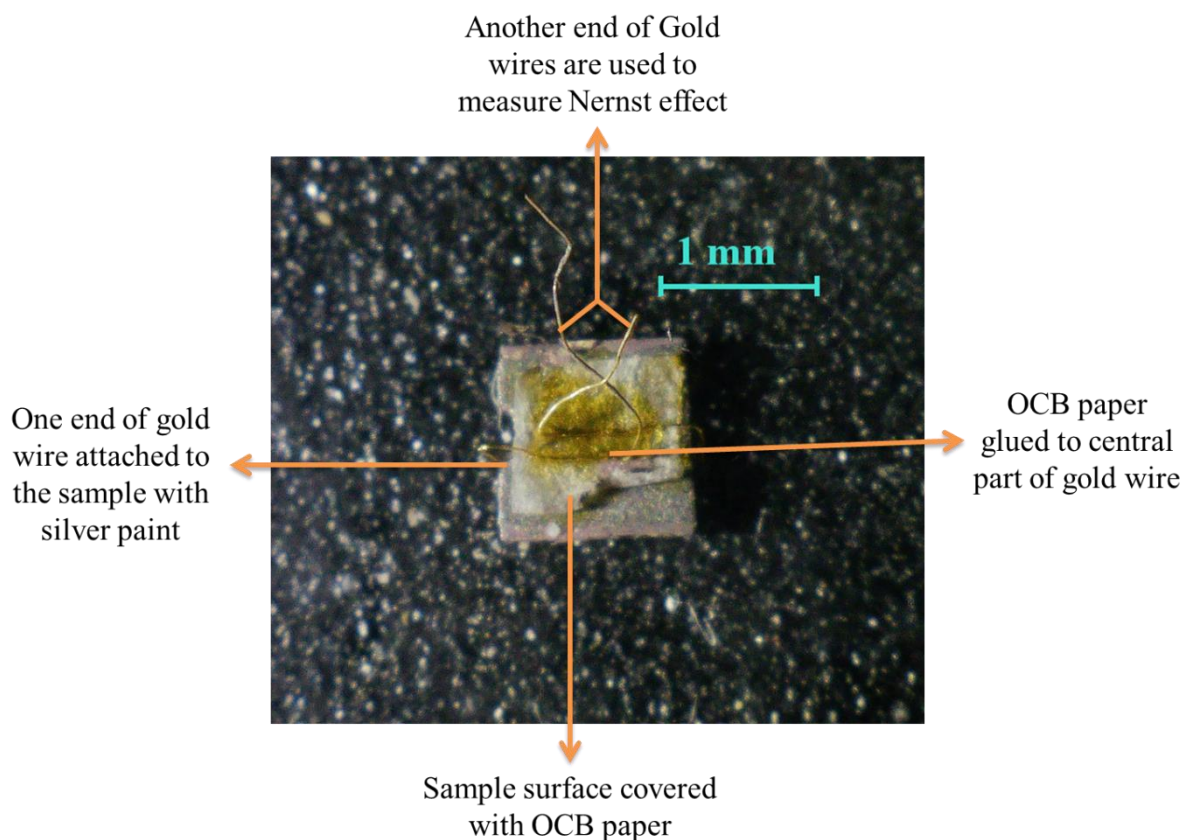


**Figure 2.10.** A Single crystal of TaAs<sub>2</sub> was prepared to determine its thermoelectric properties.

### 2.6.2 Measurements

The thermoelectric properties were determined using a probe of our own design. The prepared sample was mounted between the phosphor bronze clamps in the thermoelectrical probe. For making proper electrical connection, inevitable void space between sample and clamps was also filled with the silver paints. Other end of the gold wires was connected to the phosphorbronze wires which were already there in the probe to measure the Nernst effect. After assuring that we had proper electrical connections to the sample, the thermoelectric probe was sealed with a vacuum tight brass can. The vacuum port of the probe was connected to the Edwards pumping system, and we evacuated the probe until the pressure inside reached

## Chapter 2: Experimental Section

---

approximately  $10^{-6}$  mbar, and this process takes around 24 hours. However, in order to increase the rate of temperature equalization, we allowed a very small amount of He gas into the internal volume of the probe before the measurement. A schematic diagram of thermoelectric measurements setup Figure 2.11. The thermoelectric probe was then inserted into the VTI for measurements in temperature between 1.7 and 300 K that was controlled using a LakeShore 332. Thermal gradient along the sample was induced using a strain gauge resistive heater excited with current from a Keithley 6221 current source. The temperature of the sample and temperature difference between its ends were determined using two Cernox thermometers glued with Stycast 2850FT to the clamps. Temperatures were recorded using a temperature controller LakeShore 332, while the voltage difference along the sample was detected using Keithley 2182A nanovoltmeter. The magnitude of transverse thermoelectric voltage was usually small, therefore we used EM Electronics A20a DC nanovolt amplifier to amplify the signal, which was then recorded with a Keithley 2182A. We have measured the temperature dependences of thermopower utilizing a heater ON/OFF method, while for field sweeps the heater was always ON. During the measurements of magneto-thermopower and Nernst effect, the superconducting coils were powered by the IPS 120 power supply, allow us to measure the thermoelectric coefficients up to  $\pm 14.5$  T magnetic field.

The angular variation of the magnetothermal power and the Nernst effect at different temperatures was also measured. The angle between the sample and the magnetic field was varied by changing the position of the sample. This was achieved using a stepper motor connected to a thermoelectric probe controlled by a microprocessor controller. All instruments used in the thermoelectric set-up are connected to LabView for communication and control.

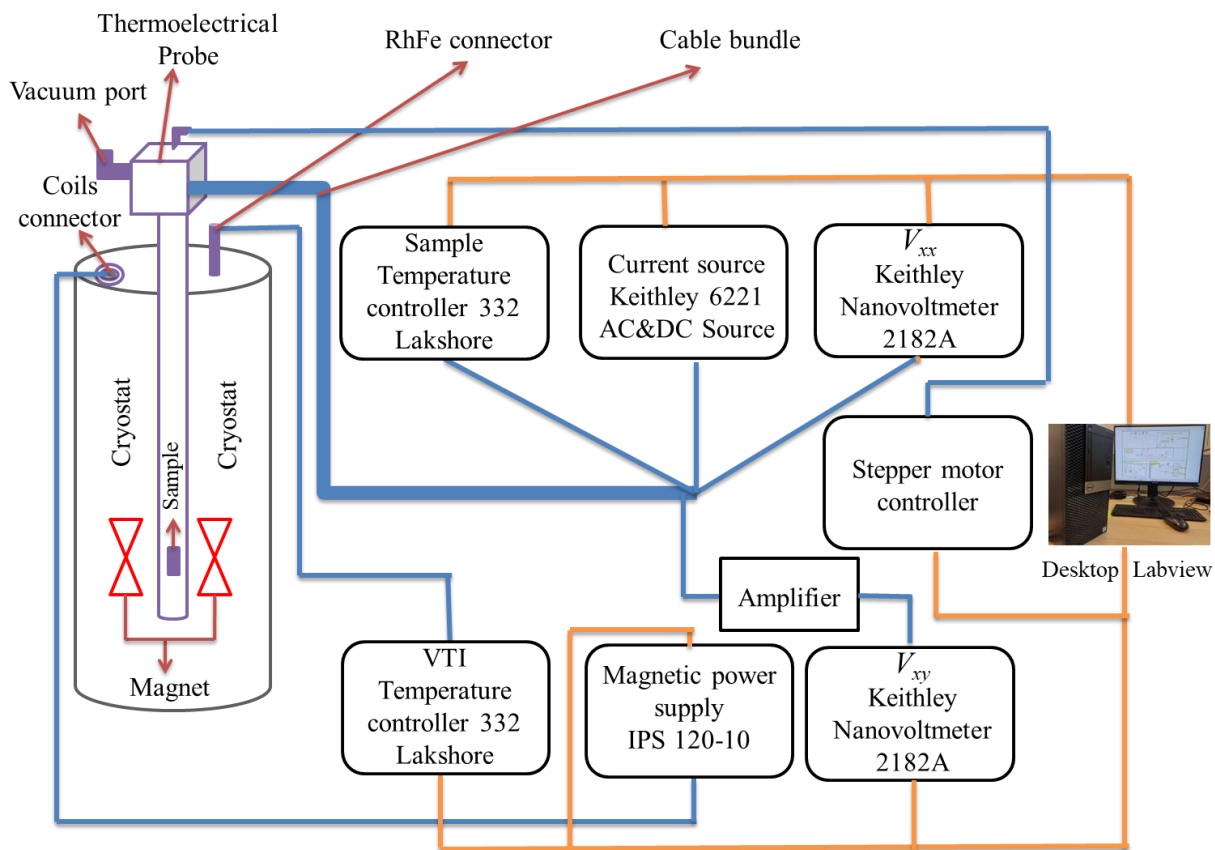


**Figure 2.11.** A schematic diagram of thermoelectric measurements setup. Blue lines denote electrical connections, orange ones denote data transfer.

### 2.7 Calibration of TEP

To subtract the back ground signal from leads of the TEP , we have measured the thermopower ( $S$ ) of a high temperature superconductor  $\text{EuBa}_2\text{Cu}_3\text{O}_{7-d}$ , which has  $S = 0 \mu\text{V/K}$  up to critical temperature ( $T_c$ )  $\sim 90\text{K}$ . Temperature ( $T$ ) dependences of  $S_{\text{Leads}}$  is presented in Fig.2.12 (solid blue circles). Back ground signal from the wires was small and linearly increases above  $T \sim 60\text{K}$ . For higher temperature, above  $T > T_c$  the signal was linearly extrapolated to the room temperature. Than we can subtract this from the raw data to get actual  $S$  of a sample. Otherwise you will have a mixture of a sample and wires signals together.

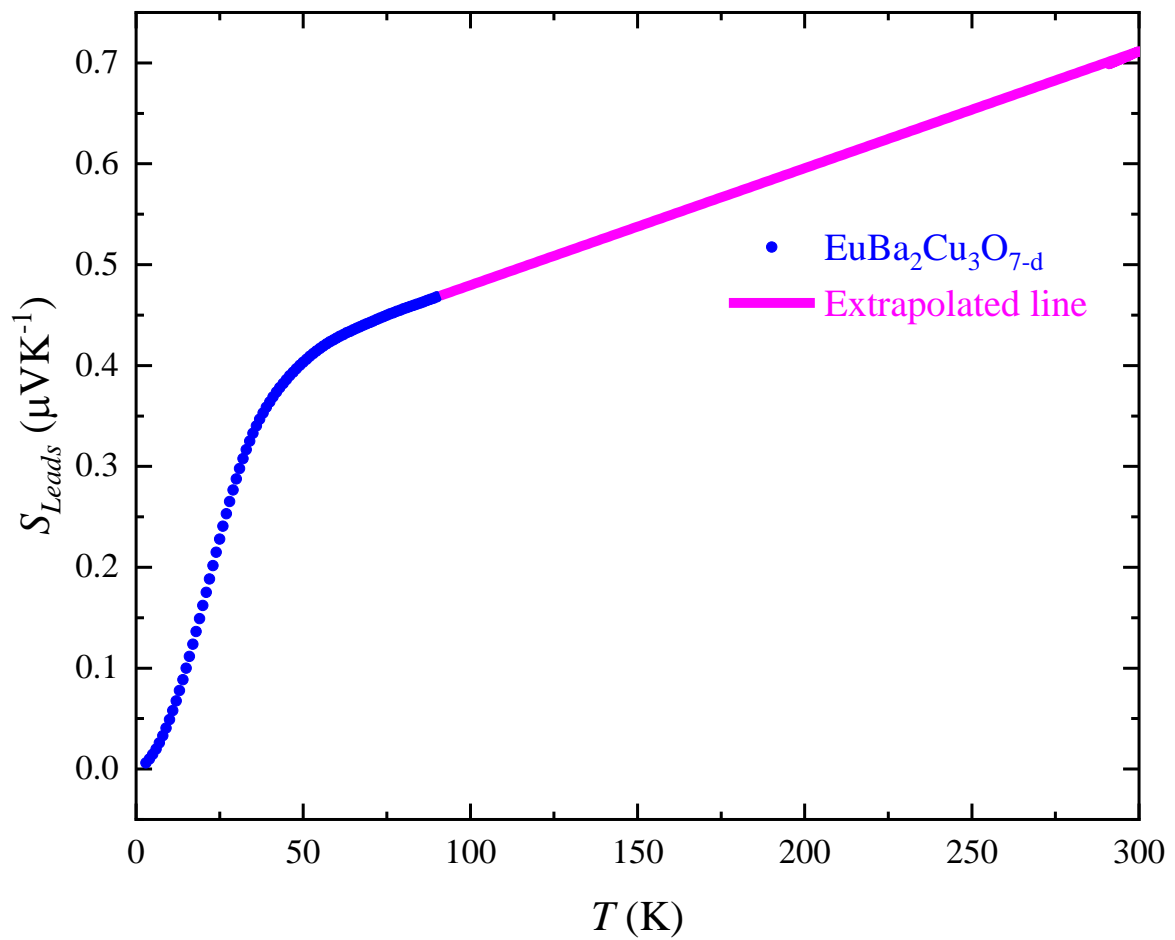


**Figure 2.12.** Temperature dependences of thermoelectric power of Leads of TEP.

## ARTICLES COMPRISING THE THESIS

### 3.1 A brief summary of the main results

In this PhD thesis, my aim was to explore the attributes of topological semimetals by studying their electrical and thermoelectric properties. This choice is motivated by the fact that the non-trivial electron structure is readily manifested by unconventional transport effects. In particular, thermoelectric coefficients show a profound response, providing a valuable source of information about an electronic system.

In the first project, we have studied the magnetoelectrical and magnetothermoelectrical transport properties of the topological semimetal TaAs<sub>2</sub>. This work involved the analysis of the prominent quantum oscillations observed at low temperatures in the resistivity as well as Hall, Seebeck, and Nernst coefficients. We noticed that of the amplitude the fundamental frequency shows an unusual temperature evolution when compared to its second harmonic. The effect of suppressing the fundamental oscillation while enhancing its second harmonic has turned out to be a consequence of Zeeman splitting and is referred to as the spin-zero effect. Such a phenomenon was previously reported to be caused by changes in the angle at which the magnetic field was applied. However, in our study, we reported the spin-zero effect in TaAs<sub>2</sub> to be induced by temperature changes, most likely the temperature evolution of the Landé  $g$ -factor. We concluded that the temperature evolution of the Landé  $g$ -factor can reflect changes in the spin-orbit coupling and be related to changes of the topological properties of TaAs<sub>2</sub>.

In the second project, we have reported anomalous Hall and anomalous Nernst effects arising from the k-space topology of the magnetic Weyl semimetal CeAlSi. In this work, we observed that at low temperature the sign of the anomalous Hall conductivity is positive for the out-of-plane oriented magnetic field and negative for the in-plane magnetic field. Based on the theoretical calculations, we showed that the sign change of the AHC originates from the reconstruction of the band structure under the variation of the spin orientation. To describe properties of the paramagnetic phase, we proposed a single-band toy model assuming a finite Berry curvature around Weyl nodes. This simple model recreates the experimental temperature evolution of AHE and ANE and suggests that the presence of Weyl points near the Fermi level plays a key role in determining the anomalous properties of CeAlSi.

In the third project, we conducted in-field electric and thermoelectric transport measurements in a thin film of the topological Dirac semimetal  $\alpha$ -Sn. When the magnetic field was applied along the electrical current or thermal gradient, we observed the negative longitudinal magnetoresistance and negative slope in the magnetic field dependence of the thermopower. This characteristic features of resistivity and thermopower vanish when the magnetic field is deviated from an orientation parallel to the electrical field or the thermal gradient. We showed that the appearances of NLMR and negative slope of the thermopower stems from the charge pumping between Weyl nodes of different chirality. This process diminishes at high temperature as a result of the reduction in the ratio of intervalley scattering time to Drude scattering time.

### **3.1.1 ARTICLE I: Quantum oscillations**

To study the quantum oscillations, we have selected a single crystal of TaAs<sub>2</sub>, which belongs to the MPn<sub>2</sub> class, where M represents the transition metal and Pn stands for the pnictide. The electronic structure of the MnP<sub>2</sub> family has recently been comprehensively

investigated and shown to consist of a number of trivial pockets together with those described by non-trivial weak topological indices [103,104]. Among the  $\text{MnP}_2$  compounds,  $\text{TaAs}_2$ , which crystallizes in a centrosymmetric monoclinic structure, has attracted considerable attention. This could be induced by observed at low temperatures unusual transport properties, such as ultra-high mobility and extremely large magnetoresistance (XMR) [105]. Furthermore, it was postulated that application of a magnetic field induces Weyl points in  $\text{TaAs}_2$  [94]. The associated Zeeman effect can also generate a non-zero Berry curvature, which will translate into an additional phase of the electron wave functions. This, in turn, can alter the conditions necessary for occurrence of the destructive interference of quantum oscillations, which is referred to as the spin-zero effect [95]. We have observed this phenomenon in measurements of the electrical and thermo-electrical transport properties of  $\text{TaAs}_2$  single crystal with applied magnetic field along  $[-210]$  crystallographic direction. In the Nernst signal, we detected two fundamental frequencies  $f_{\nu\alpha} \sim 105$  T and  $f_{\nu\beta} \sim 221$  T and a second harmonic of  $f_{\nu\beta}$ . Analogous to the Nernst oscillations, the fast Fourier transform of Shubnikov–de Haas oscillations also gave us two fundamental frequencies  $f_{\rho\alpha} \sim 122$  T and  $f_{\rho\beta} \sim 210$  T as well as a second harmonic  $2f_{\rho\beta} \sim 420$  of the latter. Although, the signal to noise ratio was higher for the former. Remarkably, the amplitude ratio of the fundamental  $\beta$  frequency and its second harmonic evolves in unusual way with temperatures, indicating the spin-zero effect at  $T \approx 25$  K. In addition, we observed that the phase of Nernst oscillations at  $T = 35$  K is opposite to one detected at  $T = 11.2$  K, which provides additional compelling evidence that the phenomenon is indeed caused by temperature changes rather than the angle at which the magnetic field was applied. A plausible source of the spin-zero effect in  $\text{TaAs}_2$  is the Lande' g-factor showing significant temperature dependence. Further, a possible reason for the temperature dependent Lande' g-factor is the evolution of the spin-orbit coupling, which can influence the topological properties of  $\text{TaAs}_2$ .

## Supplementary material: Temperature driven spin-zero effect in TaAs<sub>2</sub>

Md Shahin Alam<sup>1</sup>, P.K. Tanwar<sup>1</sup>, Krzysztof Dybko<sup>1,2</sup>, Ashutosh S. Wadge<sup>1</sup>, Przemysław Iwanowski<sup>1,2</sup>, Andrzej Wiśniewski<sup>1,2</sup> and Marcin Matusiak<sup>1,3,\*</sup>

1. *International Research Centre MagTop, Institute of Physics, Polish Academy of Sciences, Aleja Lotników 32/46, PL-02668 Warsaw, Poland*

2. *Institute of Physics, Polish Academy of Sciences, Aleja Lotników 32/46, PL-02668 Warsaw, Poland*

3. *Institute of Low Temperature and Structure Research, Polish Academy of Sciences, ul. Okólna 2, 50-422 Wrocław, Poland*

### A: Nernst signal oscillations in TaAs<sub>2</sub> and corresponding fast Fourier transform spectra

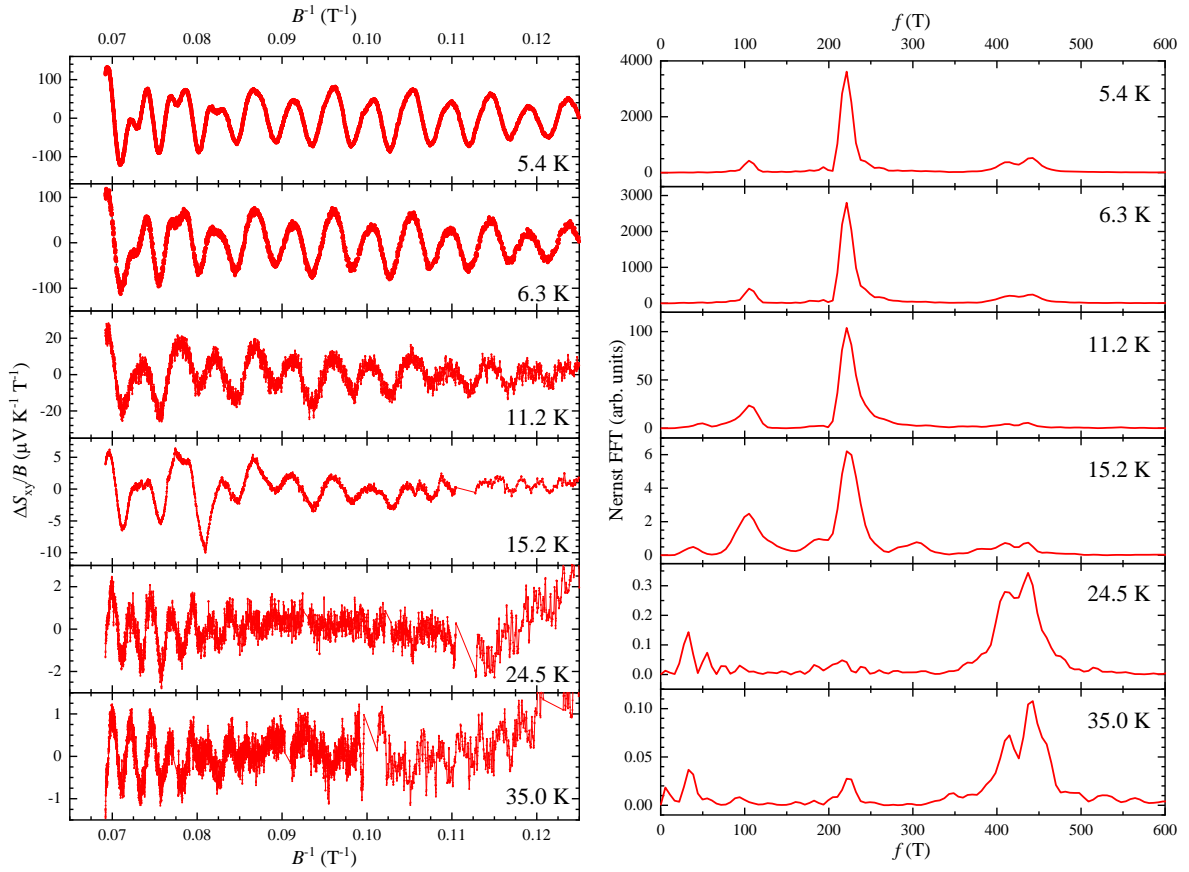


**Figure S1.** The oscillatory component of the Nernst coefficient in TaAs<sub>2</sub> plotted versus inverse magnetic field for various temperatures (left panel). The right panel presents respective FFT spectra.

**Table S1.** Parameters obtained from Lorentzian multiple peak fitting of the Nernst FFT spectra for  $\beta$  and  $2\beta$  oscillations.

<b><math>T</math> (K)</b>	<b>1<sup>st</sup> harmonic amplitude (arb. units)</b>	<b>2<sup>nd</sup> harmonic amplitude (arb. units)</b>	<b><math>A_1/A_2</math></b>	<b>1<sup>st</sup> harmonic Frequency (T)</b>	<b>2<sup>nd</sup> harmonic Frequency (T)</b>
5.4	3.81E-16	4.94E-17	7.7	220	441
6.3	2.94E-16	2.05E-17	14	221	441
11.2	1.05E-17	3.85E-19	27	223	421
15.2	6.20E-19	5.69E-20	11	224	436
24.5	3.81E-21	2.98E-20	0.13	211	437
35.0	2.77E-21	9.89E-21	0.28	223	443

**B: Temperature evolution of the  $\beta$  and  $2\beta$  oscillations amplitudes**

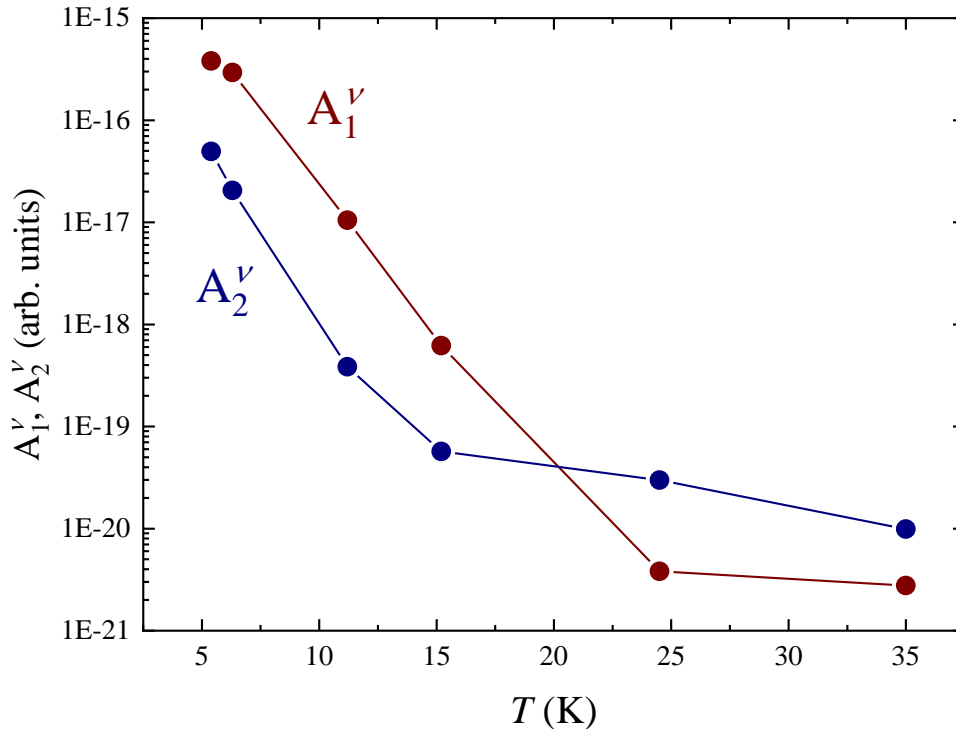


**Figure S2.** Calculated from the Nernst signal temperature dependence of the first ( $A_1^v$ ) and second ( $A_2^v$ ) harmonic amplitudes for the  $\beta$  band.

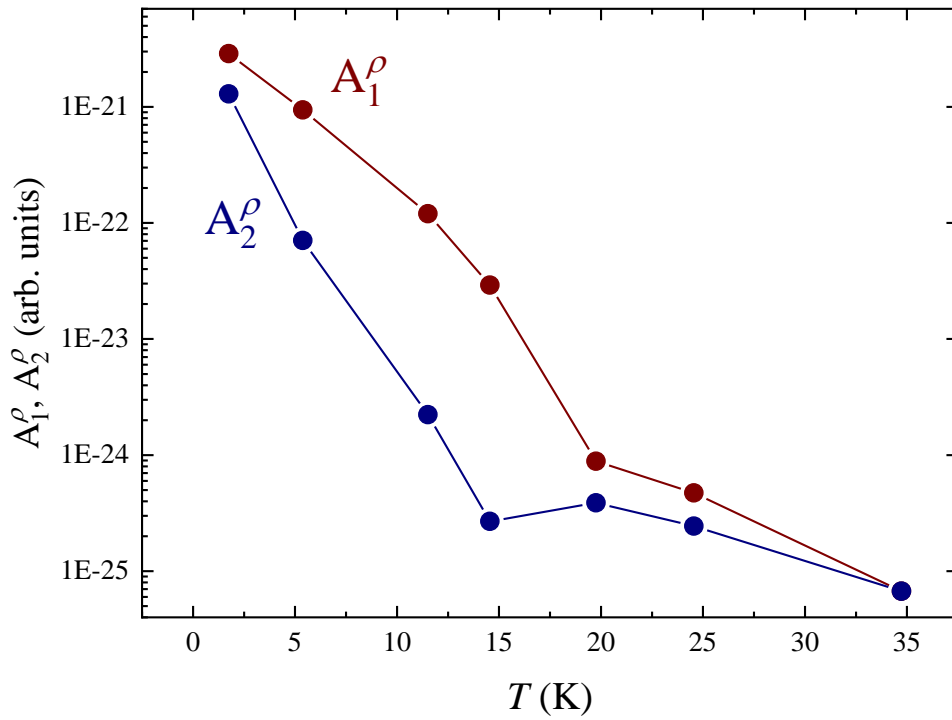


**Figure S3.** Calculated from the resistivity data temperature dependence of the first ( $A_1^\rho$ ) and second ( $A_2^\rho$ ) harmonic amplitudes for the  $\beta$  band.

## B: Filtered Nernst signal

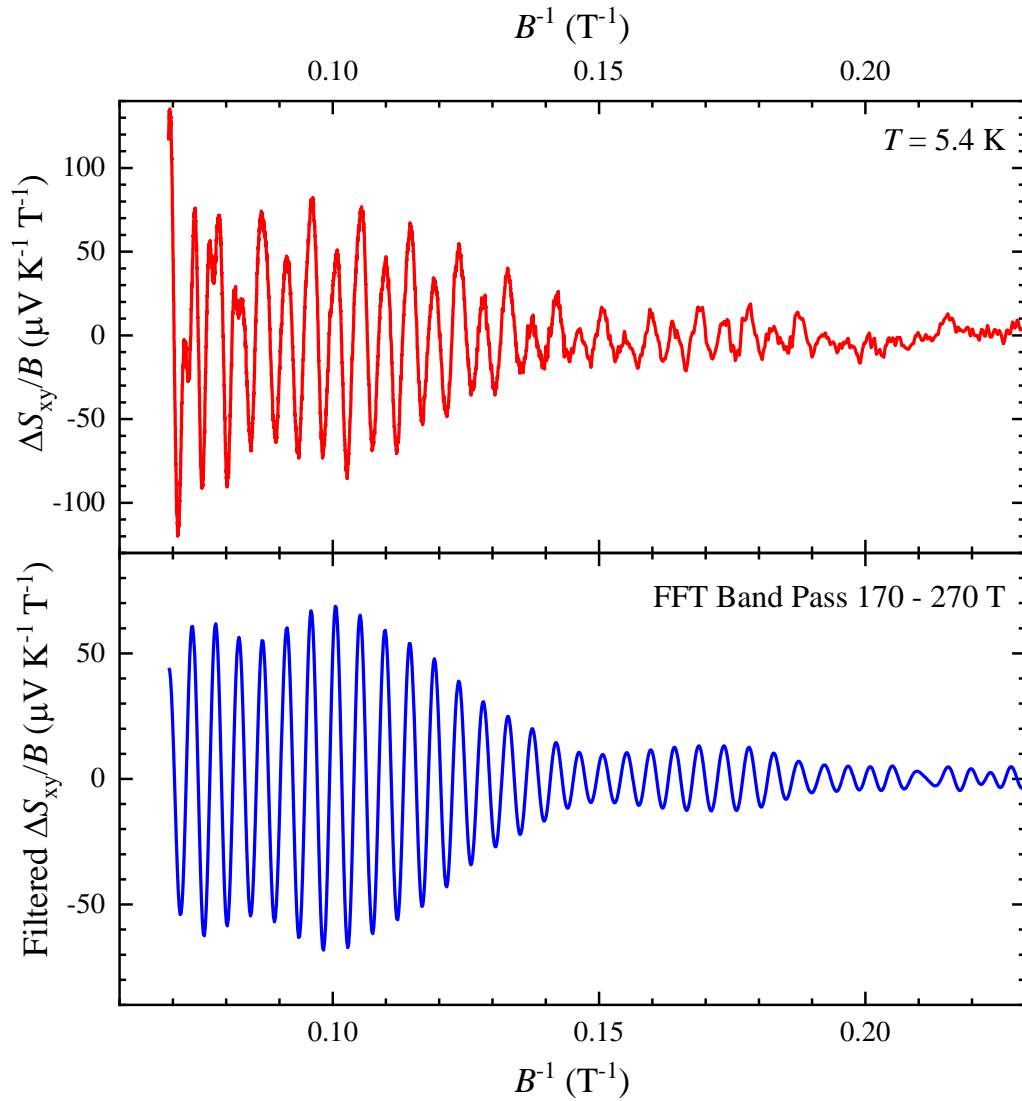


**Figure S4.** Upper panel: oscillatory Nernst signal in TaAs<sub>2</sub> measured at the temperature  $T = 5.4$  K plotted versus inverse magnetic field. Lower panel: signal from the upper panel filtered with the FFT band pass filter for the 170 - 270 T frequency range ( $\beta$  oscillations).

### C: Effective mass calculation

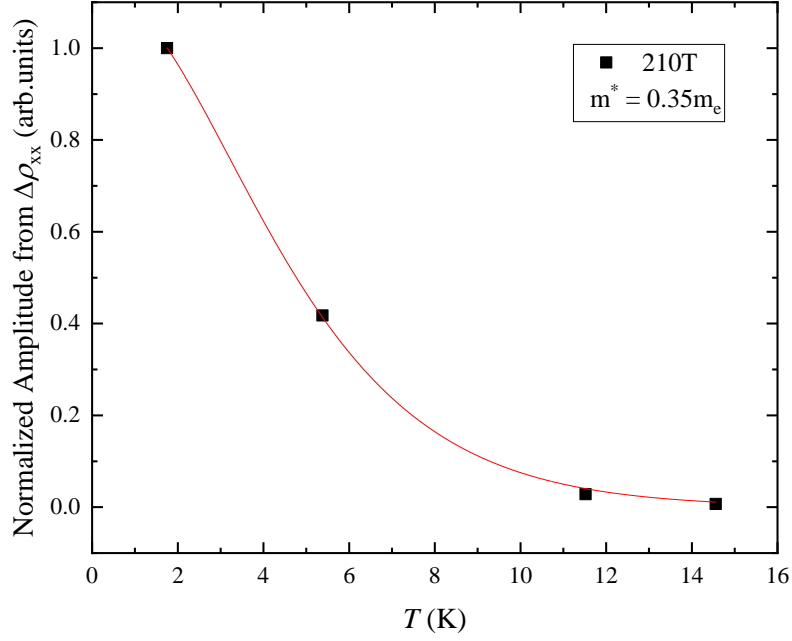


**Figure S5.** Temperature dependence of normalized FFT amplitude of the resistivity oscillations ( $8 \text{ T} < B < 14.5 \text{ T}$ ) for the  $\beta$  frequency in TaAs<sub>2</sub>. Solid line is fit of the Lifshitz-Kosevich formula.

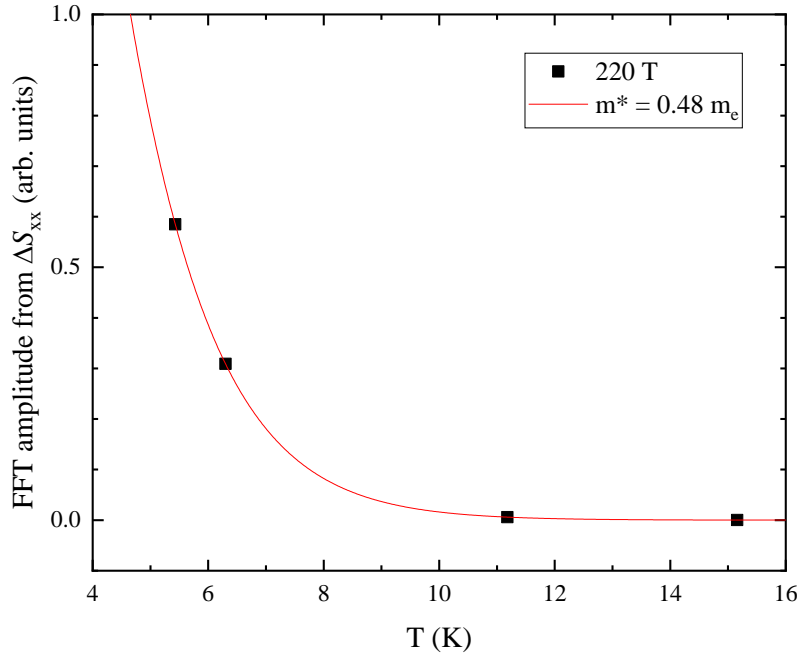


**Figure S6.** Temperature dependence of normalized FFT amplitude of the thermopower oscillations for the  $\beta$  frequency in TaAs<sub>2</sub>,  $5 \text{ T} < B < 14.5 \text{ T}$ . Solid line is fit of the modified Lifshitz-Kosevich formula [A.P. Morales et al., Phys. Rev. B **93**, 155120 (2016)]:  $A(T) \propto \frac{(\alpha p X) \coth(\alpha p X) - 1}{\sinh(\alpha p X)}$ , where  $\alpha = 2\pi^2 k_B / e\hbar$ ,  $k_B$  is the Boltzmann constant,  $e$  is the elementary charge,  $\hbar$  is the reduced Planck constant,  $p$  is the harmonic number, and  $X = m^* T / B$ .

### D: Amplitude ratio

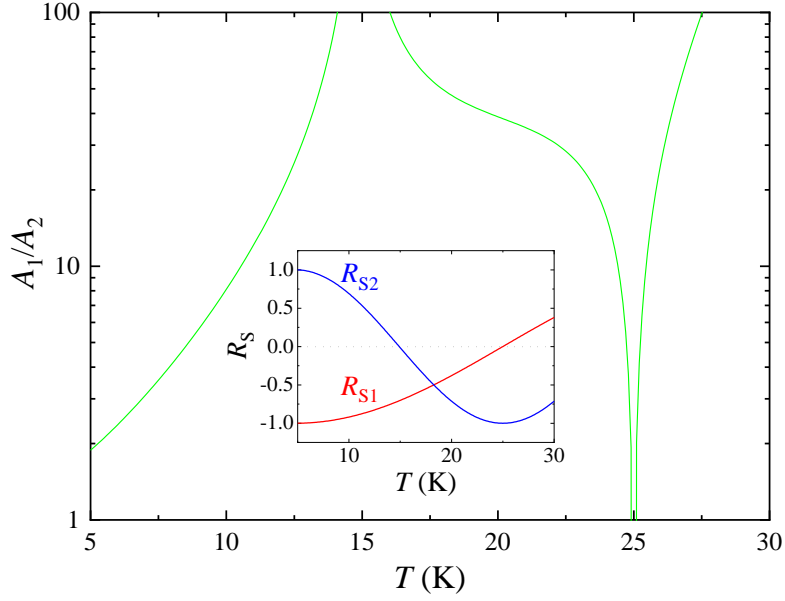


**Figure S7.** Temperature dependence of the absolute value of the first to second harmonic ratio calculated from the Lifshitz-Kosevich formula. The Dingle damping factor was assumed to be  $R_D = 1$ , the effective mass  $m^* = 0.18 m_0$ , and the Landé g-factor linearly increasing with temperature to reach the spin zero condition at  $T = 25$  K. Inset presents the temperature dependences of the spin damping factors for the fundamental frequency and its second harmonic. The latter goes through zero at  $T \approx 15$  K which causes the second harmonic to disappear at this temperature. The resulting  $A_1/A_2(T)$  qualitatively matches the experimental results, namely it initially (up to  $T \approx 15$  K) increases, then decreases and goes through zero at  $T = 25$  K and then increases again.

### E: Sample

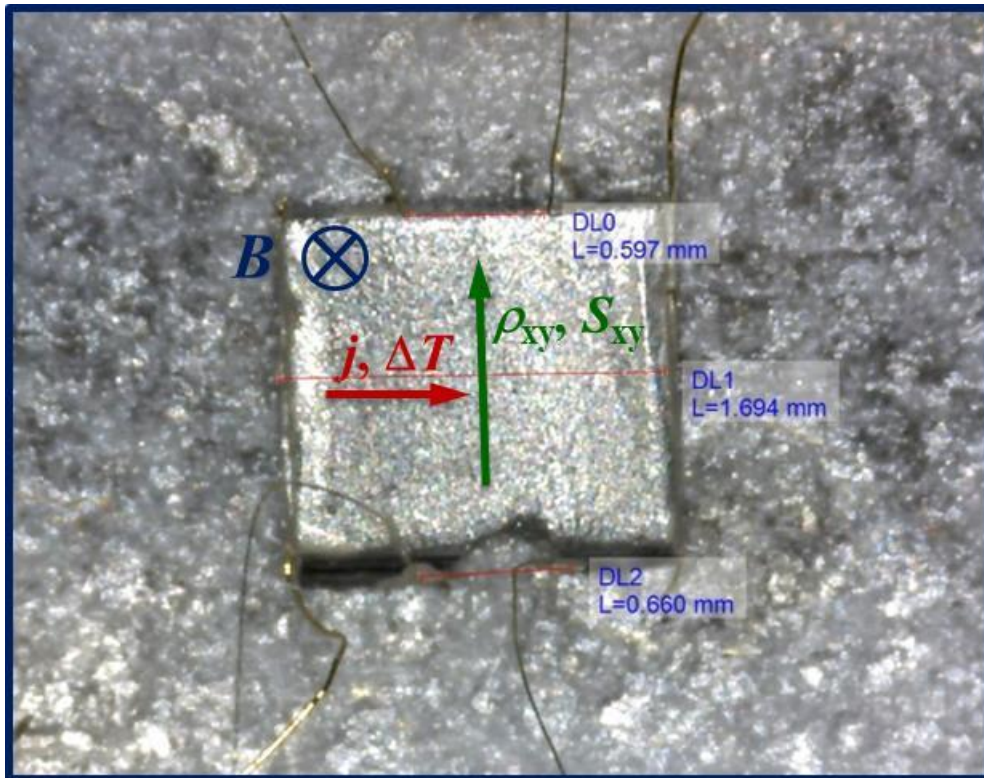


**Figure S8.** Single crystal of TaAs<sub>2</sub> with schematically shown experimental configuration.

### 3.1.2 ARTICLE II: Anomalous Hall and anomalous Nernst effect

The non-trivial topology of the electronic structure with Weyl nodes (WNs) near the Fermi level manifests itself in interesting phenomena such as the anomalous Hall and the anomalous Nernst effect. Generally, the creation of WNs requires breaking the time reversal symmetry or the inversion symmetry. Recently, it has been reported that in the case of RAISi semimetals (R stands for rare earth element) Weyl points can be generated by SI breaking, whereas TRS breaking shifts the position of WNs in the k-space [46,96,106,107]. An example is the ferromagnetic Weyl semimetal CeAlSi, which makes it an unique platform for studying the interplay between magnetism and topology. In this study, we reported the sign reversal of anomalous Hall conductivity in the ferromagnetic phase of CeAlSi for two different orientations of magnetic field, namely AHC is negative ( $\sigma_{yz}^A < 0$ ) for  $B \parallel a$ , and positive ( $\sigma_{xy}^A > 0$ ) for  $B \parallel c$ , where  $a$  and  $c$  denote the crystallographic axes. We indicated that the sign change of AHC in CeAlSi originates from the band structure reconstruction driven by the spin reorientation. The anomalous contribution has also been visible in the thermoelectric Nernst conductivity ( $\alpha_{xy}^A$ ) measured for  $B \parallel c$ . Furthermore, we observed persistence of anomalous Hall and Nernst signals even in the paramagnetic phase. To explain the temperature dependences of  $\sigma_{xy}^A$  and  $\alpha_{xy}^A/T$  above the Curie temperature, we proposed a single band toy-model, which includes a finite Berry curvature in the vicinity of Weyl nodes. The temperature dependences of  $\sigma_{xy}^A$  and  $\alpha_{xy}^A/T$  calculated using this simplistic approach correspond well to the experimental ones. This indicate that origin of high temperature large  $\sigma_{xy}^A$  and non-vanishing  $\alpha_{xy}^A$  lies in the CeAlSi topology.

Supplemental material:

**Sign change of the anomalous Hall effect and the anomalous Nernst effect  
in Weyl semimetal CeAlSi**

Md Shahin Alam <sup>1,\*</sup>, Amar Fakhredine <sup>2</sup>, Mujeeb Ahmed <sup>1</sup>, P.K. Tanwar <sup>1</sup>, Hung-Yu Yang <sup>3</sup>,  
Fazel Tafti <sup>3</sup>, Giuseppe Cuono <sup>1</sup>, Rajibul Islam <sup>1</sup>, Bahadur Singh <sup>4</sup>, Artem Lynnyk <sup>2</sup>, Carmine  
Autieri <sup>1,†</sup>, Marcin Matusiak <sup>1,5,‡</sup>

1. *International Research Centre MagTop, Institute of Physics, Polish Academy of Sciences, Aleja Lotników 32/46, PL-02668 Warsaw, Poland*
2. *Institute of Physics, Polish Academy of Sciences, Aleja Lotników 32/46, PL-02668 Warsaw, Poland*
3. *Department of Physics, Boston College, Chestnut Hill, Massachusetts 02467, USA*
4. *Department of Condensed Matter Physics and Materials Science, Tata Institute of Fundamental Research, Mumbai 400005, India*
5. *Institute of Low Temperature and Structure Research, Polish Academy of Sciences, ul. Okólna 2, 50-422 Wrocław, Poland*

## A: Non-anomalous fits of the magnetic field dependences

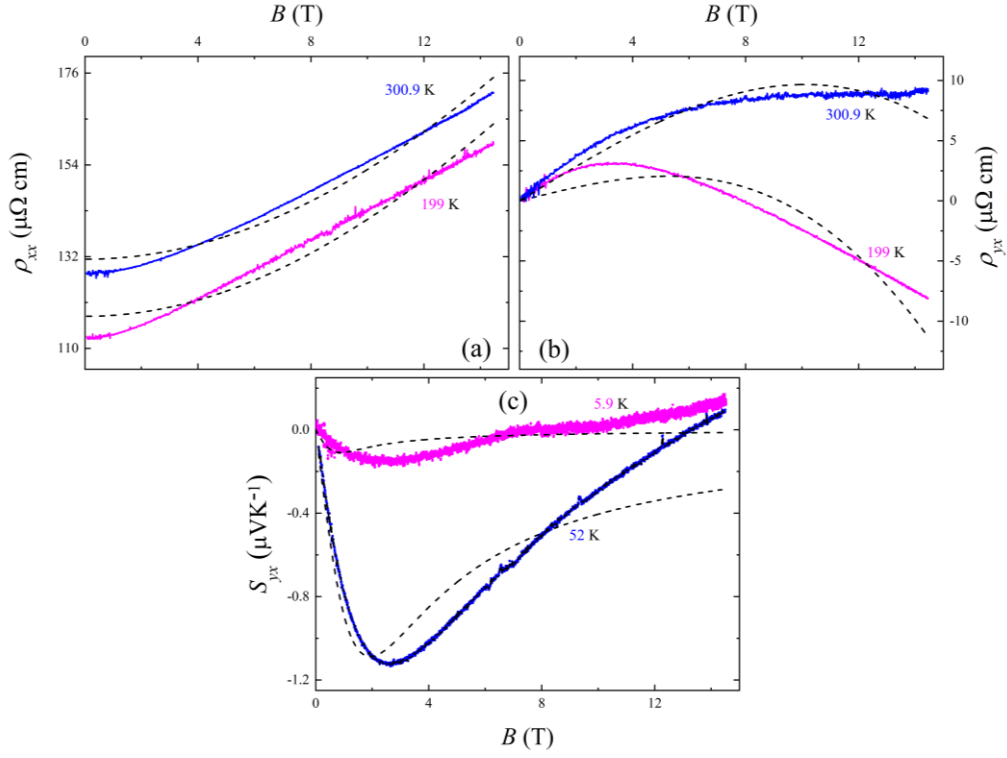


**Figure S1.** (a & b) Magnetic field dependences of the longitudinal resistivity ( $\rho_{xx}$ ) and Hall resistivity ( $\rho_{yx}$ ) for  $T = 199$  K (magenta) and 300.9 K (blue) for CeAlSi. The black dashed lines indicate the best simultaneous fits using the semi-classical two band approximation [1]. There is an apparent discrepancy between the experimental data and the model. (c) Nernst signal ( $S_{yx}$ ) as a function of  $B$ . Black dashed lines represent fits to:  $S_{yx}^N = S_0^N \frac{\mu}{1+(\mu B)^2}$  (see main text), which poorly matches the experimental data.

## B: Scaling of anomalous Hall resistivity

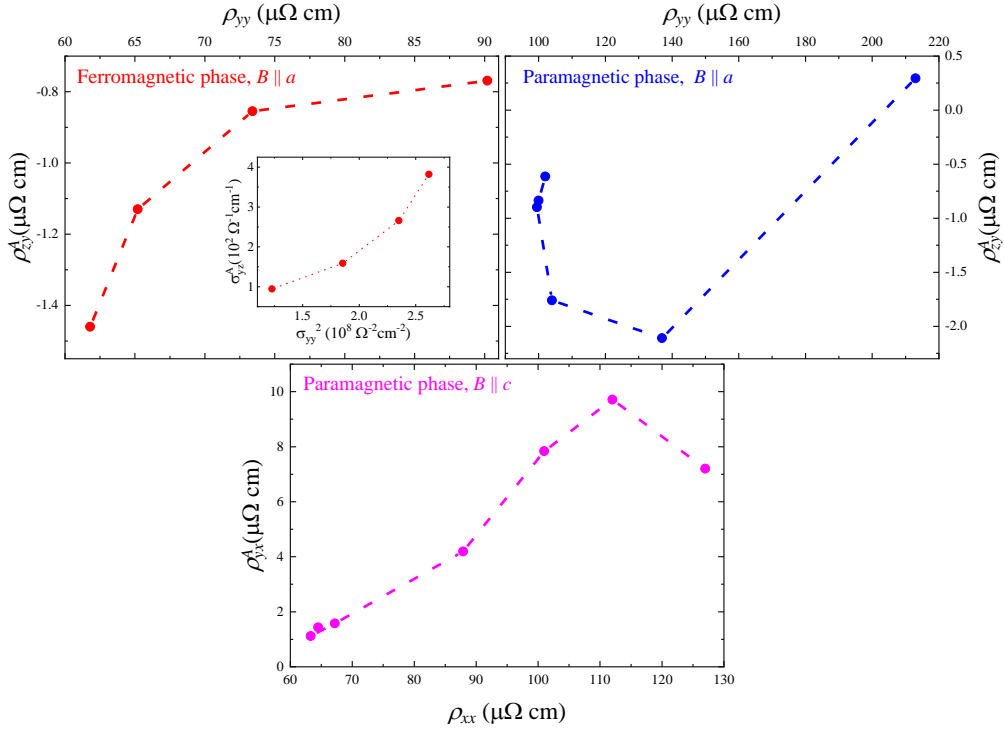


**Figure S2.** (a) The anomalous Hall resistivity ( $\rho_{zy}^A$ ) in ferromagnetic phase of CeAlSi plotted versus longitudinal resistivity ( $\rho_{yy}$ ) for  $B \parallel a$ . Inset shows the anomalous Hall conductivity ( $\sigma_{yz}^A$ ) as a function of the square of the longitudinal conductivity ( $\sigma_{yy}^2$ ) (b)  $\rho_{zy}^A$  vs  $\rho_{yy}$  for  $B \parallel a$  in paramagnetic phase. (c) The anomalous Hall resistivity ( $\rho_{yx}^A$ ) versus the longitudinal resistivity ( $\rho_{xx}$ ) for  $B \parallel c$ , in paramagnetic phase.

## C: Magnetic measurements

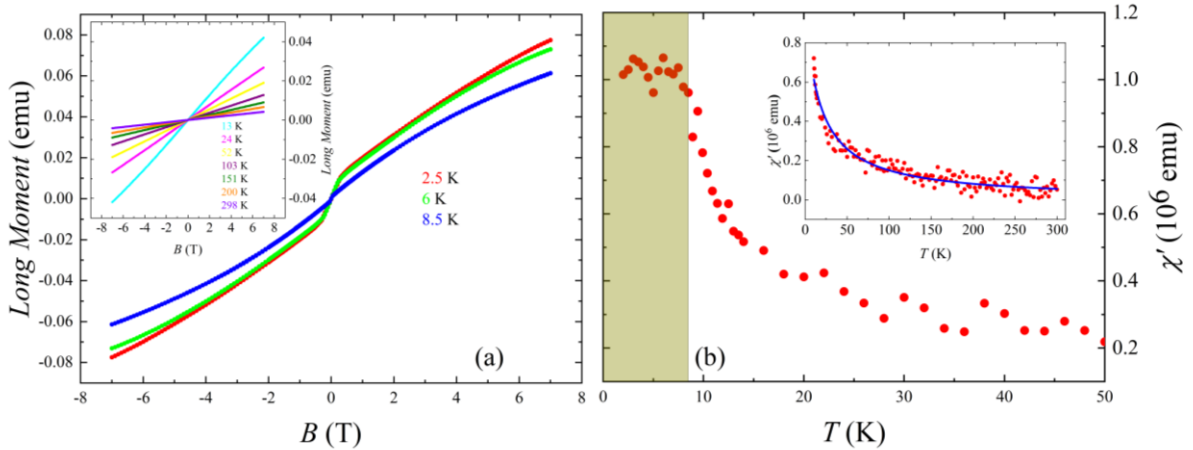


**Figure S3.** (a) Magnetic field dependences of the longitudinal magnetic moments in ferromagnetic phase of CeAlSi. Inset shows long magnetic moment as a function of  $B$  in the paramagnetic phase. (b) Temperature dependence of the magnetic susceptibility ( $\chi'$ ) with the ferromagnetic region marked in dark yellow. Inset shows  $\chi'$  vs  $T$  (red points) in the paramagnetic phase fitted to the Curie-Weiss law (solid blue line).

## D: Anomalous Hall and Nernst conductivities in presence of non-zero Berry curvature

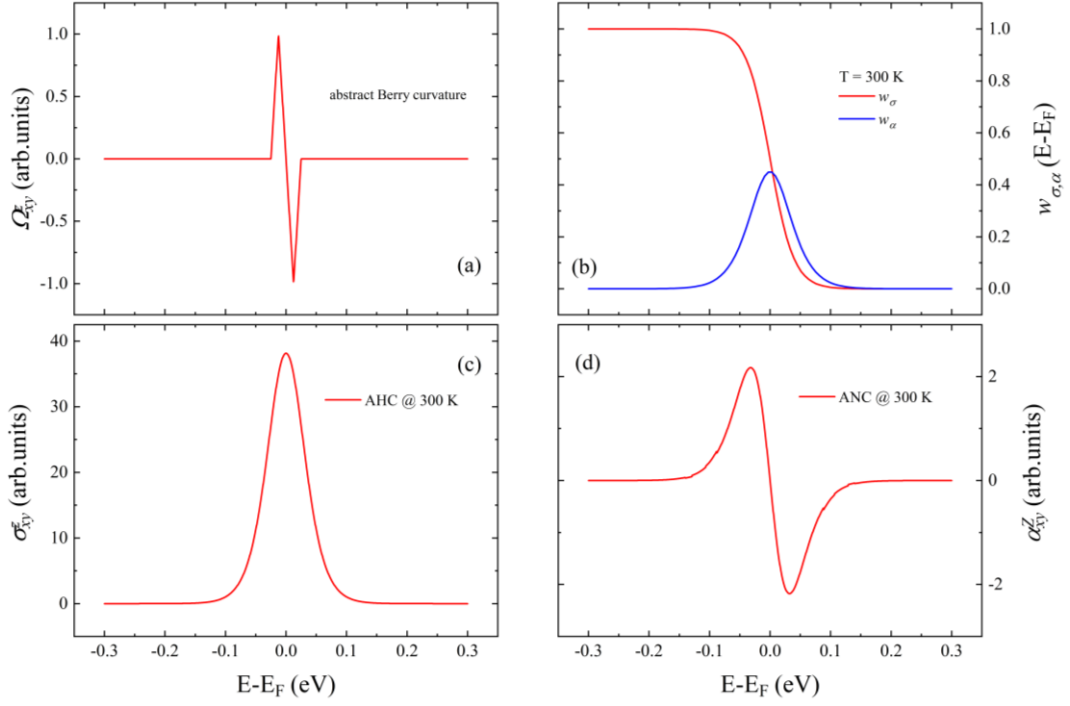


**Figure S4.** (a) Imaginary Berry curvature ( $\Omega_{xy}^Z$ ) in arbitrary units plotted versus energy near the Fermi level. (b) Weighting function ( $\omega$ ) for the anomalous Hall conductivity (red) and the transverse thermoelectrical conductivity (blue) as a function of energy at  $T = 300$  K. (c) Energy dependences of the anomalous Hall conductivity at  $T = 300$  K, calculated as a product of  $\Omega_{xy}^Z$  and weighting function  $w_\sigma$ . (d) Anomalous Nernst conductivity as a function of energy  $T = 300$  K calculated as a product of  $\Omega_{xy}^Z$  and weighting function  $w_\alpha$ .

## **E: Computational details for Density functional theory**

First-principles calculations were conducted and the projector-augmented-wave (PAW) method was applied. The generalized gradient approximation of the Perdew-Burke-Ernzerhof(PBE) form was used to treat the exchange-correlation energy (GGA), as implemented in the Vienna ab-initio simulation package (VASP) in the frame of the density functional theory [2,3]. The cut-off energies for the plane-wave basis set that were used to expand the Kohn-Sham orbitals were chosen to be 450 eV. All calculations include the spin-orbit coupling. The Monkhorst-Pack scheme was used for the  $\Gamma$ -centered  $10 \times 10 \times 10$  k-point sampling. The calculations are performed using the experimental lattice parameters of CeAlSi ( $a = 4.252 \text{ \AA}$ ;  $c = 14.5801 \text{ \AA}$ ) [4]. In order to conduct the effect of strongly correlated electrons in the 4f-shell of Ce, we applied the GGA+U method within the self-consistent DFT cycle [5]. The on-site Coulomb interaction strength  $U$  applied to the Ce 4f states is 7 eV and the intra-atomic exchange interaction strength  $J_H$  was taken as zero. Our ab-initio results were utilized to obtain the Wannier tight-binding Hamiltonian using the VASP2WANNIER90 interface [6]. The Anomalous Hall Effect was calculated subsequently after applying the technique of Wannier interpolation [7] using a k-grid of  $100 \times 100 \times 100$  with an adaptive grid of  $5 \times 5 \times 5$ . The AHE calculations were verified with a k-grid of  $300 \times 300 \times 300$  that reproduce the same results with negligible differences. The calculations were performed on three different spin configurations of the CeAlSi unit cell; a collinear FM phase with the spins aligned along the x-axis direction, a collinear FM phase with the spins aligned along the z-axis direction, and a non-collinear FM ordering. All the AHE calculations reproduce a minimum and a maximum close to the Fermi level, therefore the AHE results are robust respect to the wannierization of the three different magnetic configurations.

For better analysis of the electronic structure of CeAlSi, the atom-resolved local density of states (LDOS) was also calculated for the non-collinear ferromagnetic

configuration with spin-orbit coupling (SOC) and presented in Figure 8. DOS for other magnetic configurations are qualitatively similar. The sp-bands of Al and Si are present both below and above the Fermi level. One band of the Ce 4f-states is present at -3 eV from the Fermi level, while the other Ce 4f-states are above 2 eV from the Fermi level. The sp-orbitals of Ce are less relevant, while close to the Fermi level, the only relevant contribution from the Ce atoms comes from the 5d-states.

The oxidation states of atoms is zero in this compound. The electronic configuration for Ce reported in textbooks is  $[\text{Xe}]4f^15d^16s^2$  in the ionic approximation, this electronic configuration can change depending on the structural phases and crystal fields. In CeAlSi, the electronic configuration changes to be something more similar to  $4f^15d^36s^0$  in the ionic approximation according to our local DOS. Indeed, due to the crystal field effect of the surrounding atoms that act differently on d-electrons and on s-electrons, the s-electrons of Ce are pushed to higher energies. Since we are only interested in the electronic properties at the Fermi level, we have approximated the Ce atom as  $[\text{Xe}]4f^15d^36s^0$  considering that only the 5d electrons are relevant for the wannierization and excluding the 4f electrons from our tight-binding model. For this reason, the wannierization was performed taking into consideration the sp-electrons of Al, sp-electrons of Si and the d-electrons of Ce as tight-binding basis. Within its simplicity, this approximation brings us to a quite good result of the wannierization. We have chosen the frozen window around the Fermi level excluding the 4f states in both conduction and valence band. Our wannierization is in agreement with that reported in the literature [8].

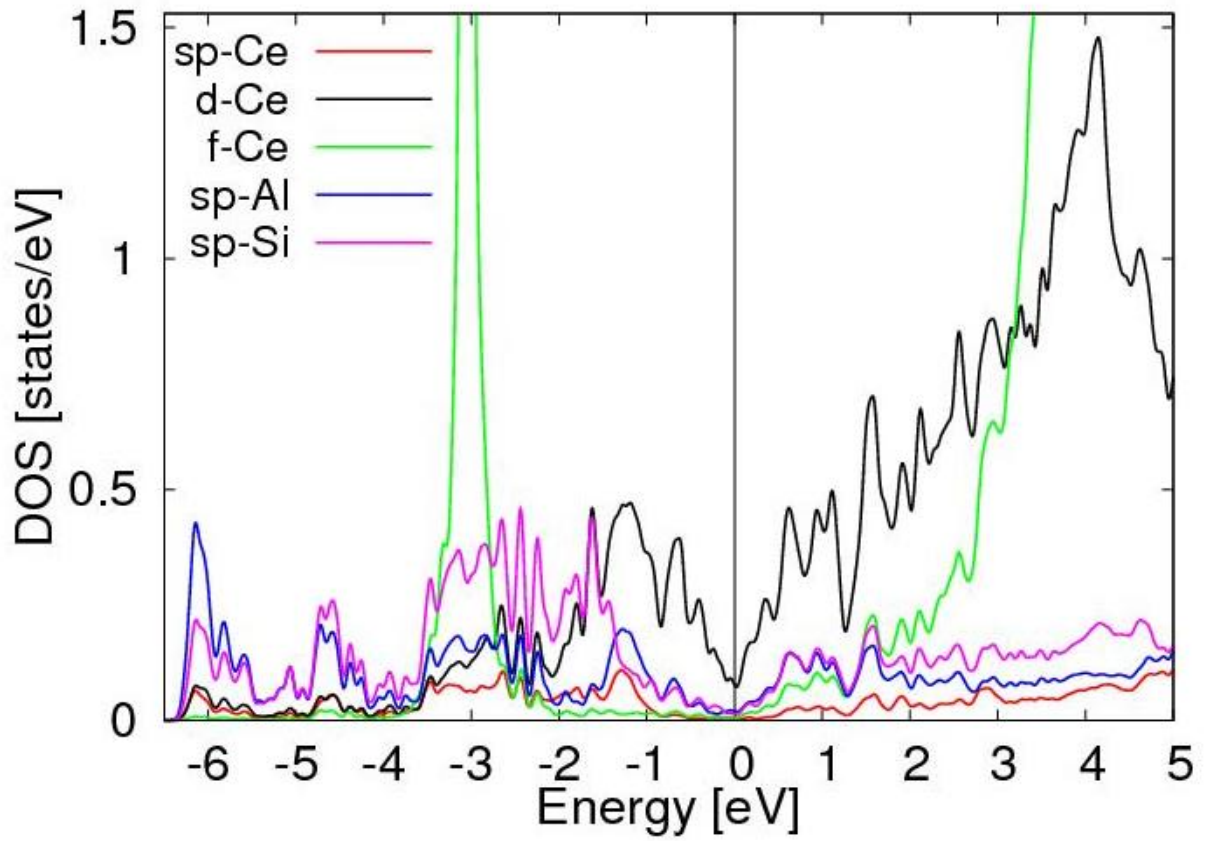


**Figure S5.** Local density of states for the non-collinear magnetic configuration of CeAlSi.

The 4f-levels of Ce are extremely localized and their DOS goes beyond the maximum of the y-range. The Fermi level is set to zero.

## References

- [1] C. M. Hurd, *The Hall Effect in Metals and Alloys, The International Cryogenics Monograph Series*, Springer, Berlin (1972). DOI: [https://doi.org/10.1007/978-1-4757-0465-5\\_8](https://doi.org/10.1007/978-1-4757-0465-5_8)
- [2] G. Kresse and J. Hafner, *Ab Initio Molecular Dynamics for Liquid Metals*, Phys. Rev. B **47**, 558 (1993). DOI: <https://doi.org/10.1103/PhysRevB.47.558>
- [3] G. Kresse and J. Furthmüller, *Efficient Iterative Schemes for Ab Initio Total-Energy Calculations Using a Plane-Wave Basis Set*, Phys. Rev. B - Condens. Matter Mater. Phys. **54**, 11169 (1996). DOI: <https://doi.org/10.1103/PhysRevB.54.11169>
- [4] H. Y. Yang, B. Singh, J. Gaudet, B. Lu, C. Y. Huang, W. C. Chiu, S. M. Huang, B. Wang, F. Bahrami, B. Xu, J. Franklin, I. Sochnikov, D. E. Graf, G. Xu, Y. Zhao, C. M. Hoffman, H. Lin, D. H. Torchinsky, C. L. Broholm, A. Bansil, and F. Tafti, *Noncollinear Ferromagnetic Weyl Semimetal with Anisotropic Anomalous Hall Effect*, Phys. Rev. B **103**, 115143 (2021). DOI: <https://doi.org/10.1103/PhysRevB.103.115143>
- [5] W. E. Pickett, *Implementation of the Lda+u Method Using the Full-Potential Linearized Augmented Plane-Wave Basis*, Phys. Rev. B - Condens. Matter Mater. Phys. **60**, 10763 (1999). DOI: <https://doi.org/10.1103/PhysRevB.60.10763>
- [6] A. A. Mostofi, J. R. Yates, G. Pizzi, Y. S. Lee, I. Souza, D. Vanderbilt, and N. Marzari, *An Updated Version of Wannier90: A Tool for Obtaining Maximally-Localised Wannier Functions*, Comput. Phys. Commun. **185**, 2309 (2014). DOI: <https://doi.org/10.1016/j.cpc.2007.11.016>
- [7] M. Zeer, D. Go, J. P. Carbone, T. G. Saunderson, M. Redies, M. Kläui, J. Ghabboun, W. Wulfhekel, S. Blügel, and Y. Mokrousov, *Spin and Orbital Transport in Rare-Earth Dichalcogenides: The Case of EuS<sub>2</sub>*, Phys. Rev. Mater. **6**, 074004 (2022). DOI: <https://doi.org/10.1103/PhysRevMaterials.6.074004>
- [8] M. M. Piva, J. C. Souza, V. Brousseau-Couture, K. R. Pakuszewski, J. K. John, C. Adriano, M. Côté, P. G. Pagliuso, and M. Nicklas, *Tuning the Nontrivial Topological Properties of the Weyl Semimetal CeAlSi*, ArXiv:2111.05742 1 (2021). DOI: <https://doi.org/10.48550/arXiv.2111.05742>

### 3.1.3 ARTICLE III: Chiral anomaly

The electronic structure of topological Dirac semimetals contains fourfold degenerate Dirac cones, which can be split into a pair of Weyl cones by breaking either the SI or the TRS. An exotic phenomenon known as chiral anomaly can occur in these materials when a parallel electric field or thermal gradient is applied along with the magnetic field [32,53]. This should manifest macroscopically as an additional electrical current but its detection by electrical measurements has been a cause for concern. This is due to possible contributions from extrinsic phenomena such as the current jetting effect [77]. On the contrary, thermoelectric measurements offer the possibility to study the aforementioned phenomena free from artefacts [53]. In this study, we have chosen a topological Dirac semimetal  $\alpha$ -Sn in a form of a strained thin film, whose electronic structure contains a pair of Dirac cones that are protected by fourfold rotational and time-reversal symmetries [28]. The latter can be broken by the application of a magnetic field, making  $\alpha$ -Sn a Weyl semimetal that is a suitable candidate for the observation of the aforementioned quantum anomaly. The expected consequences of its appearance include a negative magnetoresistance or a negative slope of the magneto-thermopower in the presence of a magnetic field parallel to the electric current or thermal gradient. Indeed, we have observed both characteristics in  $\alpha$ -Sn at low temperatures. The anomalous behavior is expected to disappear rapidly when the magnetic field is tilted away from the applied current or thermal gradient, and we have again confirmed this by angle dependent measurements. The calculated ratio of the intervalley relaxation time to the Drude scattering time indicates that  $\alpha$ -Sn at low temperature is in fact in the chiral regime.

- [64] R. Islam, B. Ghosh, G. Cuono, A. Lau, W. Brzezicki, A. Bansil, A. Agarwal, B. Singh, T. Dietl, and C. Autieri, *Topological States in Superlattices of HgTe Class of Materials for Engineering Three-Dimensional Flat Bands*, Phys. Rev. Res. **4**, 023114 (2022).
- [65] Z. Wang, H. Weng, Q. Wu, X. Dai, and Z. Fang, *Three-Dimensional Dirac Semimetal and Quantum Transport in Cd<sub>3</sub>As<sub>2</sub>*, Phys. Rev. B **88**, 125427 (2013).
- [66] C. Zhang, E. Zhang, W. Wang, Y. Liu, Z. G. Chen, S. Lu, S. Liang, J. Cao, X. Yuan, L. Tang, Q. Li, C. Zhou, T. Gu, Y. Wu, J. Zou, and F. Xiu, *Room-Temperature Chiral Charge Pumping in Dirac Semimetals*, Nat. Commun. **8**, 13741 (2017).
- [67] W. Zhang, P. Wang, G. Gu, X. Wu, and L. Zhang, *Negative Longitudinal Magnetothermopower in the Topological Semimetal ZrTe<sub>5</sub>*, Phys. Rev. B **102**, 115147 (2020).
- [68] Z. Jia, C. Li, X. Li, J. Shi, Z. Liao, D. Yu, and X. Wu, *Thermoelectric Signature of the Chiral Anomaly in Cd<sub>3</sub>As<sub>2</sub>*, Nat. Commun. **7**, 13013 (2016).
- [69] F. Caglieris, C. Wuttke, S. Sykora, V. Süß, C. Shekhar, C. Felser, B. Büchner, and C. Hess, *Anomalous Nernst Effect and Field-Induced Lifshitz Transition in the Weyl Semimetals TaP and TaAs*, Phys. Rev. B **98**, 201107(R) (2018).
- [70] B. Cheng, T. Schumann, S. Stemmer, and N. P. Armitage, *Probing Charge Pumping and Relaxation of the Chiral Anomaly in a Dirac Semimetal*, Sci. Adv. **7**, eabg0914 (2021).
- [71] C. L. Zhang, S. Y. Xu, I. Belopolski, Z. Yuan, Z. Lin, B. Tong, G. Bian, N. Alidoust, C. C. Lee, S. M. Huang, T. R. Chang, G. Chang, C. H. Hsu, H. T. Jeng, M. Neupane, D. S. Sanchez, H. Zheng, J. Wang, H. Lin, C. Zhang, H. Z. Lu, S. Q. Shen, T. Neupert, M. Z. Hasan, and S. Jia, *Signatures of the Adler-Bell-Jackiw Chiral Anomaly in a Weyl Fermion Semimetal*, Nat. Commun. **7**, 10735 (2016).
- [72] A. H. Wilson, *The theory of metals*, I. Proc. R. Soc. Lond. A **138**, 594 (1932).
- [73] T. H. Liu, J. Zhou, M. Li, Z. Ding, Q. Song, B. Liao, L. Fu, and G. Chen, *Electron Mean-Free-Path Filtering in Dirac Material for Improved Thermoelectric Performance*, Proc. Natl. Acad. Sci. U. S. A. **115**, 879 (2018).
- [74] J. Gooth, A. C. Niemann, T. Meng, A. G. Grushin, K. Landsteiner, B. Gotsmann, F. Menges, M. Schmidt, C. Shekhar, V. Süß, R. Hühne, B. Rellinghaus, C. Felser, B. Yan, and K. Nielsch, *Experimental Signatures of the Mixed Axial-Gravitational Anomaly in the Weyl Semimetal NbP*, Nature **547**, 324 (2017).

## Supplemental material:

### Quantum transport properties of the topological Dirac Semimetal $\alpha$ -Sn

Md Shahin Alam <sup>1,\*</sup>, Alexandr Kazakov <sup>1</sup>, Mujeeb Ahmad <sup>1</sup>, Rajibul Islam <sup>2</sup>, Fei Xue <sup>2</sup>, and Marcin

Matusiak <sup>1,3,†</sup>

1. International Research Centre MagTop, Institute of Physics, Polish Academy of Sciences, Aleja Lotników 32/46, PL-02668 Warsaw, Poland

2. Department of Physics, University of Alabama at Birmingham, Birmingham, Alabama 35294, USA

3. Institute of Low Temperature and Structure Research, Polish Academy of Sciences, ulica Okólna 2, 50-422 Wrocław, Poland

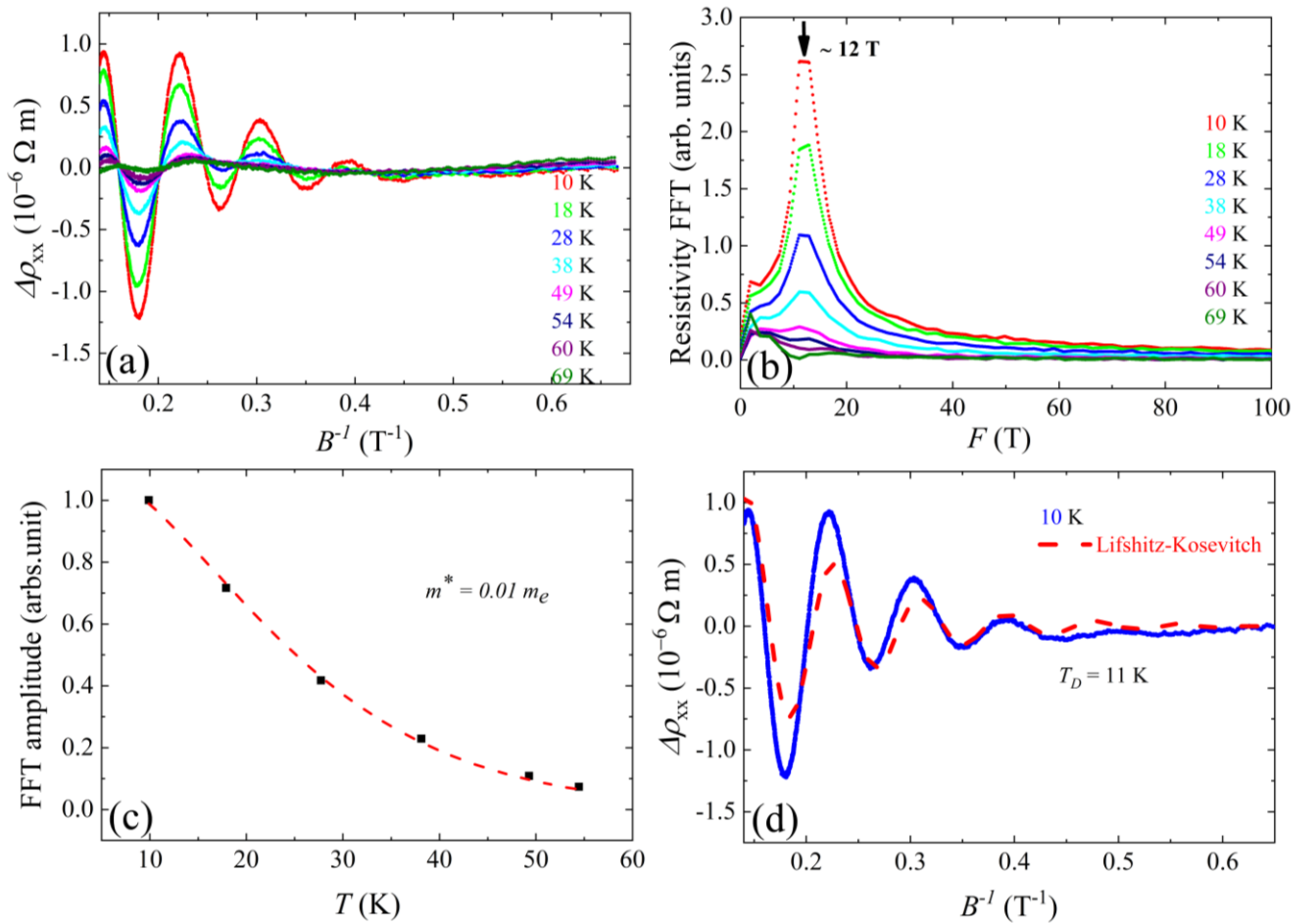


**Figure S1 .** (Color online) (a) Shubnikov de Hass oscillations after subtracting the smooth 3<sup>rd</sup> order polynomial background from  $\rho_{xx}(B)$  at different temperatures. (b) Fast Fourier transform spectrum of  $\alpha$ -Sn showing a single frequency at  $\sim 12 \text{ T}$ , calculated from SdH oscillations data, the effective field of oscillations taken between 1.5-8 T. (c) Amplitude of the FFT spectrum of the  $\sim 12 \text{ T}$  frequency plotted against temperatures. Red dashes lines

represent the fit to the thermal damping factor ( $R_T$ ) from the Lifshitz-Kosevich formula. (d) Shubnikov de Hass oscillations at 10 K temperature. Red dashes line presents the fit to the Lifshitz-Kosevich formula (see equation 1 in the main text).

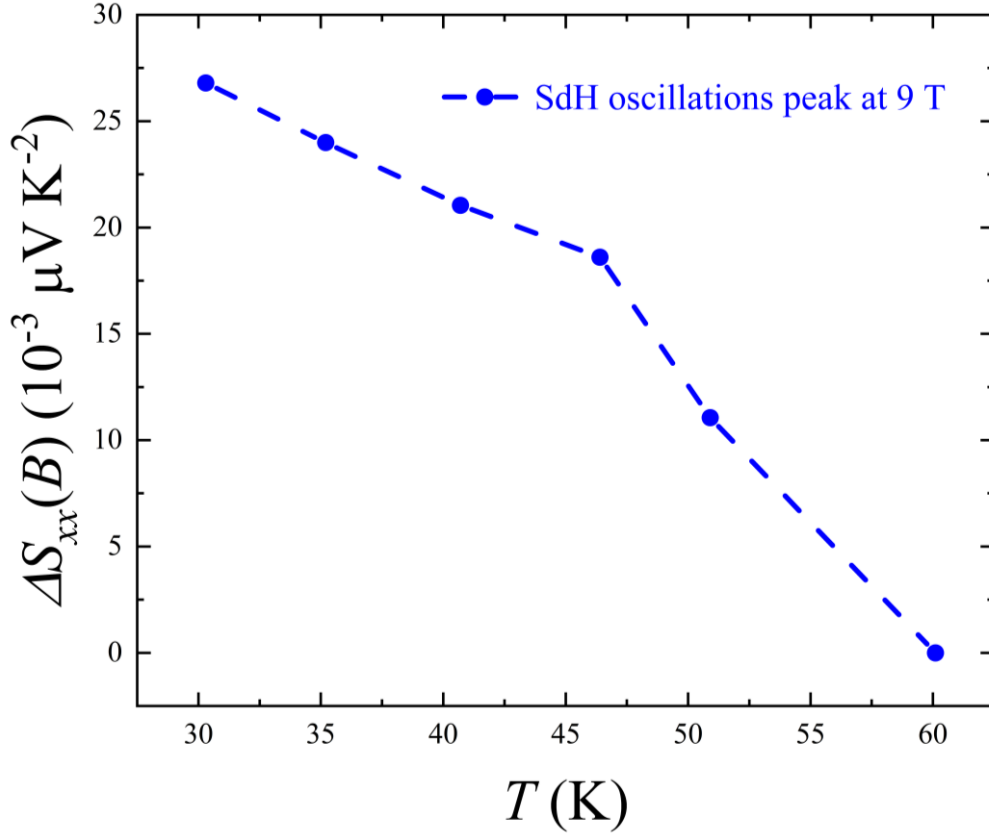


**Figure S2** . (Color online) Temperature dependence of the peak height of quantum oscillations of the thermopower ( $\Delta S/T$ ) at 9 T. The peak height at 8.8 T with respect to the peak height at 5.2 T from the baseline was calculated using the Dingle term ( $R_D$ ) from the Lifshitz-Kosevich formula. The  $T_D$  for the higher temperatures was estimated in a similar way as for the 10 K temperature (see main text).

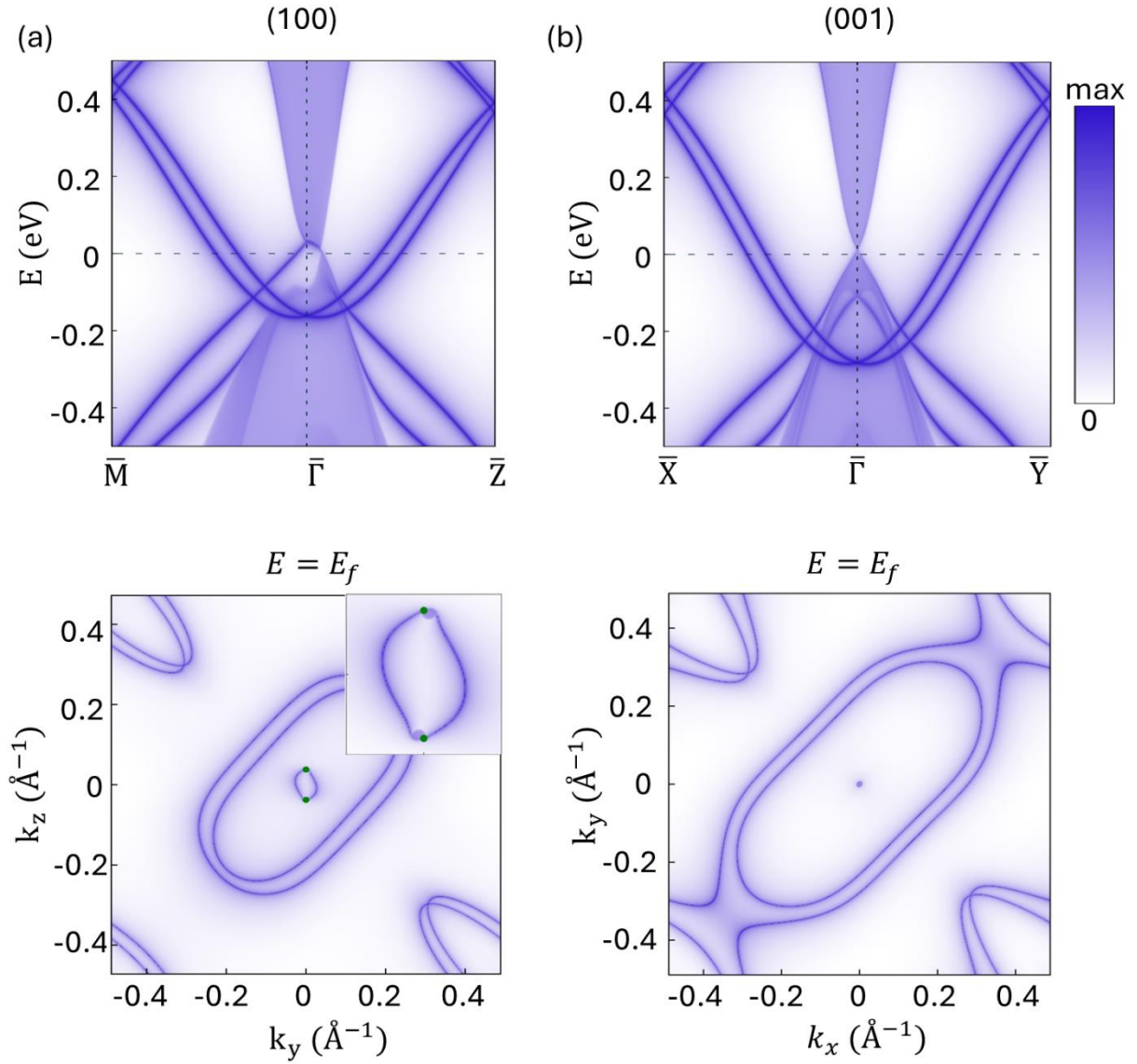


**Figure S3.** (Color online) The electronic band structure of the surface is projected on (a) (100) along  $\bar{M} \rightarrow \bar{\Gamma} \rightarrow \bar{Z}$  and (b) (001) along  $\bar{X} \rightarrow \bar{\Gamma} \rightarrow \bar{Y}$ . The isoenergetic Fermi-surface contour is displayed in the bottom panel, Dirac points are located with green circle.

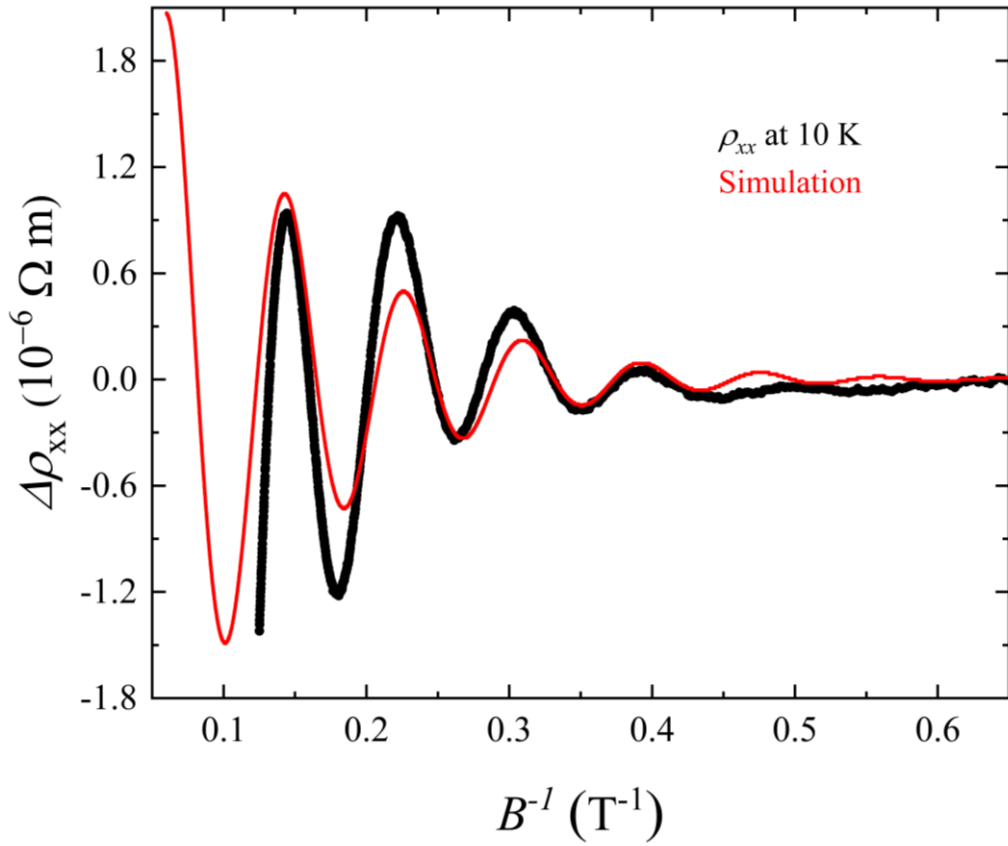


**Figure S4** . (Color online) (a) Quantum oscillations after subtracting the smooth 3<sup>rd</sup> order polynomial background in the field range of 1.5 to 8 T from  $\rho_{xx}(B)$  at 10 K temperature. Solid Red line presents the simulation of  $\Delta\rho_{xx}$  vs  $B^{-1}$  using the Lifshitz-Kosevich formula in the field range of 1.5 to 14.5 T. The parameters were used for the simulation are frequency  $f_{SDH} \sim 12$  T, effective mass  $m^* \approx 0.01 m_e$ , Dingle temperature  $T_D = 11$  K, and additional phase shift  $\beta \pm \delta = 0.7$ . These parameters have been extracted from the fitting procedure described in the main text.

## CONCLUSIONS

In summary, I have studied the transport phenomenon of topological semimetals using electrical and thermoelectric transport measurements. Specifically, I explored quantum oscillations in TaAs<sub>2</sub>, anomalous Hall and Nernst effects in CeAlSi and the chiral anomaly in  $\alpha$ -Sn. My studies concerned anomalous thermoelectrical transport phenomena in these semimetals, with objective to discover fundamental aspects of their electronic structures. The reported results, however, can also contribute to the search for new materials, which can be used in advanced technologies.

For TaAs<sub>2</sub>, we investigated the Nernst and Shubnikov - de Hass oscillations in a magnetic field applied along the [-201] direction. At low temperatures, we detected in the Nernst signal two fundamental frequencies  $f_{\nu\alpha} \sim 105$  T and  $f_{\nu\beta} \sim 221$  T and the second harmonic of  $\beta$  frequency i.e.  $2f_{\nu\beta} \sim 442$  T. The temperature dependences of their amplitudes was found to be unusual. We revealed that around  $T \approx 25$  K, the fundamental  $\beta$  oscillation is suppressed, while its second harmonic  $2\beta$  reaches its peak amplitude. We recognized this behavior as the temperature driven spin-zero effect. The temperature dependent g-factor can be an origin of this phenomenon and we noticed that our estimated Landé g-factor at  $T = 25$  K is considerably different from the value found at  $T = 5.4$  K. This may be associated with the non-parabolic band energy dispersion or temperature evolution of the spin-orbit coupling. It is worth noting that the possibility of changes in spin-orbit coupling is particularly intriguing in the case of TaAs<sub>2</sub>, where it may affect the topological attributes of the material. This appears to be an interesting topic for future research.

## Chapter 4: Conclusions

---

For CeAlSi, we performed the measurements of the anomalous Hall effect for two orientation of magnetic field, namely  $B \parallel c$  (hard axis) and  $B \parallel a$  (easy axis), where  $a$  and  $c$  represent crystallographic axes. We have also measured the complementary Nernst effect for  $B \parallel c$  axis and all results indicated the anomalous transport properties of this recently proposed ferromagnetic Weyl semimetal. Below Curie temperature ( $T < T_C$ ), the anomalous Hall conductivity signal showed a positive sign ( $\sigma_{xy}^A > 0$ ) for  $B \parallel c$  axis and a negative sign ( $\sigma_{yz}^A < 0$ ) for  $B \parallel a$  axis. The sign change of AHC in the ferromagnetic regime agrees well with the theoretical DFT results and has been ascribed to the reconstruction of nontrivial electronic structure of CeAlSi induced by the spins reorientation. In this temperature range, we also detected a sizeable anomalous Nernst conductivity when magnetic field was applied  $B \parallel c$  axis. Noticeably, the anomalous contributions are also evident in the paramagnetic phase, where  $\sigma_{xy}^A$  initially increases and peaks at  $T \approx 170$  K and then decreases, whereas  $\sigma_{yz}^A$  successively decreases with increasing temperature. Additionally, the anomalous Nernst conductivity  $\alpha_{xy}^A/T$  also significantly decreases above  $T_C$ . The temperature evolution of  $\sigma_{xy}^A$  and  $\alpha_{xy}^A/T$  are well described by a single band toy model, in which we assume a finite Berry curvature at the Fermi level with Weyl nodes 20 meV apart. We indicated that the topology of Weyl fermionic excitations near the Fermi level plays a key role to determining the anomalous Hall and anomalous Nernst effect in CeAlSi.

Very recently, we have also studied a strained thin film of topological Dirac semimetal  $\alpha$ -Sn, in which we performed the electrical resistivity and thermopower measurements. The results were shown to strongly depend on the directional configuration of magnetic field with respect to the electric field or thermal gradient. For the parallel orientations, we observed negative magnetoresistance and negative slope of the thermopower which can be related to the presence of an anomalous chiral current. The experimental observations are consistent with the theoretical predictions provided by DFT calculations. The observed negative

## Chapter 4: Conclusions

---

magnetoresistance and negative slope of the thermopower exhibit quadratic field dependences indicating a chiral charge pumping that disappears at high temperatures. The detection of chiral current was further confirmed by angle dependent measurements of resistivity and thermopower. Namely, we observed that the negative magnetoresistance and the negative slope of the thermopower disappeared when the magnetic field was tilted away from the direction of the electric current or the thermal gradient, suggesting the restoration of unbalanced chiral neutrality. The calculated ratio of the inter-Weyl node scattering time to Drude scattering time was shown to be, as expected, greater than one at low temperatures.

## BIBLIOGRAPHY

- [1] L. D. Landau, *On the Theory of Phase Transitions Part I*, Zh. Eksp. Teor. Fiz. 11:19 (1937).
- [2] L. D. Landau, *On the Theory of Phase Transitions Part II*, Eksp. Teor. Fiz. 11:627 (1937).
- [3] M. K. D. J. Thouless and M. den N. M. P. Nightingale, *Quantized Hall Conductance in a Two Dimensional Periodic Potential*, Phys. Rev. Lett. **49**, 405 (1982).
- [4] X. G. Wen, *Topological Orders and Edge Excitations in Fractional Quantum Hall States*, Adv. Phys. **44**, 405 (1995).
- [5] M. V. Berry, *Quantal Phase Factors Accompanying Adiabatic Changes*, Proc. R. Soc. Lond. A **392**, 45 (1984).
- [6] C. L. Kane and E. J. Mele, *Quantum Spin Hall Effect in Graphene*, Phys. Rev. Lett. **95**, 226801 (2005).
- [7] D. Hsieh, D. Qian, L. Wray, Y. Xia, Y. S. Hor, R. J. Cava, and M. Z. Hasan, *A Topological Dirac Insulator in a Quantum Spin Hall Phase*, Nature **452**, 970 (2008).
- [8] J. E. Moore, *The Birth of Topological Insulators*, Nature **464**, 194 (2010).
- [9] S. Y. Xu, C. Liu, N. Alidoust, M. Neupane, D. Qian, I. Belopolski, J. D. Denlinger, Y. J. Wang, H. Lin, L. A. Wray, G. Landolt, B. Slomski, J. H. Dil, A. Marcinkova, E. Morosan, Q. Gibson, R. Sankar, F. C. Chou, R. J. Cava, A. Bansil, and M. Z. Hasan, *Observation of a Topological Crystalline Insulator Phase and Topological Phase Transition in  $Pb_{1-x}Sn_xTe$* , Nat. Commun. **3**, 1192 (2012).
- [10] X. Wan, A. M. Turner, A. Vishwanath, and S. Y. Savrasov, *Topological Semimetal and Fermi-Arc Surface States in the Electronic Structure of Pyrochlore Iridates*, Phys. Rev. B **83**, 205101 (2011).
- [11] A. Burkov, *Topological Semimetals*, Nat. Mater. **15**, 1145 (2016).
- [12] N. P. Armitage, E. J. Mele, and A. Vishwanath, *Weyl and Dirac Semimetals in Three-Dimensional Solids*, Rev. Mod. Phys. **90**, 015001 (2018).
- [13] C. K. Chiu, J. C. Y. Teo, A. P. Schnyder, and S. Ryu, *Classification of Topological Quantum Matter with Symmetries*, Rev. Mod. Phys. **88**, 035005 (2016).
- [14] G. E. VOLOVIK, *The Universe in a Helium Droplet Oxford: Clarendon Press* (2003).
- [15] Z. Wang, Y. Sun, X. Q. Chen, C. Franchini, G. Xu, H. Weng, X. Dai, and Z. Fang, *Dirac Semimetal and Topological Phase Transitions in  $A_3Bi$  ( $A=Na, K, Rb$ )*, Phys. Rev. B **85**, 195320 (2012).
- [16] F. D. M. Haldane, *Berry Curvature on the Fermi Surface: Anomalous Hall Effect as a Topological Fermi-Liquid Property*, Phys. Rev. Lett. **93**, 206602 (2004).
- [17] H. Liu, J. Liang, T. Sun, and L. Wang, *Recent Progress in Topological Semimetal and Its Realization in Heusler Compounds*, Mater. Today Phys. **41**, 101343 (2024).

- [18] Q. F. Liang, J. Zhou, R. Yu, Z. Wang, and H. Weng, *Node-Surface and Node-Line Fermions from Nonsymmorphic Lattice Symmetries*, Phys. Rev. B **93**, 085427 (2016).
- [19] C. Herring, *Accidental Degeneracy in the Energy Bands of Crystals*, Phys. Rev. **52**, 365 (1937).
- [20] S. Y. Xu, Y. Xia, L. A. Wray, S. Jia, F. Meier, J. H. Dil, J. Osterwalder, B. Slomski, A. Bansil, H. Lin, R. J. Cava, and M. Z. Hasan, *Topological Phase Transition and Texture Inversion in a Tunable Topological Insulator*, Science. **332**, 560 (2011).
- [21] P. P. Ferreira, A. L. R. Manesco, T. T. Dorini, L. E. Correa, G. Weber, A. J. S. Machado, and L. T. F. Eleno, *Strain Engineering the Topological Type-II Dirac Semimetal NiTe<sub>2</sub>*, Phys. Rev. B **103**, 125134 (2021).
- [22] M. Brahlek, N. Bansal, N. Koirala, S. Y. Xu, M. Neupane, C. Liu, M. Z. Hasan, and S. Oh, *Topological-Metal to Band-Insulator Transition in (Bi<sub>1-x</sub>In<sub>x</sub>)<sub>2</sub>Se<sub>3</sub> Thin Films*, Phys. Rev. Lett. **109**, 186403 (2012).
- [23] Q. Li, D. E. Kharzeev, C. Zhang, Y. Huang, I. Pletikosić, A. V. Fedorov, R. D. Zhong, J. A. Schneeloch, G. D. Gu, and T. Valla, *Chiral Magnetic Effect in ZrTe<sub>5</sub>*, Nat. Phys. **12**, 550 (2016).
- [24] S. M. Young, S. Zaheer, J. C. Y. Teo, C. L. Kane, E. J. Mele, and A. M. Rappe, *Dirac Semimetal in Three Dimensions*, Phys. Rev. Lett. **108**, 140405 (2012).
- [25] J. A. Steinberg, S. M. Young, S. Zaheer, C. L. Kane, E. J. Mele, and A. M. Rappe, *Bulk Dirac Points in Distorted Spinels*, Phys. Rev. Lett. **112**, 036403 (2014).
- [26] M. Neupane, S. Y. Xu, R. Sankar, N. Alidoust, G. Bian, C. Liu, I. Belopolski, T. R. Chang, H. T. Jeng, H. Lin, A. Bansil, F. Chou, and M. Z. Hasan, *Observation of a Three-Dimensional Topological Dirac Semimetal Phase in High-Mobility Cd<sub>3</sub>As<sub>2</sub>*, Nat. Commun. **5**, 3786 (2014).
- [27] Z. K. Liu, B. Zhou, Y. Zhang, Z. J. Wang, H. M. Weng, D. Prabhakaran, S. Mo, Z. X. Shen, Z. Fang, X. Dai, Z. Hussain, and Y. L. Chen, *Topological Dirac Semimetal, Na<sub>3</sub>Bi*, Science. **343**, 864 (2014).
- [28] C. Z. Xu, Y. H. Chan, Y. Chen, P. Chen, X. Wang, C. Dejoie, M. H. Wong, J. A. Hlevyack, H. Ryu, H. Y. Kee, N. Tamura, M. Y. Chou, Z. Hussain, S. K. Mo, and T. C. Chiang, *Elemental Topological Dirac Semimetal:  $\alpha$ -Sn on InSb(111)*, Phys. Rev. Lett. **118**, 146402 (2017).
- [29] M. S. Alam, A. Kazakov, M. Ahmad, R. Islam, F. Xue, and M. Matusiak, *Quantum Transport Properties of the Topological Dirac Semimetal  $\alpha$ -Sn*, ArXiv:2403.00083 (2024).
- [30] A. A. Burkov, *Weyl Metals*, Annu. Rev. Condens. Matter Phys. **9**, 359 (2018).
- [31] H. Weyl, *Elektron Und Gravitation. I*, Zeitschrift Für Phys. **56**, 330 (1929).
- [32] B. Yan and C. Felser, *Topological Materials: Weyl Semimetals*, Annu. Rev. Condens. Matter Phys. **8**, 337 (2017).
- [33] A. A. Burkov and L. Balents, *Weyl Semimetal in a Topological Insulator Multilayer*, Phys. Rev. Lett. **107**, 127205 (2011).
- [34] T. Guan, C. Lin, C. Yang, Y. Shi, C. Ren, Y. Li, H. Weng, X. Dai, Z. Fang, S. Yan,

- and P. Xiong, *Evidence for Half-Metallicity in n-Type HgCr<sub>2</sub>Se<sub>4</sub>*, Phys. Rev. Lett. **115**, 087002 (2015).
- [35] Q. Xu, E. Liu, W. Shi, L. Muechler, J. Gayles, C. Felser, and Y. Sun, *Topological Surface Fermi Arcs in the Magnetic Weyl Semimetal Co<sub>3</sub>Sn<sub>2</sub>S<sub>2</sub>*, Phys. Rev. B **97**, 235416 (2018).
- [36] K. Manna, Y. Sun, L. Muechler, J. Kübler, and C. Felser, *Heusler, Weyl and Berry*, Nat. Rev. Mater. **3**, 244 (2018).
- [37] M. Ikhlas, T. Tomita, T. Koretsune, M. T. Suzuki, D. Nishio-Hamane, R. Arita, Y. Otani, and S. Nakatsuji, *Large Anomalous Nernst Effect at Room Temperature in a Chiral Antiferromagnet*, Nat. Phys. **13**, 1085 (2017).
- [38] C. Z. Li, L. X. Wang, H. Liu, J. Wang, Z. M. Liao, and D. P. Yu, *Giant Negative Magnetoresistance Induced by the Chiral Anomaly in Individual Cd<sub>3</sub>As<sub>2</sub> Nanowires*, Nat. Commun. **6**, 10137 (2015).
- [39] J. Xiong, S. K. Kushwaha, T. Liang, J. W. Krizan, M. Hirschberger, W. Wang, R. J. Cava, and N. P. Ong, *Evidence for the Chiral Anomaly in the Dirac Semimetal Na<sub>3</sub>Bi*, Science. **350**, 413 (2015).
- [40] B. Singh, A. Sharma, H. Lin, M. Z. Hasan, R. Prasad, and A. Bansil, *Topological Electronic Structure and Weyl Semimetal in the TlBiSe<sub>2</sub> Class of Semiconductors*, Phys. Rev. B **86**, 115208 (2012).
- [41] J. Liu and D. Vanderbilt, *Weyl Semimetals from Noncentrosymmetric Topological Insulators*, Phys. Rev. B **90**, 155316 (2014).
- [42] S. Y. Xu, I. Belopolski, N. Alidoust, M. Neupane, G. Bian, C. Zhang, R. Sankar, G. Chang, Z. Yuan, C. C. Lee, S. M. Huang, H. Zheng, J. Ma, D. S. Sanchez, B. K. Wang, A. Bansil, F. Chou, P. P. Shibayev, H. Lin, S. Jia, and M. Z. Hasan, *Discovery of a Weyl Fermion Semimetal and Topological Fermi Arcs*, Science. **349**, 613 (2015).
- [43] S. Souma, Z. Wang, H. Kotaka, T. Sato, K. Nakayama, Y. Tanaka, H. Kimizuka, T. Takahashi, K. Yamauchi, T. Oguchi, K. Segawa, and Y. Ando, *Direct Observation of Nonequivalent Fermi-Arc States of Opposite Surfaces in the Noncentrosymmetric Weyl Semimetal NbP*, Phys. Rev. B **93**, 161112(R) (2016).
- [44] S. Y. Xu, N. Alidoust, I. Belopolski, Z. Yuan, G. Bian, T. R. Chang, H. Zheng, V. N. Strocov, D. S. Sanchez, G. Chang, C. Zhang, D. Mou, Y. Wu, L. Huang, C. C. Lee, S. M. Huang, B. Wang, A. Bansil, H. T. Jeng, T. Neupert, A. Kaminski, H. Lin, S. Jia, and M. Z. Hasan, *Discovery of a Weyl Fermion State with Fermi Arcs in Niobium Arsenide*, Nat. Phys. **11**, 748 (2015).
- [45] S. Y. Xu, I. Belopolski, D. S. Sanchez, C. Zhang, G. Chang, C. Guo, G. Bian, Z. Yuan, H. Lu, T. R. Chang, P. P. Shibayev, M. L. Prokopovych, N. Alidoust, H. Zheng, C. C. Lee, S. M. Huang, R. Sankar, F. Chou, C. H. Hsu, H. T. Jeng, A. Bansil, T. Neupert, V. N. Strocov, H. Lin, S. Jia, and M. Zahid Hasan, *Experimental Discovery of a Topological Weyl Semimetal State in TaP*, Sci. Adv. **1**, e1501092 (2015).
- [46] J. Gaudet, H. Y. Yang, S. Baidya, B. Lu, G. Xu, Y. Zhao, J. A. Rodriguez-Rivera, C. M. Hoffmann, D. E. Graf, D. H. Torchinsky, P. Nikolić, D. Vanderbilt, F. Tafti, and C. L. Broholm, *Weyl-Mediated Helical Magnetism in NdAlSi*, Nat. Mater. **20**, 1650 (2021).

- [47] B. Skinner and L. Fu, *Large, Nonsaturating Thermopower in a Quantizing Magnetic Field*, *Sci. Adv.* **4**, eaat2621 (2018).
- [48] Y. He, J. Gayles, M. Yao, T. Helm, T. Reimann, V. N. Strocov, W. Schnelle, M. Nicklas, Y. Sun, G. H. Fecher, and C. Felser, *Large Linear Non-Saturating Magnetoresistance and High Mobility in Ferromagnetic MnBi*, *Nat. Commun.* **12**, 4576 (2021).
- [49] D. Shoenberg, *Magnetic Oscillations in Metals*, Cambridge Univ. Press (1984).
- [50] G. P. Mikitik and Y. V. Sharlai, *Manifestation of Berry's Phase in Metal Physics*, *Phys. Rev. Lett.* **82**, 2147 (1999).
- [51] N. Nagaosa, J. Sinova, S. Onoda, A. H. MacDonald, and N. P. Ong, *Anomalous Hall Effect*, *Rev. Mod. Phys.* **82**, 1539 (2010).
- [52] Y. Pan, C. Le, B. He, S. J. Watzman, M. Yao, J. Gooth, J. P. Heremans, Y. Sun, and C. Felser, *Giant Anomalous Nernst Signal in the Antiferromagnet YbMnBi<sub>2</sub>*, *Nat. Mater.* **21**, 203 (2022).
- [53] N. P. Ong and S. Liang, *Experimental Signatures of the Chiral Anomaly in Dirac–Weyl Semimetals*, *Nat. Rev. Phys.* **3**, 394 (2021).
- [54] J. Hu, S. Y. Xu, N. Ni, and Z. Mao, *Transport of Topological Semimetals*, *Annu. Rev. Mater. Res.* **49**, 207 (2019).
- [55] A. Narayanan, M. D. Watson, S. F. Blake, N. Bruyant, L. Drigo, Y. L. Chen, D. Prabhakaran, B. Yan, C. Felser, T. Kong, P. C. Canfield, and A. I. Coldea, *Linear Magnetoresistance Caused by Mobility Fluctuations in *n*-Doped Cd<sub>3</sub>As<sub>2</sub>*, *Phys. Rev. Lett.* **114**, 117201 (2015).
- [56] J. Hu, Z. Tang, J. Liu, Y. Zhu, J. Wei, and Z. Mao, *Nearly Massless Dirac Fermions and Strong Zeeman Splitting in the Nodal-Line Semimetal ZrSiS Probed by de Haas-van Alphen Quantum Oscillations*, *Phys. Rev. B* **96**, 045127 (2017).
- [57] M. S. Alam, P. K. Tanwar, K. Dybko, A. S. Wadge, P. Iwanowski, A. Wiśniewski, and M. Matusiak, *Temperature-Driven Spin-Zero Effect in TaAs<sub>2</sub>*, *J. Phys. Chem. Solids* **170**, 110939 (2022).
- [58] W. Zhao and X. Wang, *Berry Phase in Quantum Oscillations of Topological Materials*, *Adv. Phys. X* **7**, 2064230 (2022).
- [59] E. H. Hall, *On a New Action of the magnet on Electric current*, *Am. J. Math.* **2**, 287 (1879).
- [60] E. H. Hall, *XVIII. On the "Rotational Coefficient" in Nickel and Cobalt*, London, Edinburgh, Dublin Philos. Mag. J. Sci. **12**, 157 (1881).
- [61] A. Sakai, S. Minami, T. Koretsune, T. Chen, T. Higo, Y. Wang, T. Nomoto, M. Hirayama, S. Miwa, D. Nishio-Hamane, F. Ishii, R. Arita, and S. Nakatsuji, *Iron-Based Binary Ferromagnets for Transverse Thermoelectric Conversion*, *Nature* **581**, 53 (2020).
- [62] A. A. Burkov, *Anomalous Hall Effect in Weyl Metals*, *Phys. Rev. Lett.* **113**, 187202 (2014).
- [63] S. N. Guin, K. Manna, J. Noky, S. J. Watzman, C. Fu, N. Kumar, W. Schnelle, C.

- Shekhar, Y. Sun, J. Gooth, and C. Felser, *Anomalous Nernst Effect beyond the Magnetization Scaling Relation in the Ferromagnetic Heusler Compound  $\text{Co}_2\text{MnGa}$* , NPG Asia Mater. **11**, 16 (2019).
- [64] S. K. Bac, K. Koller, F. Lux, J. Wang, L. Riney, K. Borisiak, W. Powers, M. Zhukovskiy, T. Orlova, M. Dobrowolska, J. K. Furdyna, N. R. Dilley, L. P. Rokhinson, Y. Mokrousov, R. J. McQueeney, O. Heinonen, X. Liu, and B. A. Assaf, *Topological Response of the Anomalous Hall Effect in  $\text{MnBi}_2\text{Te}_4$  Due to Magnetic Canting*, Npj Quantum Mater. **7**, 46 (2022).
- [65] R. Karplus and J. M. Luttinger, *Hall Effect in Ferromagnetics*, Phys. Rev. **95**, 1154 (1954).
- [66] Q. Wang, Y. Xu, R. Lou, Z. Liu, M. Li, Y. Huang, D. Shen, H. Weng, S. Wang, and H. Lei, *Large Intrinsic Anomalous Hall Effect in Half-Metallic Ferromagnet  $\text{Co}_3\text{Sn}_2\text{S}_2$  with Magnetic Weyl Fermions*, Nat. Commun. **9**, 3681 (2018).
- [67] K. Kuroda, T. Tomita, M. T. Suzuki, C. Bareille, A. A. Nugroho, P. Goswami, M. Ochi, M. Ikhlas, M. Nakayama, S. Akebi, R. Noguchi, R. Ishii, N. Inami, K. Ono, H. Kumigashira, A. Varykhalov, T. Muro, T. Koretsune, R. Arita, S. Shin, T. Kondo, and S. Nakatsuji, *Evidence for Magnetic Weyl Fermions in a Correlated Metal*, Nat. Mater. **16**, 1090 (2017).
- [68] H. Yang, Y. Sun, Y. Zhang, W. J. Shi, S. S. P. Parkin, and B. Yan, *Topological Weyl Semimetals in the Chiral Antiferromagnetic Materials  $\text{Mn}_3\text{Ge}$  and  $\text{Mn}_3\text{Sn}$* , New J. Phys. **19**, 015008 (2017).
- [69] J. Barth, G. H. Fecher, B. Balke, T. Graf, A. Shkabko, A. Weidenkaff, P. Klaer, M. Kallmayer, H. J. Elmers, H. Yoshikawa, S. Ueda, K. Kobayashi, and C. Felser, *Anomalous Transport Properties of the Half-Metallic Ferromagnets  $\text{Co}_2\text{TiSi}$ ,  $\text{Co}_2\text{TiGe}$  and  $\text{Co}_2\text{TiSn}$* , Philos. Trans. R. Soc. A **369**, 3588 (2011).
- [70] M. S. Alam, A. Fakhredine, M. Ahmad, P. K. Tanwar, H. Y. Yang, F. Tafti, G. Cuono, R. Islam, B. Singh, A. Lynnyk, C. Autieri, and M. Matusiak, *Sign Change of Anomalous Hall Effect and Anomalous Nernst Effect in the Weyl Semimetal  $\text{CeAlSi}$* , Phys. Rev. B **107**, 85102 (2023).
- [71] J. Smit, *The Spontaneous Hall Effect in Ferromagnetics I*, Physica **21**, 877 (1955).
- [72] L. Berger, *Influence of Spin-Orbit Interaction on the Transport Processes in Ferromagnetic Nickel Alloys, in the Presence of a Degeneracy of the 3d Band*, Physica **30**, 1141 (1964).
- [73] R. A. Bertlmann, *Anomalies in Quantum Field Theory: Dispersion Relations and Differential Geometry*, Nucl. Phys. B (Proc. Suppl.) **39**, 482 (1995).
- [74] S. L. Adler, *Axial-Vector Vertex in Spinor Electrodynamics*, Phys. Rev. **177**, 2426 (1969).
- [75] H. B. Nielsen and M. Ninomiya, *The Adler-Bell-Jackiw Anomaly and Weyl Fermions in a Crystal*, Phys. Lett. B **130**, 389 (1983).
- [76] D. T. Son and B. Z. Spivak, *Chiral Anomaly and Classical Negative Magnetoresistance of Weyl Metals*, Phys. Rev. B **88**, 104412 (2013).
- [77] K. Yoshida, *A Geometrical Transport Model for Inhomogeneous Current Distribution*

- in Semimetals under High Magnetic Fields*, J. Phys. Soc. Jpn **40**, 1027 (1976).
- [78] M. C. Chang and M. F. Yang, *Chiral Magnetic Effect in the Absence of Weyl Node*, Phys. Rev. B **92**, 205201 (2015).
- [79] C. Felser and J. Gooth, *Topology and Chirality*, ArXiv:2205.05809 (2023).
- [80] T. J. Seebeck, “*Magnetische Polarisation Der Metalle Und Erze Durch Temperatur-Differenz*” (*Magnetic Polarization of Metals and Minerals by Temperature Differences*), *Abhandlungen Der Königlichten Akademie Der Wissenschaften Zu Berlin*, Treatises R. Acad. Sci. Berlin pp. 265 (2003).
- [81] H. B. Callen, *The Application of Onsager’s Reciprocal Relations to Thermoelectric, Thermomagnetic, and Galvanomagnetic Effects*, Phys. Rev. **73**, 1349 (1948).
- [82] Kamran. Behnia, *Fundamentals of Thermoelectricity*, Oxford University Press, Oxford, UK (2015).
- [83] T. Liang, Q. Gibson, J. Xiong, M. Hirschberger, S. P. Koduvayur, R. J. Cava, and N. P. Ong, *Evidence for Massive Bulk Dirac Fermions in  $Pb_{1-x}Sn_xSe$  from Nernst and Thermopower Experiments*, Nat. Commun. **4**, 2696 (2013).
- [84] K. Behnia and H. Aubin, *Nernst Effect in Metals and Superconductors: A Review of Concepts and Experiments*, Reports Prog. Phys. **79**, 046502 (2016).
- [85] E. H. Sondheimer, *The Theory of the Galvanomagnetic and Thermomagnetic Effects in Metals*, Proc. R. Soc. London. Ser. A. Math. Phys. Sci. **193**, 484 (1948).
- [86] N. F. Mott and H. Jones, *The Theory of the Properties of Metals and Alloys*, Oxford University Press, Oxford (1936).
- [87] N. W. Ashcroft and N. D. Mermin, *Solid State Physics*, Holt, Rinehart and Winston (1976).
- [88] C. L. F. and D. G. Frank J. Blatt, Peter A. Schroeder, *THERMOELECTRIC POWER OF METALS*, Plenum Press, New York (1976).
- [89] V. Kozii, B. Skinner, and L. Fu, *Thermoelectric Hall Conductivity and Figure of Merit in Dirac/Weyl Materials*, Phys. Rev. B **99**, 155123 (2019).
- [90] X. Xu, Y. Liu, G. Seyfarth, A. Pourret, W. Ma, H. Zhou, G. Wang, Z. Qu, and S. Jia, *Thermoelectric Transport and Phonon Drag in Weyl Semimetal Monochalcogenides*, Phys. Rev. B **104**, 115164 (2021).
- [91] M. Matusiak, J. R. Cooper, and D. Kaczorowski, *Thermoelectric Quantum Oscillations in  $ZrSiS$* , Nat. Commun. **8**, 15219 (2017).
- [92] Z. Jia, C. Li, X. Li, J. Shi, Z. Liao, D. Yu, and X. Wu, *Thermoelectric Signature of the Chiral Anomaly in  $Cd_3As_2$* , Nat. Commun. **7**, 13013 (2016).
- [93] J. Noky, J. Gooth, C. Felser, and Y. Sun, *Characterization of Topological Band Structures Away from the Fermi Level by the Anomalous Nernst Effect*, Phys. Rev. B **98**, 241106(R) (2018).
- [94] D. Gresch, Q. Wu, G. W. Winkler, and A. A. Soluyanov, *Hidden Weyl Points in Centrosymmetric Paramagnetic Metals*, New J. Phys. **19**, 035001 (2017).
- [95] S. Sun, Z. Song, H. Weng, and X. Dai, *Topological Metals Induced by the Zeeman*

- Effect*, Phys. Rev. B **101**, 125118 (2020).
- [96] H. Y. Yang, B. Singh, J. Gaudet, B. Lu, C. Y. Huang, W. C. Chiu, S. M. Huang, B. Wang, F. Bahrami, B. Xu, J. Franklin, I. Sochnikov, D. E. Graf, G. Xu, Y. Zhao, C. M. Hoffman, H. Lin, D. H. Torchinsky, C. L. Broholm, A. Bansil, and F. Tafti, *Noncollinear Ferromagnetic Weyl Semimetal with Anisotropic Anomalous Hall Effect*, Phys. Rev. B **103**, 115143 (2021).
- [97] J. Polaczyński, G. Krizman, A. Kazakov, B. Turowski, J. B. Ortiz, R. Rudniewski, T. Wojciechowski, P. Dłużewski, M. Aleszkiewicz, W. Zaleszczyk, B. Kurowska, Z. Muhammad, M. Rosmus, N. Olszowska, L.-A. De Vaultier, Y. Guldner, T. Wojtowicz, and V. V. Volobuev, *3D Topological Semimetal Phases of Strained  $\alpha$ -Sn on Insulating Substrate*, ArXiv:2309.03951 (2023).
- [98] M. S. and P. S. Michael Binnewies, Robert Glaum, *Chemical Vapor Transport Reactions*, De G., Berlin, Boston, (2012).
- [99] A. W. Ashutosh S Wadge, Grzegorz Grabecki, Carmine Autieri, Bogdan J Kowalski, Przemysław Iwanowski, Giuseppe Cuono, MF Islam, Carlo M Canali, Krzysztof Dybko, Andrzej Hruban, Andrzej Łusakowski, Tomasz Wojciechowski, Ryszard Diduszko, Artem Lynnyk, Natalia Ols, *Electronic Properties of TaAs<sub>2</sub> Topological Semimetal Investigated by Transport and ARPES*, J. Phys. Condens. Matter **34**, 125601 (2022).
- [100] G. Lehmppuhl, A. Ichimiya, and H. Nakahara, *Interpretation of RHEED Oscillations during MBE Growth*, Surf. Sci. Lett. **245**, L159 (1991).
- [101] A. Chambers, *Creating a Vacuum - Pumps*, Chapman & Hall (CRC) (2005).
- [102] S. M. N. and P. S. R. A. Kubiak, *Molecular Beam Epitaxy*, William Andrew Publishing, 1-113 (1995).
- [103] B. Wang, B. Singh, B. Ghosh, W. C. Chiu, M. M. Hosen, Q. Zhang, L. Ying, M. Neupane, A. Agarwal, H. Lin, and A. Bansil, *Topological Crystalline Insulator State with Type-II Dirac Fermions in Transition Metal Dipnictides*, Phys. Rev. B **100**, 205118 (2019).
- [104] Y. Luo, R. D. McDonald, P. F. S. Rosa, B. Scott, N. Wakeham, N. J. Ghimire, E. D. Bauer, J. D. Thompson, and F. Ronning, *Anomalous Electronic Structure and Magnetoresistance in TaAs<sub>2</sub>*, Sci. Rep. **6**, 27294 (2016).
- [105] Y. Y. Wang, Q. H. Yu, P. J. Guo, K. Liu, and T. L. Xia, *Resistivity Plateau and Extremely Large Magnetoresistance in NbAs<sub>2</sub> and TaAs<sub>2</sub>*, Phys. Rev. B **94**, 041103(R) (2016).
- [106] H. Y. Yang, B. Singh, B. Lu, C. Y. Huang, F. Bahrami, W. C. Chiu, D. Graf, S. M. Huang, B. Wang, H. Lin, D. Torchinsky, A. Bansil, and F. Tafti, *Transition from Intrinsic to Extrinsic Anomalous Hall Effect in the Ferromagnetic Weyl Semimetal PrAlGe<sub>1-x</sub>Si<sub>x</sub>*, APL Mater. **8**, 011111 (2020).
- [107] G. Chang, B. Singh, S. Y. Xu, G. Bian, S. M. Huang, C. H. Hsu, I. Belopolski, N. Alidoust, D. S. Sanchez, H. Zheng, H. Lu, X. Zhang, Y. Bian, T. R. Chang, H. T. Jeng, A. Bansil, H. Hsu, S. Jia, T. Neupert, H. Lin, and M. Z. Hasan, *Magnetic and Noncentrosymmetric Weyl Fermion Semimetals in the RAlGe Family of Compounds (R= Rare Earth)*, Phys. Rev. B **97**, 041104(R) (2018).

Dostępny do artykułów:

**1.Md Shahin Alam**, P.K. Tanwar, Krzysztof Dybko, Ashutosh S. Wadge, Przemysław Iwanowski, Andrzej Wiśniewski, Marcin Matusiak, *Temperature-Driven Spin-Zero Effect in TaAs<sub>2</sub>*, J. Phys. Chem. Solids **170**, 110939 (2022), <https://doi.org/10.1016/j.jpics.2022.110939>.

**2.Md Shahin Alam**, Amar Fakhredine, Mujeeb Ahmad, P. K. Tanwar, Hung-Yu Yang, Fazel Tafti, Giuseppe Cuono, Rajibul Islam, Bahadur Singh, Artem Lynnyk, Carmine Autieri, and Marcin Matusiak, *Sign change of anomalous Hall effect and anomalous Nernst effect in the Weyl semimetal CeAlSi*, Phys. Rev. B **107**, 85102 (2023), DOI: 10.1103/PhysRevB.107.085102

**3.Md Shahin Alam**, Alexandr Kazakov, Mujeeb Ahmad, Rajibul Islam, Fei Xue, Marcin Matusiak, Quantum transport properties of the topological Dirac semimetal  $\alpha$ -Sn, Phys. Rev. B 109, 245135– Published 26 June, 2024 Published 26 June, 2024, DOI: <https://doi.org/10.1103/PhysRevB.109.245135>